國立臺灣大學工學院土木工程研究所

碩士論文

Department of Civil Engineering

College of Engineering

National Taiwan University

Master Thesis

加勁擋土牆以含細粒料之回填土在降雨作用下之行為及改善方法評估

Evaluation of Improved Methods for Geosynthetic-Reinforced Soil Walls with Marginal Backfills subjected to Rainfall

呂昕臻

Hsin-Chen Lu

指導教授：楊國鑫 博士

Advisor: Kuo-Hsin Yang, Ph.D.

中華民國 108 年 7 月

July, 2019

doi:10.6342/NTU201901530

國立臺灣大學碩士學位論文
口試委員會審定書

Evaluation of Improved Methods for Geosynthetic-Reinforced Soil Walls with Marginal Backfills subjected to Rainfall

本論文係呂昕臻君（R06521108）在國立臺灣大學土木工程學系完成之碩士學位論文，於民國一〇八年七月四日承下列考試委員審查通過及口試及格，特此證明

口試委員

	楊　國　鑫 （指導教授）	楊國鑫 （簽　名）
	方　永　壽	方永壽
	洪　勇　善	洪勇善
	黃　景　川	黃景川
系 主 任	謝　尚　賢	謝尚賢

doi:10.6342/NTU201901530

doi:10.6342/NTU201901530

Acknowledgement

首先，向恩師楊國鑫教授致上最高的謝意與敬意，碩士生涯中不斷地引領我們思考、學習。除了學術方面，老師也以身作則，培養我們做學問及面對問題該有的嚴謹態度。此外，也謝謝口試委員黃景川教授、洪勇善教授、及方永壽教授於百忙之中撥冗審閱並提供建議，使本論文更臻完善。

在研究所期間，也很感謝兆偉、名琁、奕新、蔣榮、昕明、Son 等學長姊的悉心帶領及教導我們各種試驗流程及儀器使用。對研究室的好夥伴建澄、健鈞、Mark 以及最貼心的學妹們婷苓、昱葵、于萱亦是感激不盡。謝謝你們不惜犧牲自己念書做研究的時間來幫我一起做實驗，尤其是婷苓，幾乎每一次的實驗都有你的參與。至於我的實驗夥伴 Mark，非常榮幸能和你一起合作，這兩年來我們從未知慢慢摸索、解決問題，也精進了自己團隊合作及溝通的能力。除了很高興能夠在日常生活中有練習英語口說的機會之外，實驗中的重物也很感謝你幫忙搬。

最後，將最深的感謝獻給我最愛的家人。感謝你們在求學過程中全力的支持關愛，提供衣食無缺的生活，使我能無後顧之憂的專心在研究所課業及實驗。你們無疑是此論文最大的功臣之一，能夠生在這樣的家庭是如此的幸運。願自己能在不久的將來對你們獻上最大的回饋。

謹以此論文獻給我最親愛的家人及朋友，並勉勵自己保持積極嚴謹的態度，朝向未來前進。

呂昕臻　謹誌于

國立台灣大學　土木工程學系　大地組　2018.07

doi:10.6342/NTU201901530

摘要

加勁擋土牆相較於傳統重力式擋土牆為柔性的擋土結構物，因此被視為邊坡穩定中最好的方法之一。然而為因應台灣地方法規，富含細粒料的現地土壤常被利用為背填土。當降雨入滲時，背填土基質吸力的喪失以及土壤剪力強度的弱化都是導致以含細粒料的現地土背填的加勁擋土牆破壞之主因。因此本研究致力於了解以富含細粒料的土壤為背填土的加勁擋土牆在降雨情況下的行為以及破壞模式。

本研究進行了一系列以富含細粒料的土壤為背填土的加勁擋土牆之縮尺試驗，除了了解其在降雨情況下的行為之外，也提出改善的方法供實際應用並探討其改善之效益。改善方法包含了縮小加勁材間距、使用高滲透係數的回填土、以及在加勁材界面鋪設薄砂層。試驗中降雨的延時設定使模型加勁擋土牆達到穩定狀態，或是直到擋土牆完全破壞為止。而在每組試驗中均紀錄了體積含水量、孔隙水壓、及牆變位；發展出的加勁材應變及土壤剪力也利用實驗後的影像處理來分析。

研究結果顯示縮小加勁材間距有助於維持模型加勁擋土牆之穩定，並使牆變位最小化。此外，使用高滲透係數的回填土雖然能有效的避免基質吸力的喪失，但仍會發展出張力裂縫，同時也使破壞機制轉為較於瞬間的表面淺層破壞。至於薄紗層的設計則是對以富含細粒料的土壤為背填土的加勁擋土牆在降雨情況下有相當優良的成效。除了加勁材與背填土之間的摩擦力增加之外，牆體本身受覆土壓力而變形的程度也因為採用了薄紗層而大幅改善。由於變形量為影響加勁擋土牆表現之關鍵因素，因此本研究認為在降雨情況下的設計安全係數須因應最大容許之牆變為來提升。

關鍵字：加勁擋土牆、富含細粒料之背填土、降雨、模型試驗

doi:10.6342/NTU201901530

Abstract

Geosynthetic reinforced soil walls (GRS walls) are considered as one of the best among all slope stabilization methods. However, in-situ soil (marginal backfill) was often adopted to adhere to a local regulation which specifies that the excavated and backfilled soils should be balanced. Loss of matric suction and soil shear strength due to rainfall infiltration is a main cause of the failure of GRS walls with marginal backfill.

A series of reduced scale model tests was performed to investigate the performance of GRS walls with marginal backfill under rainfall conditions and to propose improved methods for practical design. The effects of the three improved methods, namely, reduction of reinforcement spacing, selection of better quality backfill, and adoption of sand cushions, were evaluated. Rainfall duration was set such that the wall model became fully wet or the monitored value reached steady state. The volumetric water content and the pore water pressure were monitored and the wall displacement was recorded throughout the tests. Mobilized reinforcement tensile strain was evaluated and the strain distribution in the wall models was analyzed via post image processing.

The test results indicated that the reduction of reinforcement spacing can effectively improve the stability of the wall; meanwhile, the displacement was diminished. In addition, applying granular backfill can indeed avoid the loss of matric suction; however, tensions cracks or critical failure surface developed suddenly. Finally, the adoption of sand cushions is complementary beneficial to the performance of GRS walls with marginal backfill under rainfall condition. Not only was the interface friction enhanced but the deformation characteristic was improved. The sand cushions also accelerated the dissipation of water.

Keywords: Geosynthetic-reinforced walls; Marginal backfill; Rainfall; Model tests

doi:10.6342/NTU201901530

Table of Contents

doi:10.6342/NTU201901530

doi:10.6342/NTU201901530

List of Figures

Chapter 1

Chapter 2

doi:10.6342/NTU201901530

Chapter 3

Chapter 4

doi:10.6342/NTU201901530

Chapter 5

doi:10.6342/NTU201901530

Chapter 6

doi:10.6342/NTU201901530

doi:10.6342/NTU201901530

List of Tables

Chapter 1

Chapter 2

Chapter 3

Chapter 4

Chapter 5

Chapter 6

doi:10.6342/NTU201901530

Chapter 1 Introduction

1.1 Research Background and Motivation

In recent years, global warming has been considered as one of the greatest threats to earth; it not only causes the rise of sea levels but also changes the pattern of precipitation. From a geotechnical engineering standpoint, the pattern of precipitation, which has a trend of becoming more and more extreme, is of great concern. More specifically, a high-intensity rainfall in a flash or a long-lasting rainfall became frequent occurrence. The above-mentioned situation has caused slope stability issues around the world and has caused catastrophic damage. Figure 1.1 shows some pictures of slope stability problems induced by rainfall.

(a) (b)

Figure 1.1 Rainfall induced slope instability: (a) Kyushu, Japan; (b) Maokong Gondola

Various measures have been taken to stabilize the slopes, as shown in Table 1.1. Factors such as the mode of failure, the feasibility of construction, the effect of stabilizing, and the eco-friendliness should be considered upon designing. Conventional RC structures can be easily controlled to satisfy the requirement of the quality and can perform well on stabilizing the slopes. Nevertheless, RC structures are not only

doi:10.6342/NTU201901530

detrimental to the environment but they also restrain much of the deformation, causing abrupt failure. Contrarily, geosynthetic reinforced soil (GRS) structures can provide significant enhancement on the slope stability; meanwhile, the tolerance of the deformation is dramatically improved due to the flexibility of the GRS structures. Therefore, GRS structures, having the advantages of eco-friendliness, high tolerance of deformation, and eloquent reduction in the risk of sudden collapse, are considered as one of the best measures to stabilize the slopes (Wu and Chou, 2013).

With various advantages, GRS walls are widely used all over the world for slope stabilization. However, the application of GRS structures has certain limitations. The use of good quality backfills with high permeability (i.e., pure sand) is indeed satisfactory. Nevertheless, for the cut down of the cost and the convenience of the construction, in-situ soil is often used as backfills. Additionally, in-situ soil was adopted to adhere to a local regulation which specifies that the excavated and backfilled soils at the construction site should be balanced. In-situ soil, considered as marginal backfill, consists of sand and fines contents. Marginal backfill has little capacity for drainage. Loss of matric suction and soil shear strength due to the infiltration of rainfall has long been one of the main causes of the failure of GRS walls. Figure 1.2 enunciates the mechanism and process of a GRS slope failure triggered by rainfall. Among all types of failures, rainfall holds the largest portion of the causes. Figure 1.3 presents some failure cases of GRS structures caused by rainfall. According to preceding studies, up to 60% of GRS wall failure was caused by water (Koerner and Koerner, 2013). Intense rainfall had then been identified as the most critical natural factor on slope stability (Wu et al., 2013). Hence, investigating the performance of slopes under rainfall condition and stabilizing the slopes is mandatory. This study purports to evaluate the performance of GRS walls with marginal backfills and propose remedial measures by using different backfill or configurations.

Table 1.1 Slope stability measures and application

Construction method	Method illustration	Applications and advantages
GRS structures		Applications: 1. Embankment 2. Repairment measures Advantages: 1. Flexibility 2. Eco-friendly
Ground anchor with RC grid beam		Applications: 1. Gentle slope 2. Dip slope Advantages: 1. Time-saving 2. Vegetation in grid
RC grid beam		Applications: 1. Uneven slope 2. Steep slope Advantages: 1. Slope-adjusted 2. Vegetation in grid
RC retaining wall		Applications: 1. Excavation toe stability 2. Landfill stability Advantages: 1. Durable 2. Concrete can be controlled and meet requirements
Shotcrete		Applications: 1. Steep slope 2. No-vegetation slope Advantages: 1. Fill the discontinuity of slope surface

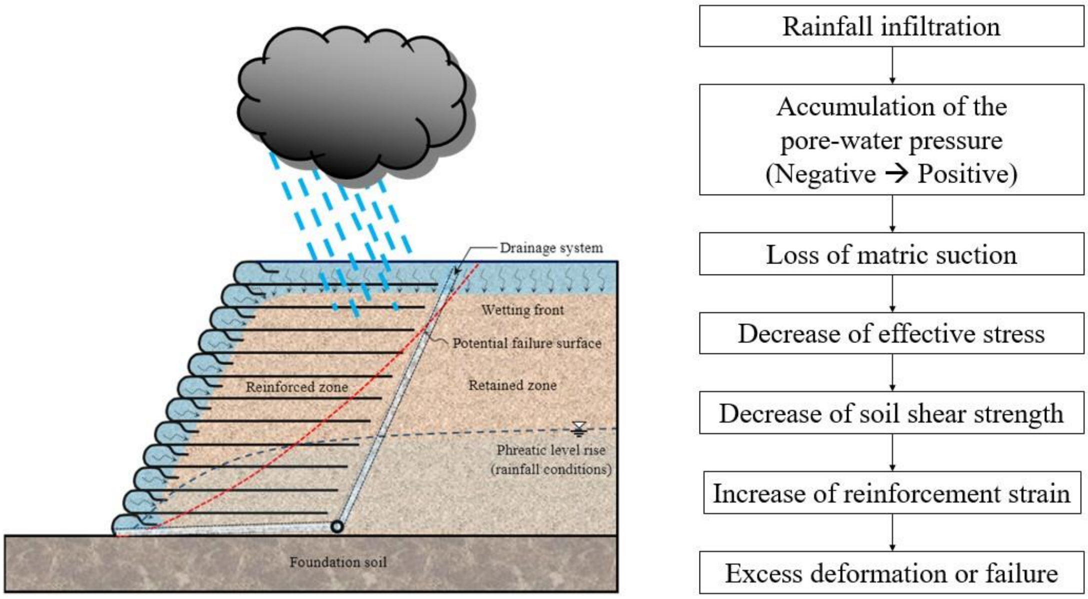

Figure 1.2 Mechanism of rainfall induced GRS structure failure

Figure 1.3 GRS wall failure caused by rainfall (Wu and Chou, 2013)

1.2 Research Objectives

This research carried out a series of reduced scale model tests of GRS walls subjected to rainfall. The performance of GRS walls with marginal backfill was investigated. Various improved methods concerning different backfills and configurations were also evaluated. The target of this research is to pursue the following:

- To investigate the hydraulic performance and failure mechanism of GRS walls subjected to rainfall.
- To evaluate the effects of different backfills and configurations on GRS walls under rainfall condition.
- To propose improved measures for practical design of GRS walls with marginal backfills against rainfall.

1.3 Research Layout

This thesis presents a study on GRS walls with marginal backfills subjected to rainfall and proposed improved measures for practical design. The performance of GRS wall subjected to rainfall is discussed in terms of pore water pressure, volumetric water content, the reinforcement strain, and the wall displacement. Figure 1.4 illustrates the research flow chart of the thesis, including the above introduction. The thesis is organized as follows:

Chapter 1 introduces the background, motivation, and objectives of this research. Additionally, the layout of this research is provided herein.

Chapter 2 presents the literature review including the introduction of geosynthetic reinforced structures, the scaling laws for conducting model tests, and the investigation of the performance of geosynthetic reinforced walls subjected to rainfall.

doi:10.6342/NTU201901530

Chapter 3 elaborates the testing of material properties, which involves the physical and engineering properties of the testing soil, and the material properties of the reinforcement used in this study.

Chapter 4 presents the reduced scale model tests, including the design of the experiments, the apparatus used in this study, and the detailed procedure of the model tests.

Chapter 5 discusses the results in terms of the volumetric water content, wall displacement, and the strain of the reinforcement. Comparison of the performance of GRS walls with marginal backfill under different reinforcement spacing is presented.

Chapter 6 provides the results of the improved design. Evaluation of the influence of different backfill materials and design configurations on the performance of GRS wall was also presented.

Chapter 7 draws to the conclusions of this research and proposes recommendations and suggestions for future study and practical application.

doi:10.6342/NTU201901530

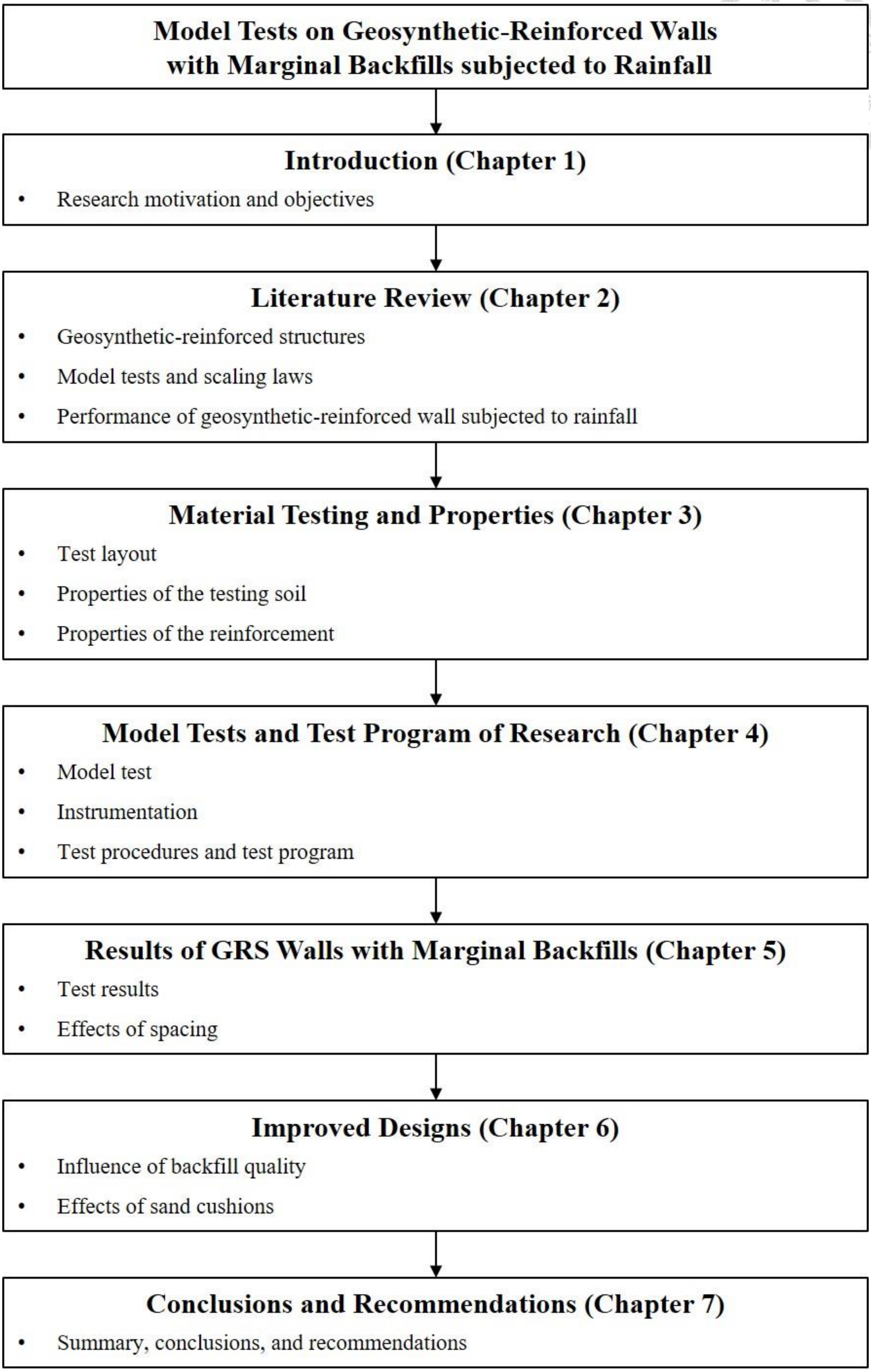

Figure 1.4 Research Flowchart

Chapter 2 Literature Review

2.1 History and Design Methods of GRS Structures

2.1.1 History

The concept of reinforced soil came into existence centuries ago in ancient China and western countries. The Great Wall which was built in 200 B.C. is a well-known example of geosynthetic reinforced structure. The geosynthetics used to build the Great Wall includes willow and reed. The conceptualization of geosynthetic reinforced structures was not discovered until Henry Vidal, an engineer from France, got inspired from observing how a bird builds its nest in the 1960s. He proposed a way of constructing GRS walls by using sandy soil as the backfill, steel sheets as the reinforcement, and concrete plate as the facing. Through unremitting efforts, the GRS wall system has been promoted successfully and has gained recognition among the geotechnical engineering field (Chou et al., 2016).

2.1.2 Basic Principles

Geosynthetic reinforced structures are combinations of soil and geosynthetics which have tensile strength. Because of the overburden pressure and the self-weight of the soil, there exists a frictional force between the soil and the geogrid when there is a relative displacement. The geosynthetic will thus be subjected to a tensile force. Therefore, the overall stability and the shear strength of the reinforced soil increase with the increase of the apparent adhesion and the confining pressure of the reinforced soil, which results from the geosynthetics' resistance to tensile force. Additionally, the interlocking effect between the soil particles and the openings of the geosynthetics mobilizes the resistance force. With the application of geosynthetics, the soil wall is able to resist much more tensile force.

doi:10.6342/NTU201901530

2.1.3 Failure Mode and Design of GRS Structures

The failure mechanisms of the GRS structures, as shown in Figure 2.1, can be classified into two categories, namely, internal and external failure. Internal failure includes breakage, pullout, and connection of the reinforcement while external failure involves failure of sliding, bearing capacity, and overturning. The designing regulations for GRS structures, for example, FHWA, ASSHTO, and NCMA take the failure mechanisms into consideration. Breakage and pullout failure of the reinforcement are enunciated in the following sections. The failure mechanisms of external failure will not be elaborated since they are similar to that of the general retaining walls.

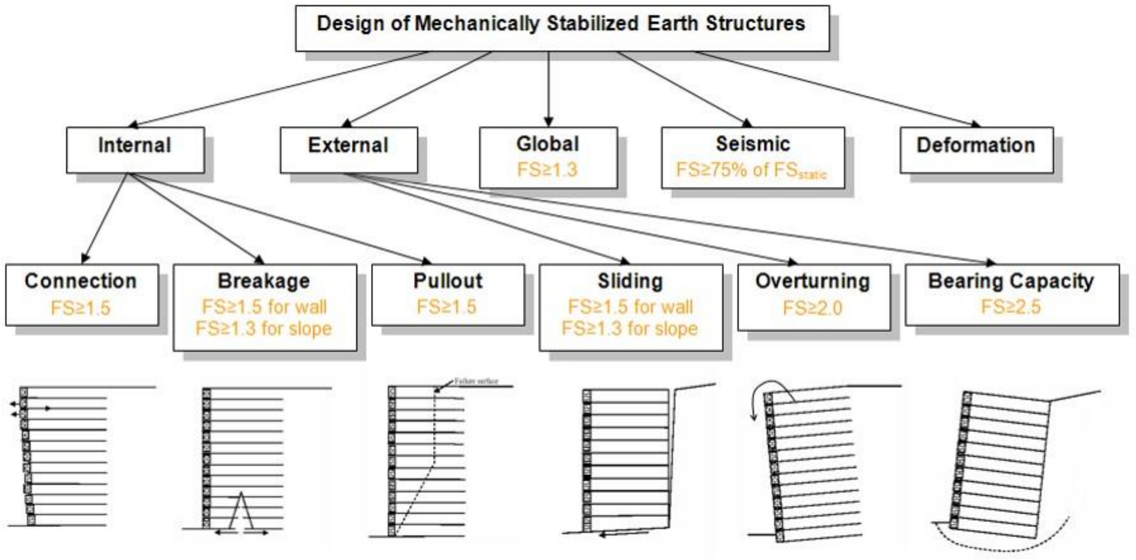

Figure 2.1 Failure mechanisms of GRS structures

A. Reinforcement Breakage Failure

According to the designing regulations of the Federal Highway Administration (FHWA, 2009), the maximum tensile force that could be mobilized in a single layer can be estimated in Equation 2.1:

$$T_{\max} = \left(\frac{K_r}{K_a}\right) k_a S_v (\gamma z + q) \tag{2.1}$$

$$FS = \frac{T_{al}}{T_{\max}} \geq 1.5 \tag{2.2}$$

where $T_{\max}$ = maximum tensile force that could be mobilized, K_r/K_a = normalized coefficient of lateral earth pressure, k_a = coefficient of lateral earth pressure, S_v = spacing of the reinforcement, γ = unit weight of the backfill soil, z = depth from the crest of the wall, and q = surcharge. This equation is based on the assumption that the earth pressure behind the retaining wall and the mobilized maximum tensile force has reached static equilibrium. Moreover, the normalized coefficient of lateral earth pressure K_r/K_a varies with different types of reinforcement and the depth from the crest of the wall, as shown in Figure 2.2. If a reinforcement with high extensibility was used, and the deformation is large enough the cause active failure, K_r/K_a will keep a constant value of 1.0. Therefore, to prevent the geosynthetic from breakage failure, the allowable tensile force, T_{al}, has to be at least 1.5 times larger than the mobilized tensile force, $T_{\max}$, as shown in Equation 2.2:

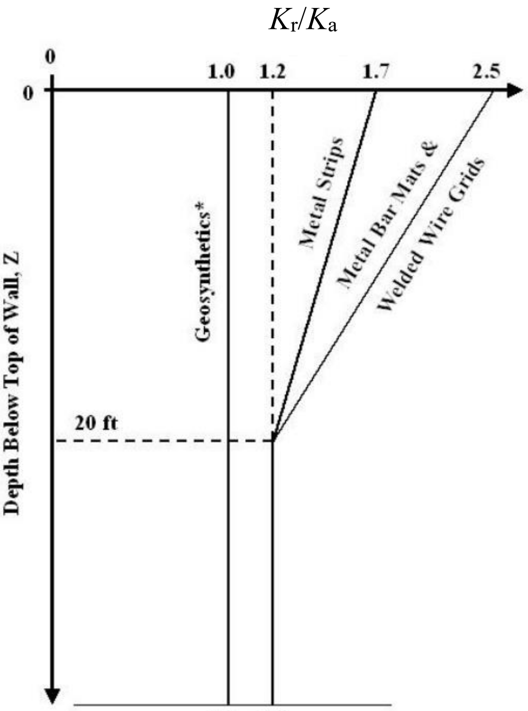

Figure 2.2 Normalized coefficient of lateral earth pressure (FHWA, 2009)

doi:10.6342/NTU201901530

B. Reinforcement Pullout Failure

The pullout resistance of the reinforcement can be estimated using Equation 2.3, Equation 2.4, and Equation 2.5, given by the Federal Highway Administration (FHWA, 2009):

$$P_r = c\, F^* \alpha\, \sigma_{\mathrm{v}}\, L_{\mathrm{e}} \tag{2.3}$$

$$F^* = \frac{2}{3}\tan\phi \tag{2.4}$$

$$FS = \frac{P_r}{T_{\max}} \geq 1.5 \tag{2.5}$$

where P_{r} = pullout resistance force of the reinforcement, c = effective unit perimeter of the reinforcement, F^* = pullout resistance factor of the reinforcement, α = correction factor of the reinforcement extensibility, σ_{v} = vertical overburden pressure above the reinforcement, and L_{e} = embedded length of the reinforcement.

It can be clearly seen from Figure 2.3 that the pullout resistance force of the reinforcement, P_{r}, develops from the frictional force of both two sides ($c = 2$) of the embedded reinforcement L_{e}. Additionally, the correction factor of the reinforcement extensibility α varies with different types of reinforcement and the values are summarized in Table 2.1. Regarding the coefficient of the pullout resistance of the reinforcement F^*, the frictional force between the soil and the reinforcement along with the passive resistance between the soil particles and the reinforcement are what cause so. Figure 2.4 presents the schematic picture of the mechanism of the interlocking effect. The value of F^* can be obtained by conducting wide width tensile strength test or by Equation 2.4, where ϕ is the friction angle of the backfill soil. In order to prevent the reinforcement from pullout failure, the pullout resistance force of the reinforcement, P_{r}, should be larger than 1.5 times of the maximum tensile force that could be mobilized, $T_{\max}$, as shown in Equation 2.5.

doi:10.6342/NTU201901530

Table 2.1 Correction factor of the reinforcement extensibility of different materials (FHWA, 2009)

Reinforcement Type	Correction Factor α
Metallic	1.0
Geogrid	0.8
Geotextile	0.6

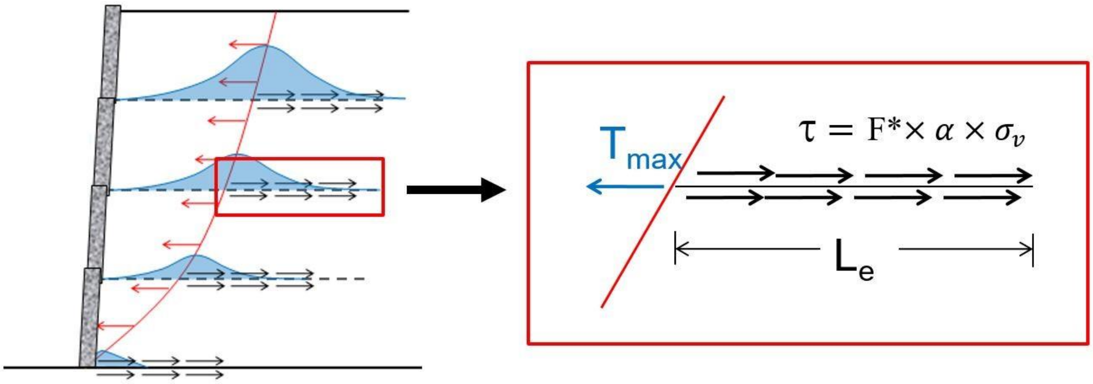

Figure 2.3 Schematic view of the pullout resistance of the reinforcement

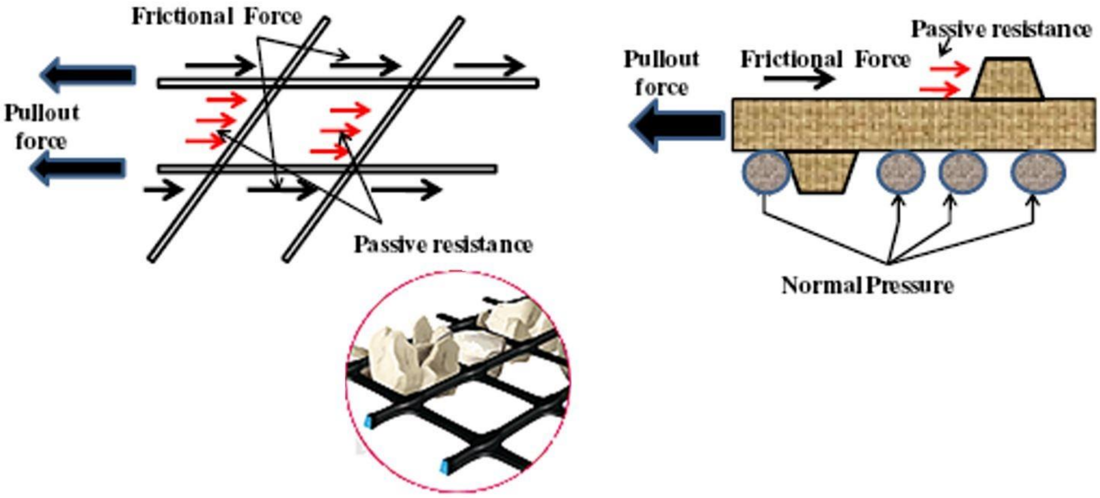

Figure 2.4 Schematic view of the interlocking effect

2.2 Performance of GRS Structures subjected to rainfall or seepage

Past studies indicated that intense rainfall is the primary natural cause for the observed failure cases (Table 2.2). Thus, various studies have been carried out to inspect the performance of geosynthetic reinforced walls subjected to rainfall. Rainfall-induced pore water pressure accumulation and development inside the GRS structures caused excessive deformation, local, or overall failure. Aside from case studies, model tests have been conducted to evaluate the performance of GRS walls subjected to rainfall. Factors such as the rainfall intensity, rainfall duration, the quality of the backfill, and the reinforcement configurations are all critical to the stability of the wall. Details of the case studies and model tests are discussed in subsequent sections.

Table 2.2 Generic causes of mechanically stabilized earth failure (Wu et al., 2013)

Primary causes	Subsets
Natural influences	Intense rainfall
	Strong earthquake
Technical errors	Inadequate project planning and site exploration
	Erroneous analysis and design
	Material deficiencies
	Poor construction quality
	Improper service and maintenance

2.2.1 Case Study

Koerner investigated 171 failed mechanically stabilized earth (MSE) walls with geosynthetic reinforcement (Koerner and Koerner, 2013). It was noted that among all failed cases, 60% were caused by internal or external water. In addition, silt and clay soil types were used as backfill materials in 61% of the failure cases. The reason for the use of fine-grained soils is felt to be their availability at a low cost in comparison to the cost of sands and gravels which usually have to be imported to the site. The concern over and critical issue of using such fine-grained soils is that they have low to extremely low hydraulic conductivity. This can be properly handled by proper design; however, the research stated that water within, behind, or beneath the reinforced zone which can mobilize hydrostatic pressure are rarely accounted for in the design process. Figure 2.5

presents the failure mechanisms induced by internal and external water. More failure cases were investigated and were thoroughly discussed subsequently.

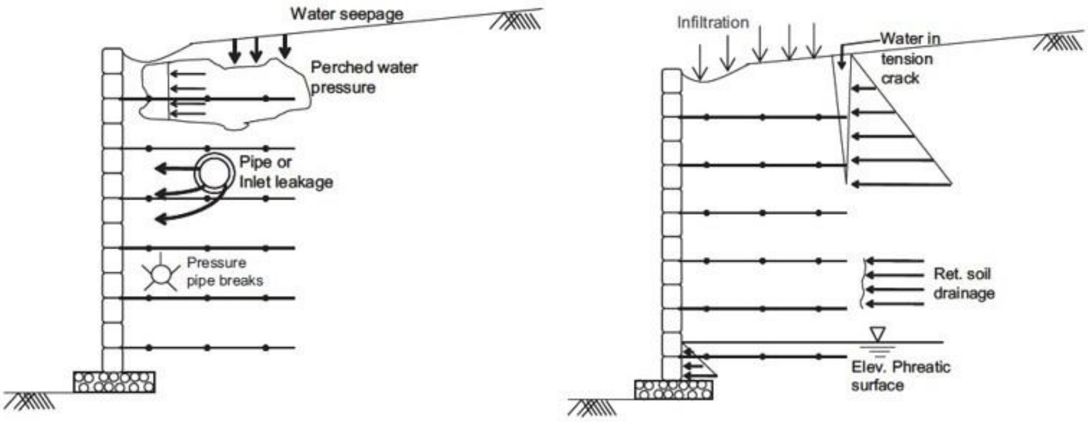

Figure 2.5 Failure mechanisms of GRS walls induced by water (Koerner and Koerner, 2013)

The western part of Japan was struck by Typhoon No. 23 in October 2004. Infrastructures over a wide area in Kansai were damaged severely. The accumulated rainfall was 226 mm while the maximum intensity was 10 mm/hr. Shibuya et al. (2007) investigated a failure of a large reinforced earth wall with a maximum height of about 23 meters that took place in a mountainous area. Figure 2.6 enunciates the scenario of the wall failure. The backfill material has a fines content larger than 25%. The wall failure may be attributed to simultaneous occurrence of several causes, including the concentration of in-soil seepage and surface water that flows into the failure zone, the relatively low permeability of the embankment, the poor drainage behind the wall, and the softening characteristic of the foundation soil as sheared undrained. It was concluded that drainage system should take care not only the wall but also the embankment behind and the wall should be placed on a foundation with larger bearing capacity (i.e., rock with SPT N-value larger than 50). Additionally, the short-term stability analysis of the wall should be employed considering the undrained condition upon designing.

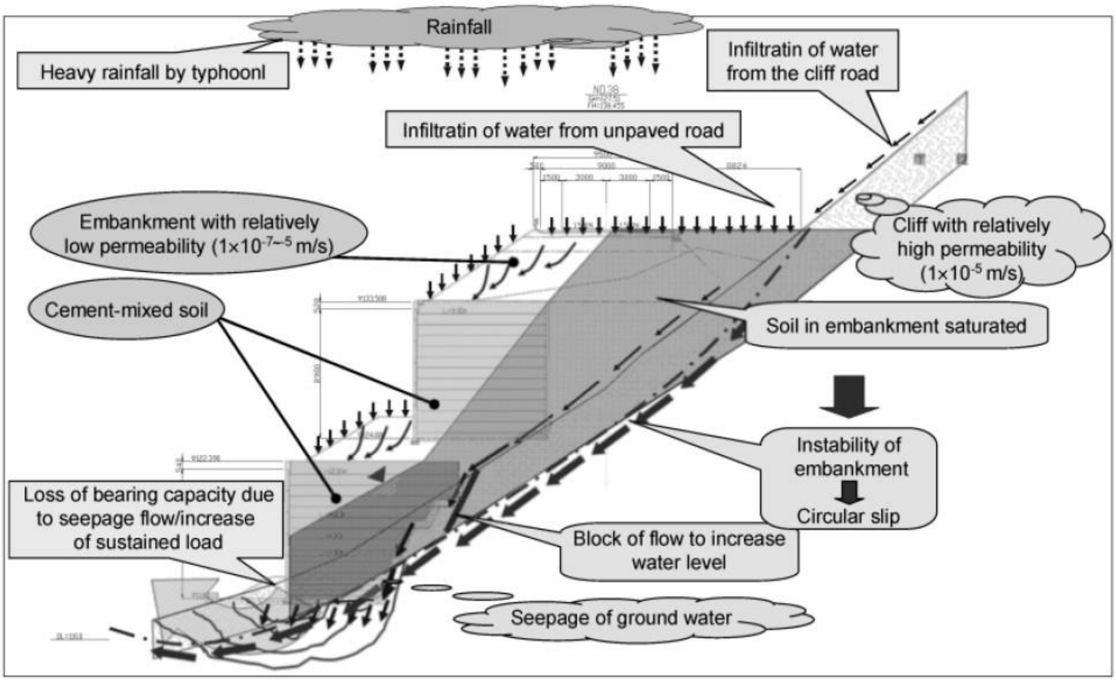

Figure 2.6 Scenario of the wall failure (Shibuya et al., 2007)

An excavated steep slope reinforced by geogrids was studied by Liu et al. (2012). A section of the slope collapsed soon after July 2, 2004, when Typhoon Ming-Du-Li passed over Taiwan. Heavy rainfall with maximum intensity at 166.5 mm/hr and 503 mm accumulated rainfall was recorded at a nearby precipitation station. The field observations led to the conclusion that the failure was closely related to rainfall. An impermeable clay layer was found underlying the reinforced slope. Moreover, the backfill was identified to have fines content of up to 42%. When abundant rainfall infiltrated into the reinforced slope, the infiltration obstructed by the impermeable clay and fine contents began to generate significant transient water pressure. The research indicated that the continuous rainfall led to the accumulation of pore water pressure in the GRS slope, followed by the loss of matric suction and soil shear strength; failure commenced subsequently.

Yoo et al. (2006) analyzed a failure of a geosynthetic reinforced segmental retaining wall that collapsed during a monsoon season in Korea. The local meteorological study indicated that the total precipitation was approximately 780 mm, which was rather higher than normal. The rainfall intensity was registered with a maximum rate of 155 mm/day. Laboratory tests pointed out that the backfill, completely decomposed granite soil, contains over 30% of fines. Finite element analysis was additionally conducted to examine pore water pressures in the soil. The results of the pore water pressure distributions during the rainfall period are presented in

Figure 2.7. The subsequent rather intense rainfall brought the matric suctions in the reinforced zone further down to single digit values upon the ceasing of rainfall. Also noted is the rise of the groundwater table above the wall base. The investigation revealed among other things that the low-quality backfill was mainly responsible for the wall failure, and the primary triggering factor was the rainfall infiltration.

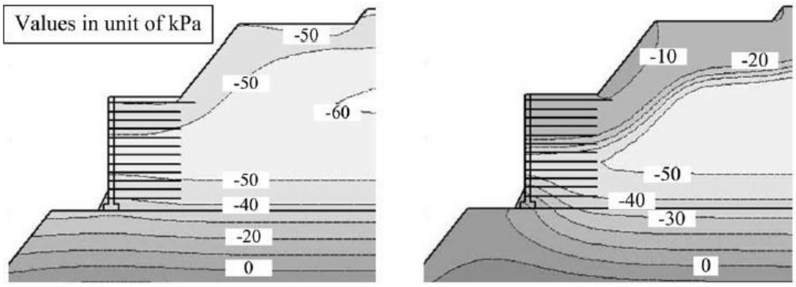

(a) June 1

(b) July 1

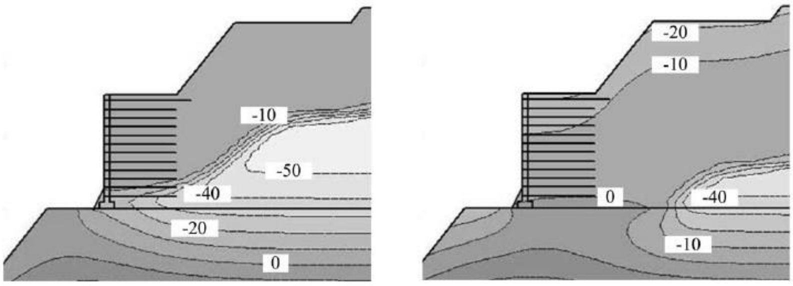

(c) July 20

(d) July 30

Figure 2.7 Pore water pressure distributions at different dates during rainfall period

(Yoo and Jung, 2006)

Yang et al. (2019) presented a comprehensive failure investigation of a GRS slope subjected to rainfall. The slope was 26-m high with four layers of geogrid reinforcement. The backfill soil contains more than 60% of fines and is considered as silty clay. Excessive deformation induced by heavy rainfall after typhoons were observed. The slope was pushed by the deformed weathered sandstone at the back and eventually collapsed in 2013 due to the accumulation of the rainfall (600mm). Figure 2.8 presents the development of the PWP along with the rainfall patterns. It was concluded that PWP was able to accumulate in the slope owing to the low draining capacity of the marginal backfill. Moreover, drainage system with flexible joints should be adopted in marginal backfilled GRS walls since excessive slope could occur upon the infiltration of rainfall.

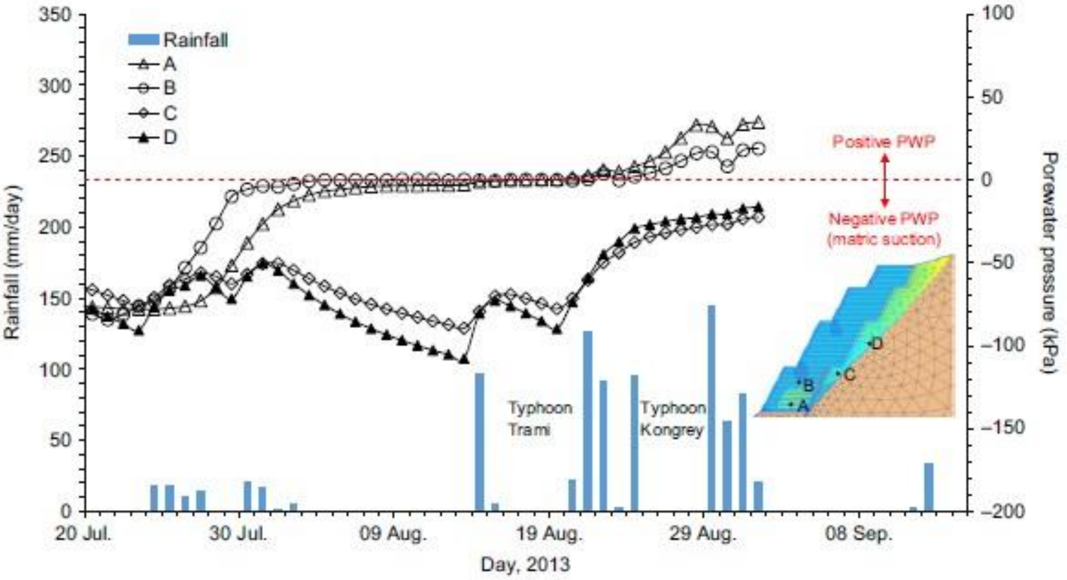

Figure 2.8 Development of the pore water pressure (Yang et al., 2019)

2.2.2 Model Tests

A series of centrifuge model tests was performed to simulate the poor drainage condition of a GRS wall after several days of heavy raining (Chen et al., 2007). The configuration of the model wall is presented in Figure 2.9. Clayey soil from Linkou area and a combination of geotextile with polymeric grids are used as the backfill and the reinforcement. The soil had a specific gravity, a plastic limit, and a liquid limit of 2.67, 23%, and 42%, respectively, and was classified as CL according to the USCS. The ultimate tensile strength of the reinforcement was 1.62 kN/m. Figure 2.10 shows the wall deformation modes found during the experiments. Various reinforcement arrangement was adopted to investigate the performance of the GRS wall under the worst climatic conditions. The results showed that GRS walls can be stable even in the worst climatic conditions if an appropriate reinforcement configuration is introduced. Specifically, decreasing the reinforcement spacing is much more effective than increasing the reinforcement length in terms of alleviation of wall displacements.

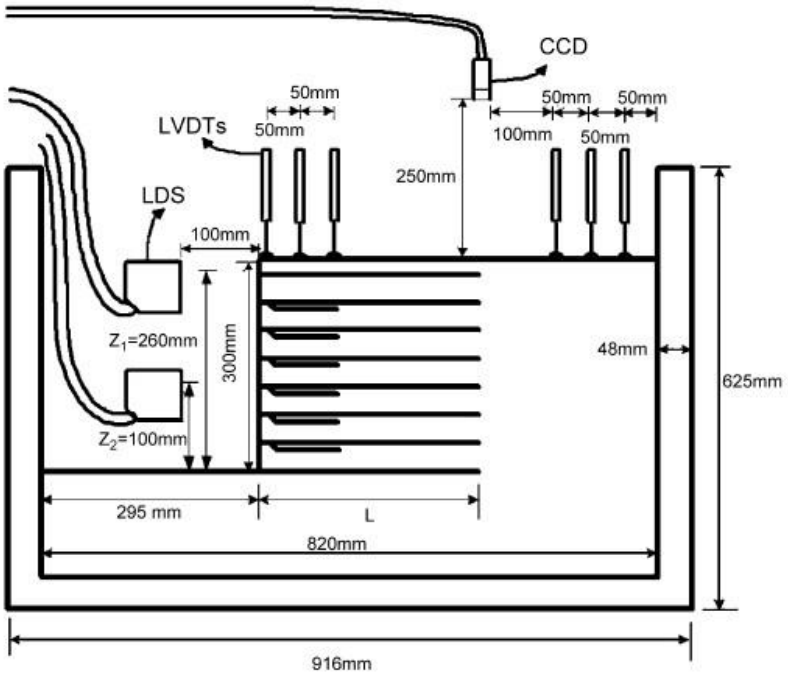

Figure 2.9 Configuration of the model wall (Chen et al., 2007)

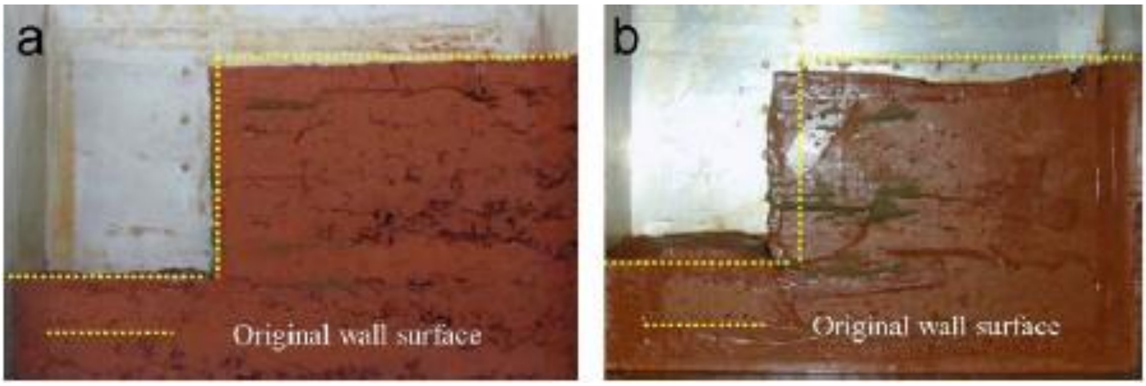

Figure 2.10 Wall deformation modes: (a) tilting; (b) bulging (Chen et al., 2007)

Centrifuge model tests were further conducted to convince the statement that the loss of interfacial shear resistance due to wetting of backfill is one of the possible reasons responsible for GRS wall failures (Balakrishnan and Viswanadham, 2016). A marginal soil with 21% fines was chosen as the backfill in the study. The testing soil had a maximum dry unit weight of 17.3 kN/m^3 and a friction angle of 34°. Geogrid was used as the reinforcement; notably, a thin non-woven geotextile was stuck to geogrid in the facing portion to prevent soil particles coming out of geogrid openings. Figure 2.11 shows the instrumentation of the model tests. Excessive wall displacements were found and tension cracks were observed to take place right behind the reinforced zone if the reinforcement strength was not enough, as shown in Figure 2.12.

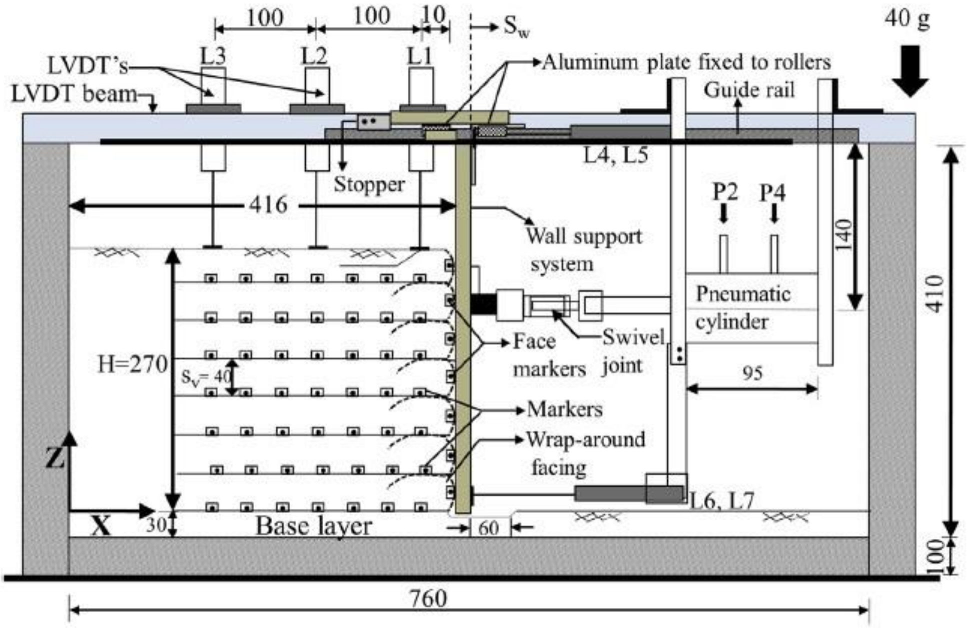

Figure 2.11 Cross-section view of the centrifuge model test instrumentation (Balakrishnan and Viswanadham, 2016)

doi:10.6342/NTU201901530

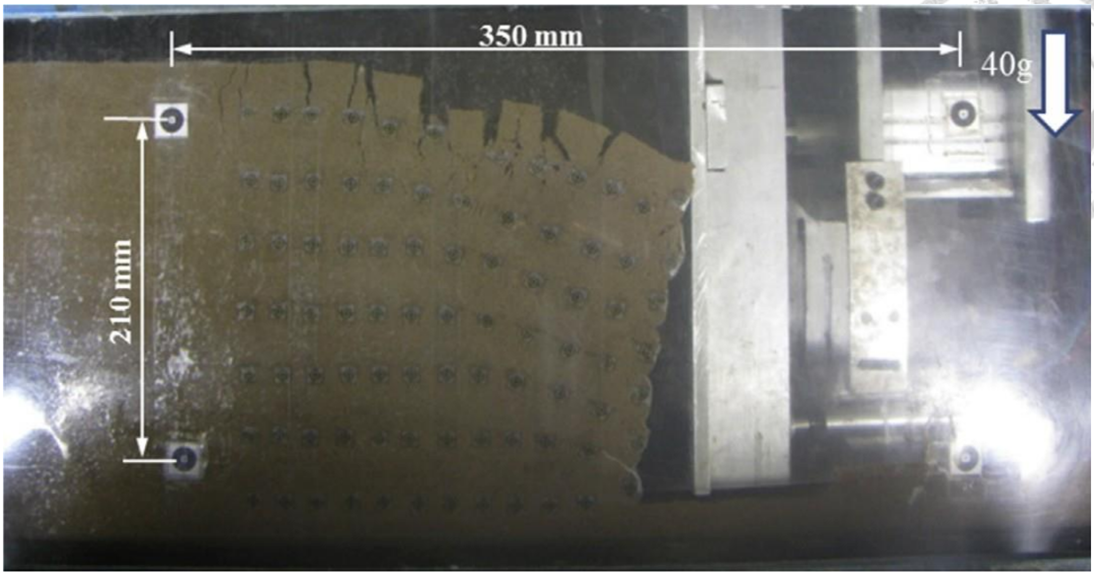

Figure 2.12 Tension cracks inspected during the tests (Balakrishnan and Viswanadham, 2016)

Gallage et al. (2012) conducted model tests of GRS slopes with different slope angles subjected to rainfall. The backfilled silty sand which contains 17% fines content had a maximum dry density and a specific gravity of 1.725 g/cm^3 and 2.75, respectively. The slopes were subjected to rainfall with an approximate intensity of 40 mm/hr. Figure 2.13 presents the location of the sensors and Figure 2.14 shows the change of the pore water pressure and the volumetric water content throughout the test. The results indicated that the slopes with the inclination larger than the friction angle of the backfill can be stable until the suction was decreased by the infiltration of the rainwater into the slope; failures in slopes with gentler inclination were initiated by the development of the positive pore water pressure near the toe and is rather slow and progressive. Both results led to the conclusion that rainfall infiltration is a critical factor to the wall stability.

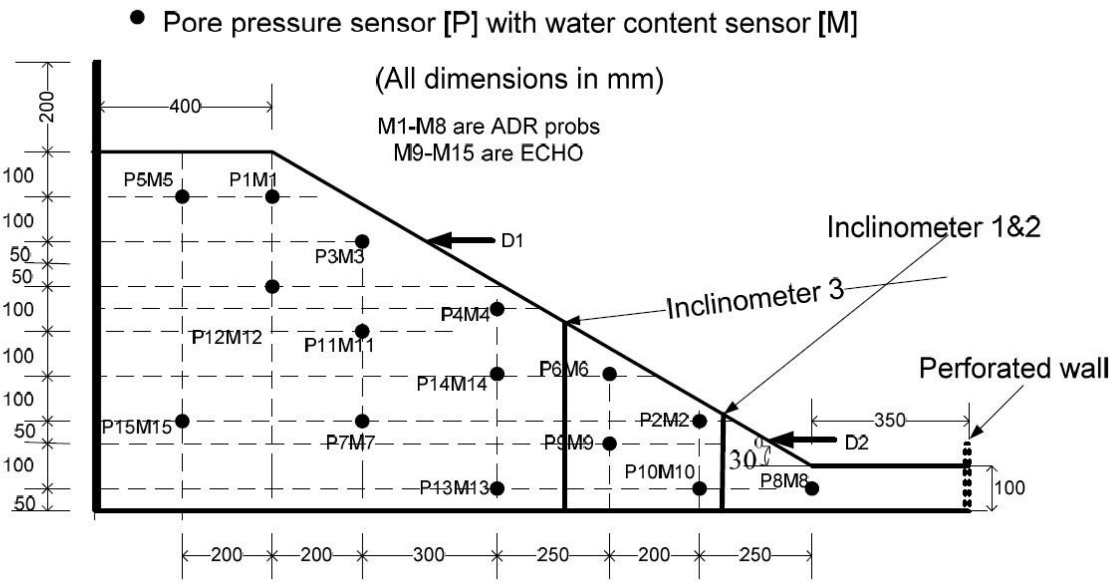

Figure 2.13 Sensor locations in the model tests (Gallage et al., 2012)

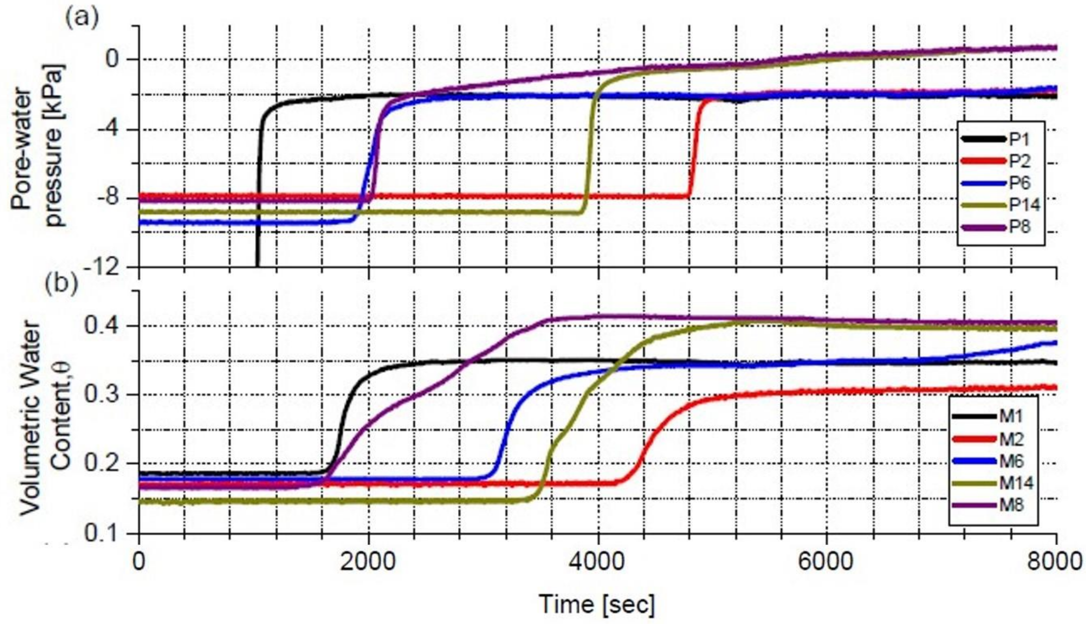

Figure 2.14 Change of PWP and VWC (Gallage et al., 2012)

Yoo et al. (2013) carried out a series of model tests to investigate the effect of rainfall in the performance of geosynthetic reinforced soil wall. The schematic sectional view and a photo of model GRS wall are shown in Figure 2.15. Decomposed granite soil (DGG) and non-woven geotextile were used as the backfill soil and reinforcement respectively. The backfill soil was a non-plastic poorly-graded sand, with a maximum unit weight of 19 kN/m^3. A rainfall intensity of 56.2 mm/hr and total given precipitation of 450 mm were adopted. The results of the laboratory tests are presented in Figure 2.16; 1 mm wall displacement was measured while the pore water registered during the wetting period was as great as 4 kPa. The research suggested that the cycles of wetting and drying associated with a heavy rainfall may induce additional wall displacement and reinforcement strains in GRS walls. It can be concluded that the rainfall intensity is a governing factor for the performance of a GRS wall during rainfall infiltration.

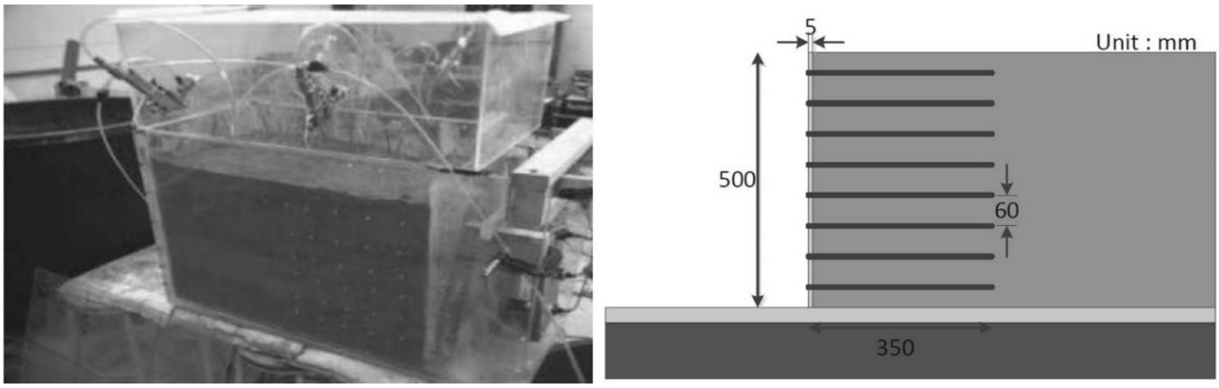

Figure 2.15 A photo and the schematic sectional view of the GRS wall (Yoo et al., 2013)

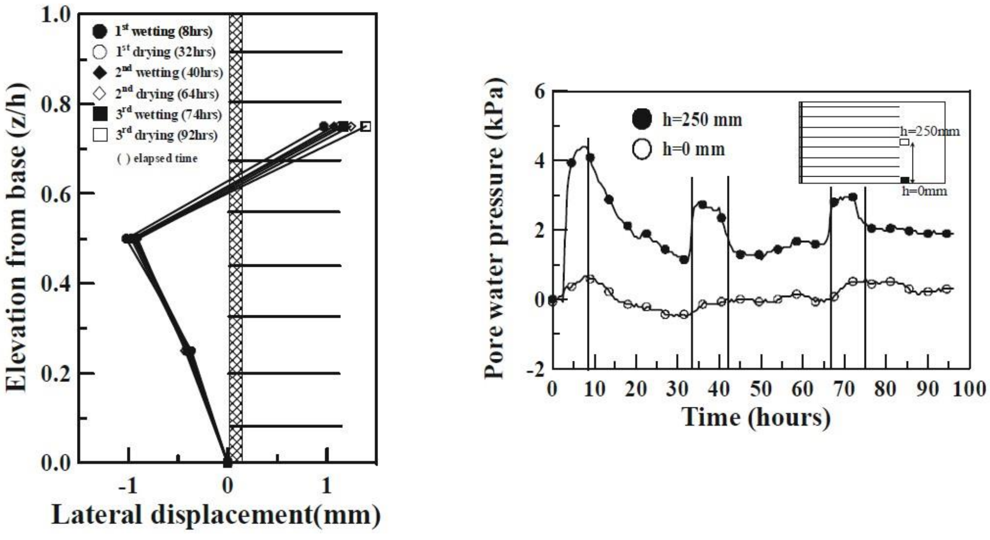

(a) (b)

Figure 2.16 Results: (a) wall displacement; (b) pore water pressure (Yoo et al., 2013)

2.2.3 Full-scale Tests

Full-scale laboratory model tests concerning the effect of rainfall infiltration were also carried out by Portelinha et al. (2013) and Portelinha and Zornberg (2017). Figure 2.17 presents the schematic view of the model wall and Figure 2.18 shows a full scale GRS wall test, done to monitor the hydraulic and mechanical responses. The model wall was 1.8 m and 1.55 m in height and width respectively. The backfill material includes 44% fines and has a saturated hydraulic conductivity of 4.9×10^{-7} m/s. A polyester needle-punched nonwoven geotextile was used as reinforcement to provide tensile strength and drainage. Vertical spacing of 30 cm was adopted in the study. The results illustrated that nonwoven geotextiles did provide internal drainage, which diverted approximately 25% of the water volume. Additionally, the infiltration of the rainfall led to a significant increase in reinforcement strains and wall displacement. In particular, the increase was caused by pore water accumulation, which resulted in an increase in the unit weight of the backfilled soil.

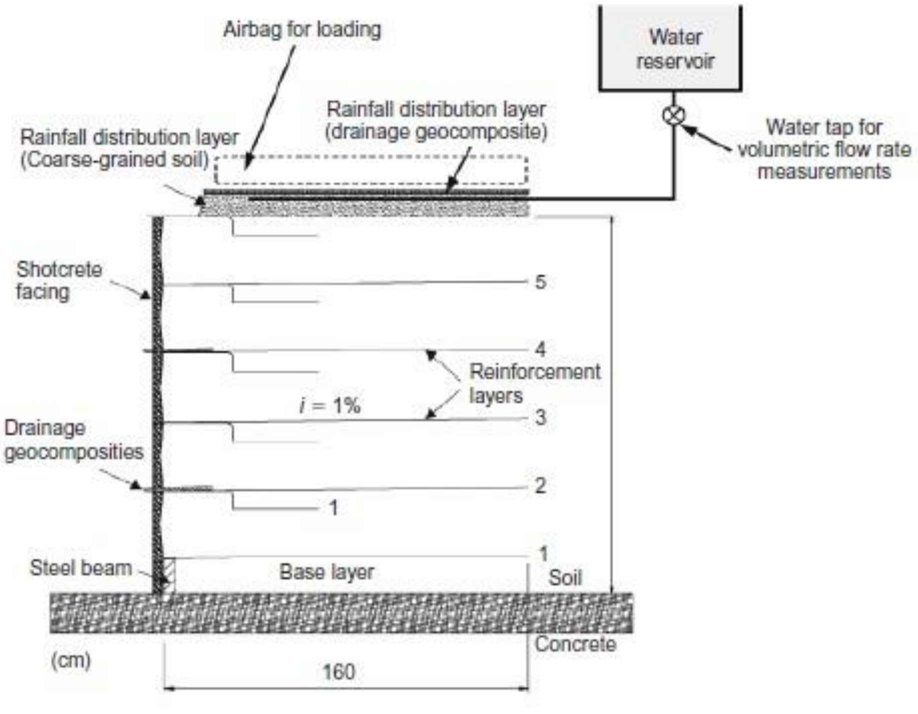

Figure 2.17 Schematic view of the full-scale model (Portelinha et al., 2013)

Figure 2.18 Front view of the full-scale GRS wall (Portelinha and Zornberg, 2017)

2.2.4 Numerical Study

Bhattacherjee and Viswanadham (2015) discussed the effect of geosynthetic reinforcement to slopes under rainfall conditions. Numerical simulation was performed with the rainfall duration of 24 hours and the intensity of 2-80 mm/hr. Figure 2.19 presents the distribution of the PWP after rainfall in unreinforced and reinforced slope. The study concluded that reinforcement can provide drainage, restrain wall displacement, and enhance the wall stability.

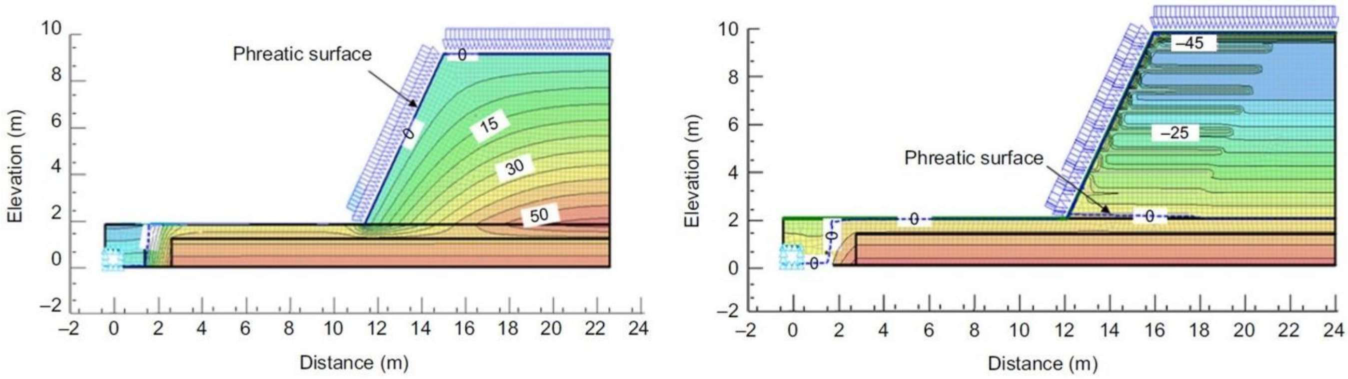

Figure 2.19 Distribution of PWP after rainfall (Bhattacherjee and Viswanadham, 2015)

Consider the failure mechanisms of marginal backfilled GRS walls, Yang et al. (2018) and Thou et al. (2015) proposed sand cushion as the improved method for marginal backfilled GRS walls. The schematic view of sand cushion is shown in Figure 2.20. The application of sand cushion can increase the interface friction between the soil and the geogrid. Moreover, the sand cushion can provide drainage functions which can effectively enhance the slope stability of GRS walls. The system stability increased with the increase of sand cushion thickness; however, the function of sand cushion reached a maximum value when about 20% of marginal backfill was replaced with sand as sand cushions. Figure 2.21 presents the effect of the adoption of sand cushions in a model GRS wall.

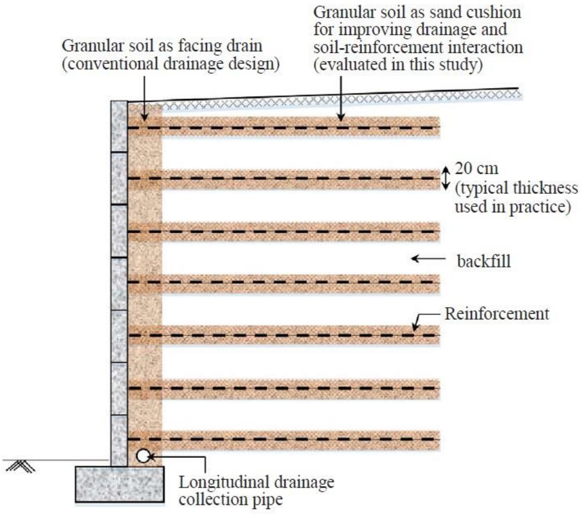

Figure 2.20 Schematic view of sand cushion (Yang et al., 2018)

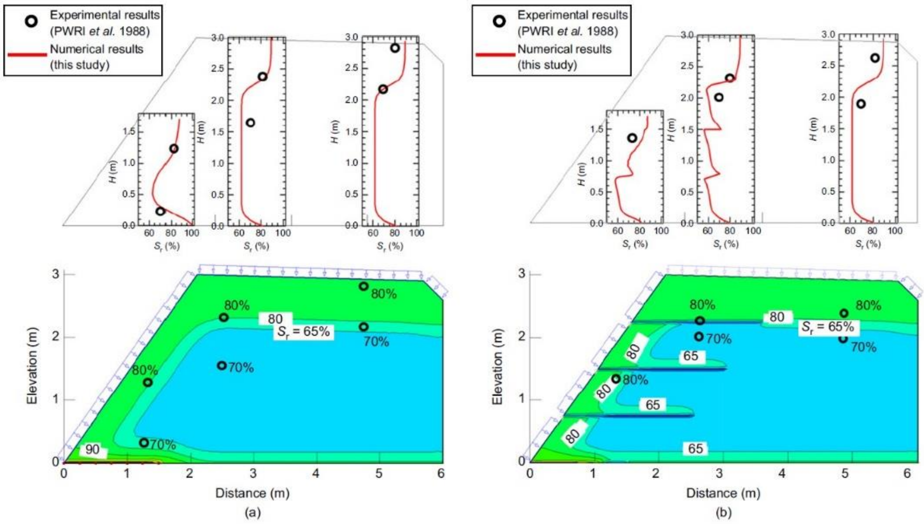

Figure 2.21 Effect of the adoption of sand cushion (Thou et al., 2015)

Preceding studies, including field investigation and laboratory tests, drew to the conclusion that the behavior of GRS walls is closely related to the matric suction of the backfilled soil. Furthermore, rainfall infiltration led to the accumulation of the pore water pressure, followed by the loss of matric suction and soil shear strength. In addition, the decrease of the interface shear strength resulted from rainfall infiltration is one of the causes of GRS wall failures. However, the application of geosynthetics can provide effective reinforcement to the wall; meanwhile, the displacement of the wall is successfully alleviated. Most importantly, geosynthetics is capable of dissipating the pore water pressure, which is critical to the wall stability.

2.3 Model Tests and Scaling Laws

Model tests are purported to the understanding of the mechanical behavior in the prototype by investigating the results from small scale physical models with a reduced number of variables. Both similitude law and dimensional analysis play important roles in the reduced scale model tests; it assures the feasibility and reliability of the test results. The similitude law and dimensional analysis will be introduced in the subsequent sections. The use of dimensional analysis on important variables of this research is also discussed.

2.3.1 Similitude Law

Model tests are designed to understand the mechanical behavior of the prototype by constructing a reduced scale model of the prototype to simulate the true performance of the prototype. The similitude law defines the relationship between the physical quantities of the model and those of the prototype. The similitude law states that the relation between the model and the prototype should satisfy three similarities, namely, geometric similarity, kinematic similarity, and dynamic similarity (Langhaar, 1951).

doi:10.6342/NTU201901530

The similarity of the shape of the model and prototype is considered as the geometric similarity. More specifically, all the corresponding parts of the model and the prototype should be the same. Geometric similarity can be expressed in Equation 2.6:

$$\frac{L_p}{L_m} = \lambda \tag{2.6}$$

where L = length, subscript p is the prototype, subscript m is the model, and λ = scaling factor. Figure 2.22 is a schematic view of a slope in the prototype and its model. The ratios of the slope height H in the prototype to that in the model and the ratio of the length of the slope L in the prototype to that in the model are constants λ. Besides, the slope angle θ is the same in both the prototype and the model. Thus, Figure 2.22 satisfies the geometric similarity.

The kinematic similarity indicates a status where the motion and the displacement in the prototype are similar to that in the model. Likewise, the dynamic similarity denotes the similarity of the forces acting on the prototype slope and the model slope. The dynamic similarity would be satisfied once the ratio of forces acting on corresponding points or surfaces of the prototype and the model remains constant. Figure 2.22 also meets dynamic similarity since the ratio of the driving forces, F_{dp} and F_{dm}, in the prototype and the model respectively, and the ratio of the resistance forces, F_{rp} and F_{rm}, are constant.

doi:10.6342/NTU201901530

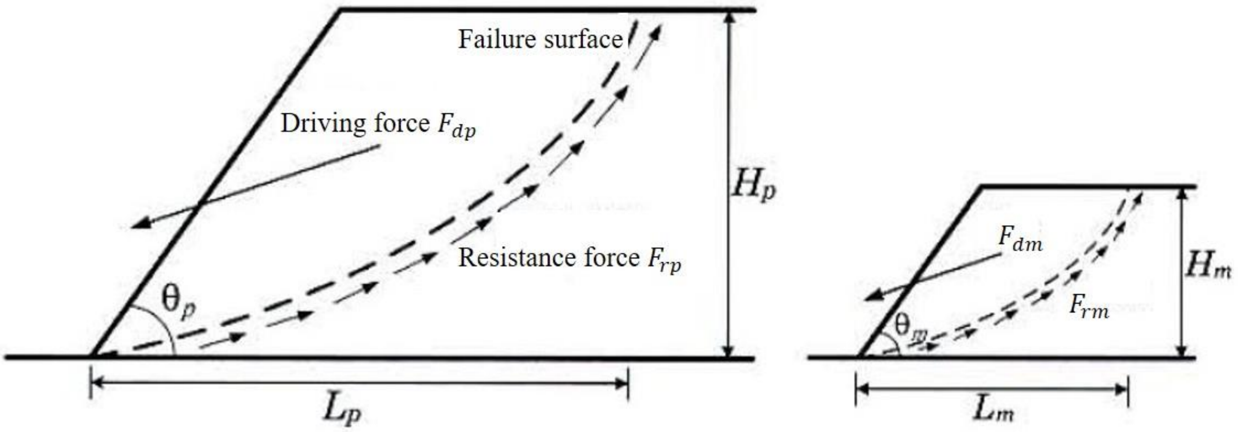

Figure 2.22 Schematic view of a prototype slope and its model (Chen and Chi, 2010)

2.3.2 Dimensional analysis

Dimensional analysis plays a vital role in the process of conducting a model test. Variables needed for the analysis can be reduced to the target variables by decomposing them into several dimensionless products. The concept of the dimensional analysis is based on the Buckingham’s Theorem (Buckingham, 1914), which states that if there is a function independent to the basic unit dimensions, then it can be written into several dimensionless products. The theorem can be expressed as Equation 2.7 and 2.8:

$$\Phi(\Pi_1,\Pi_2,\cdots\Pi_{n\text{-}k}) = 0 \tag{2.7}$$

$$\Pi_1 = \phi(\Pi_2,\cdots\Pi_{n\text{-}k}) \tag{2.8}$$

where k = number of fundamental dimensions required to describe the n variables, Π = independent quantities of groups that can be expressed. For example, assume Π_1, $\Pi_2,\cdots\Pi_{n\text{-}k}$ are physical quantities, let Π_1 be length, Π_2 be mass, and Π_3 be time. Π_1, Π_2, and Π_3 are three independent basic unit dimensions $(r = 3)$. In this case, the other $(n - 3)$ variables (i.e., force and velocity) can be expressed by dimensionless products of Π_1, Π_2, and Π_3 (Langhaar, 1951).

This research aims to understand the performance of GRS walls under rainfall condition. Thus, the scaling down of the rainfall, which is referred to as the quantity of flow, is considered as the most important issue. Let the quantity of flow, q (volume per unit time), be a function of several independent variables, as Equation 2.9 (Cargill and Ko, 1983):

$$q = f(l, A, \Delta H, g, \kappa, \rho, \mu) \tag{2.9}$$

where l = length over which the potential difference in head, ΔH, is dissipated, A = cross-sectional area of the soil mass conducting the flow, g = gravitational constant, κ = soil physical permeability, ρ = mass density of the fluid and μ = fluid viscosity. Subsequently, let the representative dimensions be ρ, l, and g for mass (M), length (L), and time (T), respectively, using the recurring set of the equations we can obtain a relationship shown in Equation 2.10:

$$\Pi = \frac{qul}{\rho g \kappa A \Delta H} \tag{2.10}$$

For complete similarity between any model and its prototype, corresponding Π terms must be equal, as shown in Equation 2.11 and 2.12:

$$\Pi_p = \Pi_m \tag{2.11}$$

$$\left(\frac{qul}{\rho g \kappa A \Delta H} \right)_p = \left(\frac{qul}{\rho g \kappa A \Delta H} \right)_m \tag{2.12}$$

Since the same porous material and fluid are used for both the prototype and the model test in this research, and the gravitational force is not scaled, we can get Equation 2.13:

$$\frac{\rho_\mathrm{p}}{\rho_\mathrm{m}} = \frac{\kappa_\mathrm{p}}{\kappa_\mathrm{m}} = \frac{\mu_\mathrm{p}}{\mu_\mathrm{m}} = 1 \tag{2.13}$$

From Equation 2.12 and 2.13, we can obtain the scaling factor of the flow, q, and the time, t, as shown in Equation 2.14 and 2.15:

$$\psi_q = \frac{A_p \Delta H_p l_m}{A_m \Delta H_m l_p} = N^2 \tag{2.14}$$

$$\psi_t = \frac{\rho_m g_m \kappa_m \mu_p x_p}{\rho_p g_p \kappa_p \mu_m x_m} = N \tag{2.15}$$

The often used scaling factors for modeling of geosynthetic materials are summarized in Table 2.3 (Viswanadham, 2004). Notably, the strain in the model test and its prototype remains the same, the geometric parameters(i.e., height, width, and length) should be scaled down N times, and the tensile strength of the reinforcement, T, should be scaled down N^2 times.

Table 2.3 Common scaling factors for modeling of GRS structures (Viswanadham et al., 2004)

Parameters	Scaling factors	
	1g model	Ng model
Geosynthetic stain ε_g (%)	1	1
Length a, b, t (m)[a]	$1/N$	$1/N$
Displacement δ (mm)	$1/N$	$1/N$
Cross-section area of rib A (m^2)[b]	$1/N^2$	$1/N^{2c}$
Cross-section area of rib/unit length A' (m)[b]	$1/N$	$1/N$
Tensile strength T_g (kN/m)	$1/N^2$	$1/N^{2c}$
Secant modulus J_g (kN/m)	$1/N^2$	$1/N$
Pull-out force P (kN)	$1/N^3$	$1/N^2$
Bond stress τ_b (kN/m^2)	$1/N$	1
Soil-geosynthetic friction angle ϕ_{sg} (deg)	1	1

[a] a, b, t: Geometric dimensions in longitudinal and transverse directions for geogrid and in the case of geogrid t thickness of rib or thickness of geotextile

[b] Not valid for geotextiles

[c] $A_m/A_p = 1/N^2$; $(T_g)_m/(T_g)_p = 1/N$

Chapter 3 Material Testing and Properties

3.1 Test Layout

This research carried out a series of reduced scale model tests to investigate the performance of geosynthetic reinforced wall under rainfall conditions. Before conducting model tests, it is essential to understand the properties of the materials used in this research. In this section, in addition to the elaboration of material testing procedures, the results of the material property tests are presented herein. Figure 3.1 shows the test methods to determine the properties of soil and reinforcement used in this study.

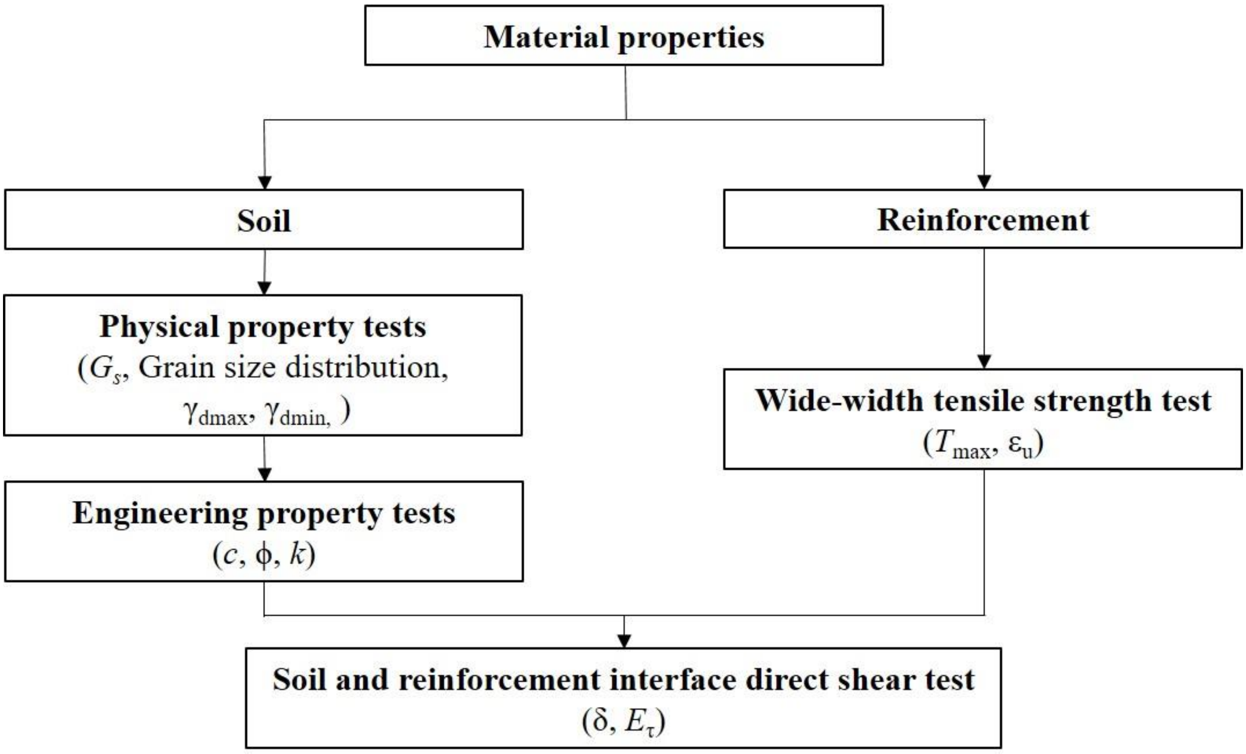

Figure 3.1 Material property tests layout

doi:10.6342/NTU201901530

3.2 Soil Physical Properties

Vietnam quartz sand and silty sand (i.e. Vietnam quartz sand with twenty percent Kaolinite) were used in this study. In this study, the pycnometer test, sieve analysis, hydrometer test, and relative density test were conducted to obtain the physical properties of the testing soil. The grain size distribution curve and the soil classification were subsequently acquired. The appearance of the testing soil is shown in Figure 3.2.


(a) (b)

Figure 3.2 Testing soil: (a) Vietnam quartz sand; (b) Vietnam quartz sand with 20% Kaolinite

3.2.1 Specific Gravity Test

The specific gravity of the test soil was obtained by the specific gravity test according to ASTM D854. The value of the specific gravity was obtained from the average of three tests. Figure 3.3 shows the equipment of the specific gravity test, and the test results are presented in Table 3.1. The specific gravity of the pure sand and the silty sand is 2.65 and 2.62, respectively.

Table 3.1 Results of the specific gravity test

Soil type	Test 1	Test 2	Test 3	Average G_s
Pure Sand	2.65	2.65	2.66	**2.65**
Silty Sand	2.63	2.60	2.62	**2.62**

doi:10.6342/NTU201901530

Figure 3.3 Equipment of the specific gravity test

3.2.2 Sieve Analysis Test

Sieve analysis was conducted to obtain the soil grain size distribution curve in accordance with ASTM D293. Figure 3.4 shows the equipment used for the sieve analysis. Sieves No. 4, No. 10, No. 20, No. 40, No. 60, No. 100, and No. 200 were used in the test. Table 3.2 summarizes the test results, and Figure 3.5 shows the grain size distribution curve of the sand. Furthermore, the effective size (D_{10}) of the testing soil is 0.16 mm while the coefficient of gradation (C_c) and the uniformity coefficient (C_u) is 0.89 and 0.66, respectively. Hence, one of the test soil, Vietnam quartz sand, is classified as poorly graded sand (SP) according to the Unified Soil Classification System (USCS). The grain size distribution curve of the silty sand was obtained from the hydrometer tests.

Figure 3.4 Equipment for the sieve analysis

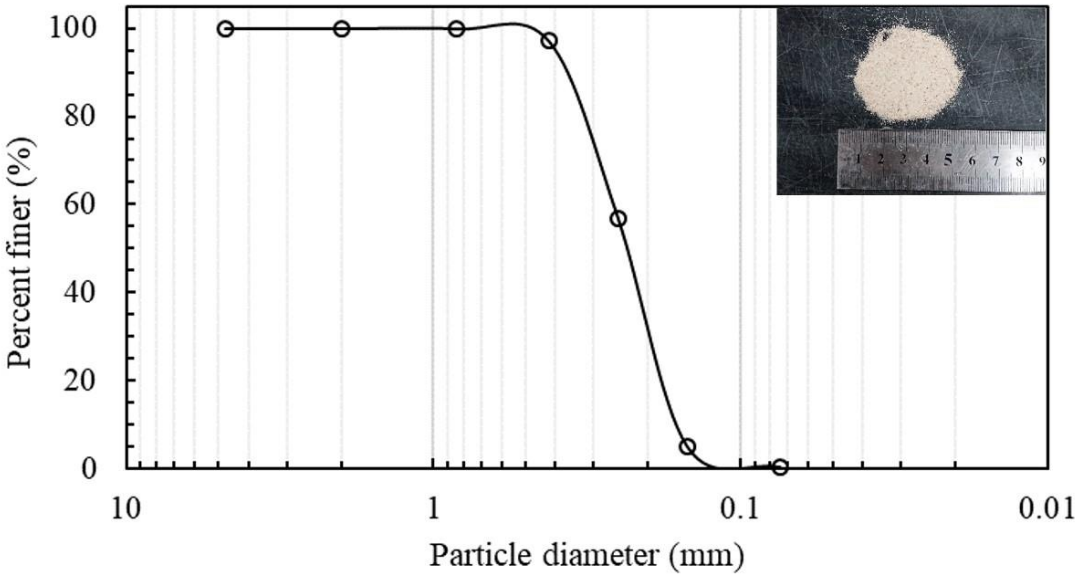

Figure 3.5 Grain size distribution curve of Vietnam quartz sand

doi:10.6342/NTU201901530

Table 3.2 Results of the sieve analysis

Sieve No.	Opening Size (mm)	Percentage Retained (%)	Percent Finer (%)
4	4.75	0.00	100.00
10	2.00	0.00	100.00
20	0.84	0.06	99.94
40	0.42	2.78	97.16
60	0.25	40.27	56.89
100	0.149	51.90	4.99
200	0.074	4.75	0.24
Pan	-	0.24	0.00

3.2.3 Hydrometer Test

According to ASTM D7928, hydrometer test was carried out to determine the grain size distribution curve for the silty sand of which the particle size is smaller than No. 200 sieve. A hydrometer and a sedimentation cylinder, as shown in Figure 3.6, was used to perform the hydrometer test. Figure 3.7 shows the grain size distribution curve of the testing soil (i.e., Vietnam quartz sand with 20% Kaolinite). The segment that has a particle diameter smaller than 0.075 mm was obtained from the hydrometer test, whereas the remainder was obtained from sieve analysis. The test soil is classified as silty sand (SM) according to the Unified Soil Classification System (USCS).

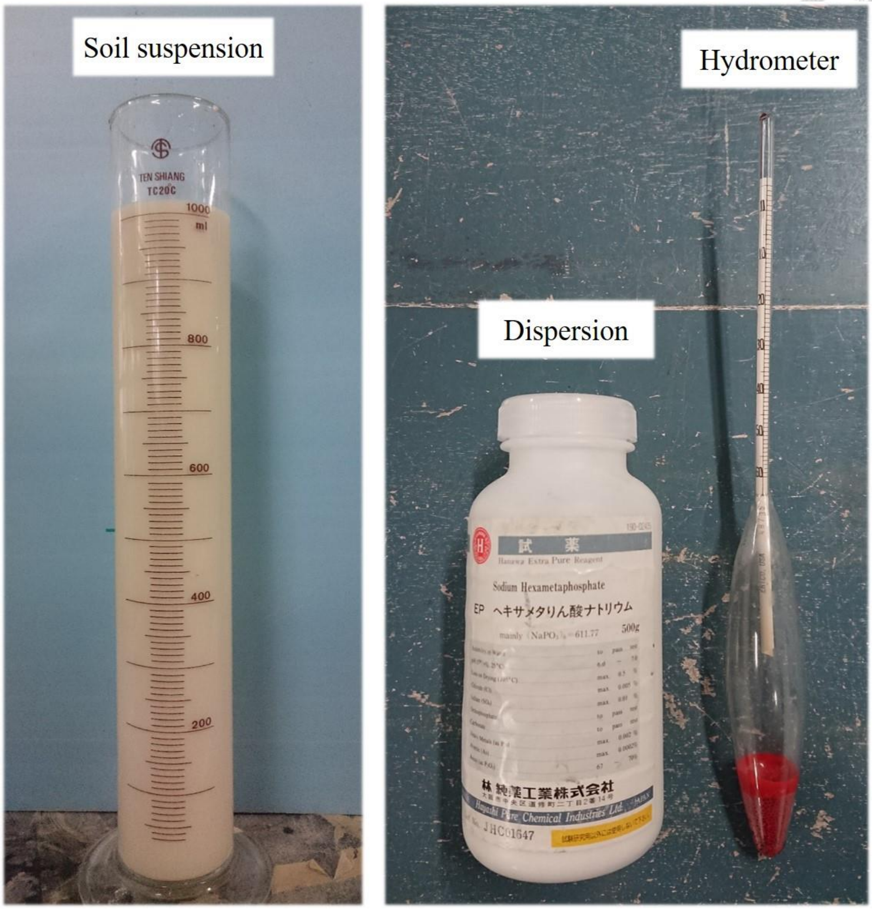

Figure 3.6 Apparatus of the hydrometer test

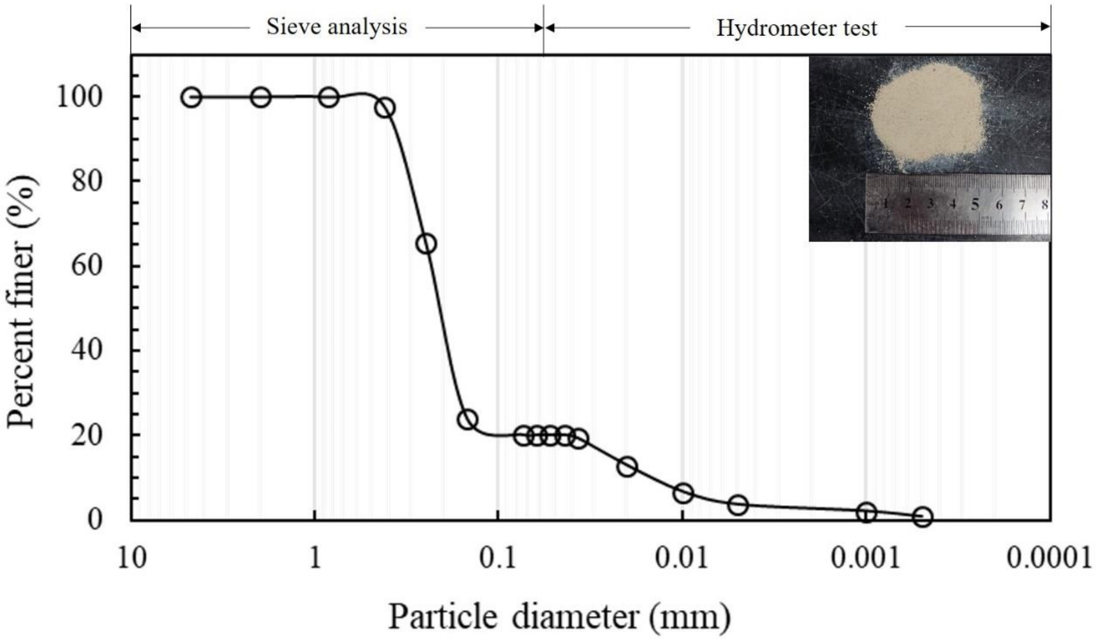

Figure 3.7 Grain size distribution curve of silty sand

3.2.4 Relative Density Test

Relative density can be calculated from the maximum and minimum dry unit weight or void ratio, as shown in Equation 3.1:

$$D_r = \frac{\gamma_{\mathrm{d}} - \gamma_{\mathrm{d,min}}}{\gamma_{\mathrm{d,max}} - \gamma_{\mathrm{d,min}}} \times \frac{\gamma_{\mathrm{d,max}}}{\gamma_{\mathrm{d}}} = \frac{e_{\max} - e}{e_{\max} - e_{\min}} \tag{3.1}$$

where D_r = relative density, $\gamma_{\mathrm{d,max}}$ = maximum dry unit weight, $\gamma_{\mathrm{d,min}}$ = minimum dry unit weight, γ_{d} = dry unit weight at the target relative density, $e_{\max}$ = maximum void ratio, $e_{\min}$ = minimum void ratio, and e = void ratio at the target relative density. The maximum and minimum dry unit weight and void ratio were obtained using a vibrating deck according to ASTM D4523. Figure 3.8 shows the setup of the apparatus used for the relative density test. A mold with a volume of 2831 cm^3 was filled with oven-dried testing soil by pluviation method to achieve the loosest state; the minimum dry unit weight and the maximum void ratio can be attained. The densest state was executed by mounting the mold on the vibratory table with a vertical surcharge (2±0.2 $\mathrm{lb/in}^2$). The volume at the densest state can thus be calculated by measuring the decrease of height after vibration; the maximum dry unit weight and the minimum void ratio can be known subsequently.

The study obtained the friction angle of sand by applying normal stress on samples at different relative density. The results indicate that the friction angle of sand slightly increases with the increase of relative density. Furthermore, the wetting process poses infinitesimal effect on the friction angle of sand with relatively high permeability. Therefore, the target density of D_r = 70% was selected for the GRS wall model using sand as backfill. Table 3.3 presents the results of the relative density test.

doi:10.6342/NTU201901530

Figure 3.8 Apparatus for relative density test

Table 3.3 Results of the relative density test of sand

ASTM	Loosest State		Densest State		Target State (D_r = 70%)	
Parameters	$\gamma_{d,min}$ (kN/m^3)	e_{max}	$\gamma_{d,max}$ (kN/m^3)	e_{min}	γ_d (kN/m^3)	e
Value	13.54	0.92	15.21	0.71	14.7	0.77

3.2.5 Compaction Test

Compaction test was carried out to determine the optimum water content and the maximum dry density of the testing soil (i.e., Vietnam quartz sand with 20% Kaolinite). The standard Proctor compaction test was performed according to AASHTO T99, using a 5.5 lb hammer with a free-falling distance of 12 in, as shown in Figure 3.9 . The specimen was prepared by conducting three levels of compaction with 25 blows each layer. Figure 3.10 shows the results of the compaction curve of the testing soil. The maximum dry density is 18.1 kN/m^3 while the optimum water content is 10.7%. In this study, the specimen was compacted at the optimum water content (10.7%) to 90% of the maximum dry unit weight, on the basis of the construction regulation which specifies the compaction has to be at least 90% maximum dry density at ±2% optimum water content.

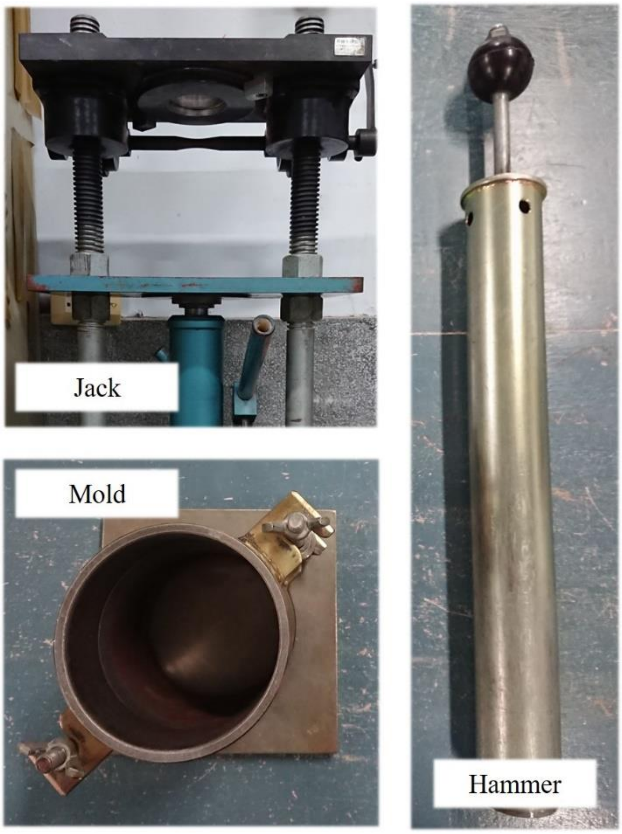

Figure 3.9 Equipment for the compaction test

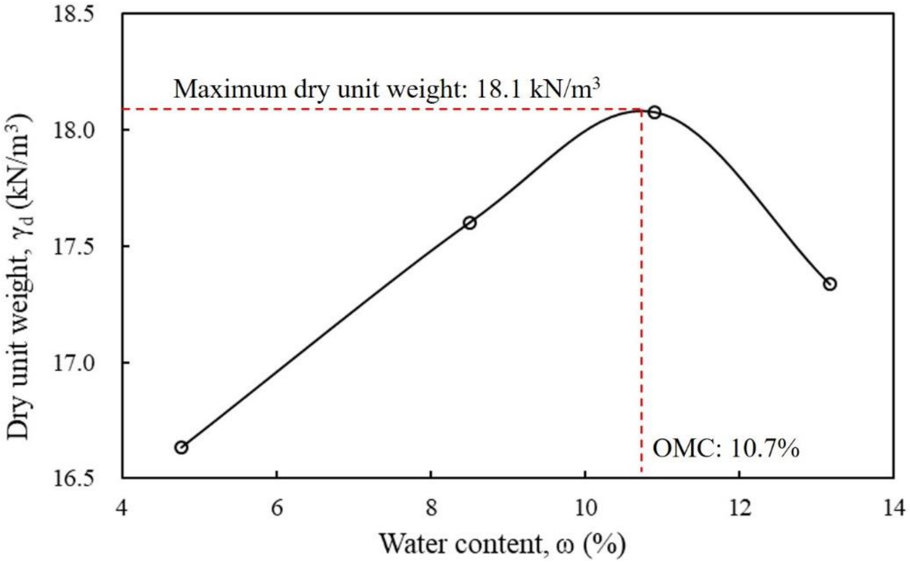

Figure 3.10 Compaction curve of the test soil

3.3 Engineering Properties of Testing Soil

In this study, permeability tests and triaxial tests were performed to determine the engineering properties, the permeability and shear strength, of the test sand and silty sand. Specifically, constant head test and consolidated drained triaxial test were conducted for the testing soil with relatively large permeability (i.e., Vietnam quartz sand) while the falling head test and the consolidated undrained triaxial test were conducted for the testing soil with relatively low permeability (i.e., Vietnam quartz sand with 20% Kaolinite).

3.3.1 Constant Head Test

The permeability of the test sand was obtained from the constant head permeability test, conducted in accordance with ASTM D5084. The permeability can be determined by Darcy's Law, as shown in Equation 3.2:

$$q = Av = Aki = Ak\frac{h}{L} \tag{3.2}$$

where q = discharge, A = cross-sectional area perpendicular to the flow of water, v = velocity of the flow, k = permeability of the testing soil, i = hydraulic gradient, L = length of the specimen which water seeps through, and h = head difference.

Figure 3.11 shows the setup for the constant head permeability test. The specimen was mounted on a steel platform with an O-ring and Vaseline between the specimen and the platform to prevent the leakage of water. Two porous disks were capped at the top and bottom of the specimen, and non-woven geotextiles were also placed between the porous disk and the specimen to prevent soil particles from leaking out.

doi:10.6342/NTU201901530

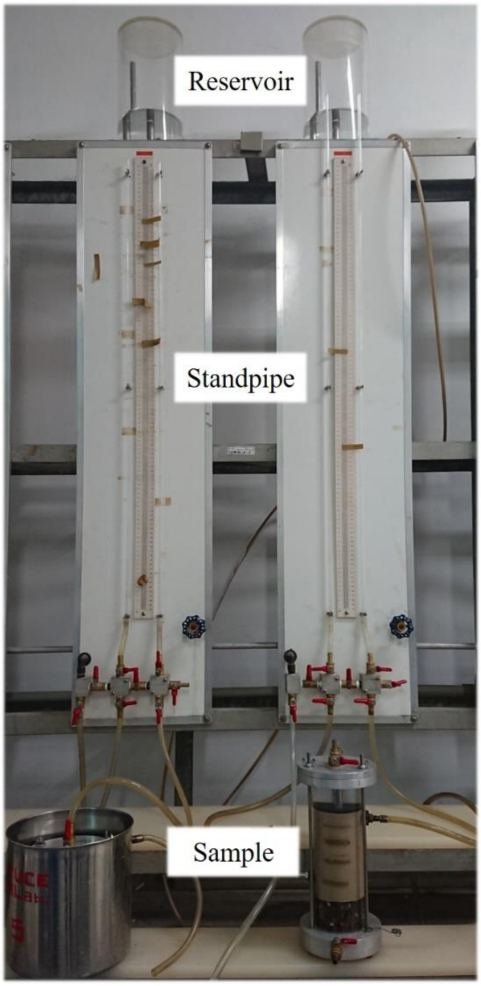

Figure 3.11 Apparatus for permeability tests

3.3.2 Falling Head Test

Falling head permeability test was conducted for silty sand. The permeability of the testing soil can be determined from Equation 3.3:

$$k = \frac{La}{A(t_2 - t_1)} \ln\left(\frac{h_1}{h_2}\right) \tag{3.3}$$

Figure 3.11 shows the apparatus for the falling head permeability test, and the test was carried out according to ASTM D5084. The specimen was vacuumed to be saturated before the test started. The permeability of the silty sand can be determined by measuring the head loss of water between a certain time interval. The results of the permeability tests are presented in Table 3.4.

doi:10.6342/NTU201901530

Table 3.4 Results of the permeability tests

k (m/s)	Test 1	Test 2	Test 3	Average
Pure Sand	5.3×10^{-4}	5.5×10^{-4}	5.2×10^{-4}	**5.3×10^{-4}**
Silty Sand	3.9×10^{-6}	3.9×10^{-6}	3.8×10^{-6}	**3.9×10^{-6}**

3.3.3 Consolidated Drained Triaxial Test

Consolidated drained triaxial test was carried out to investigate the shear strength of the testing soil. The test apparatus, including the triaxial compression chamber, the axial loading device, and the pressure controlling devices, are shown in Figure 3.12. The preparation of the specimen, as shown in Figure 3.13, and the testing procedure were referred to ASTM D7181. Specifically, the specimen is allowed to drain during the shearing phase. Mohr circles along with the friction angle of the testing soil can be attained from the tests, and the results are presented in Figure 3.14. The friction angle of the test sand is 37°.

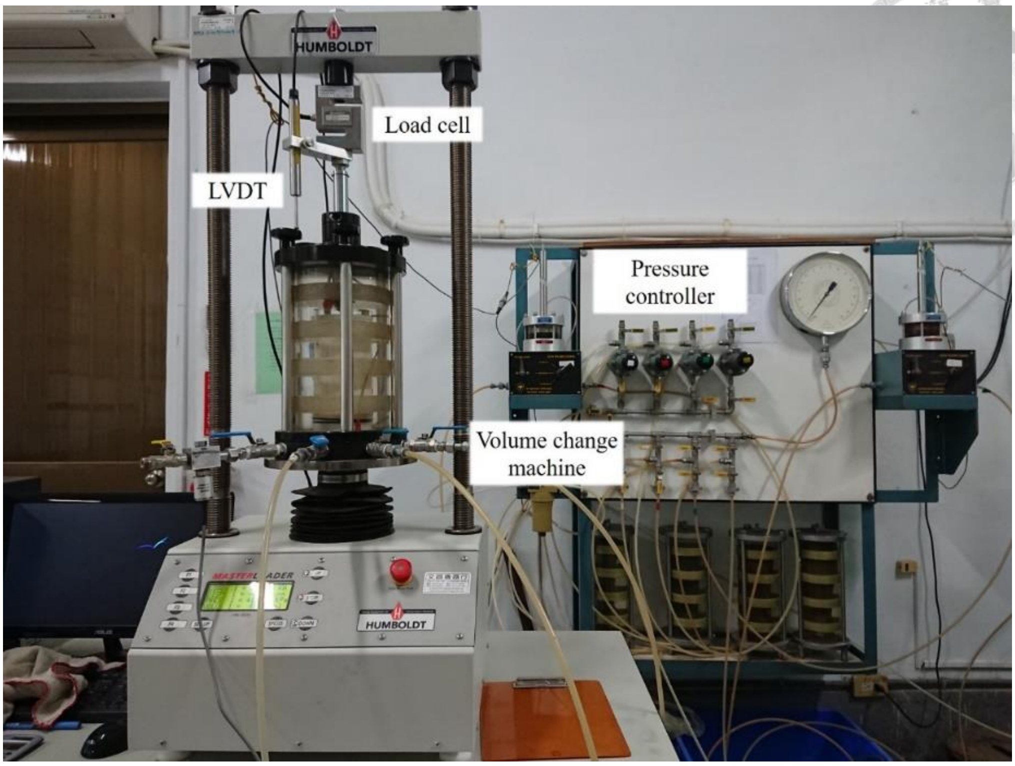

Figure 3.12 Apparatus of the triaxial test

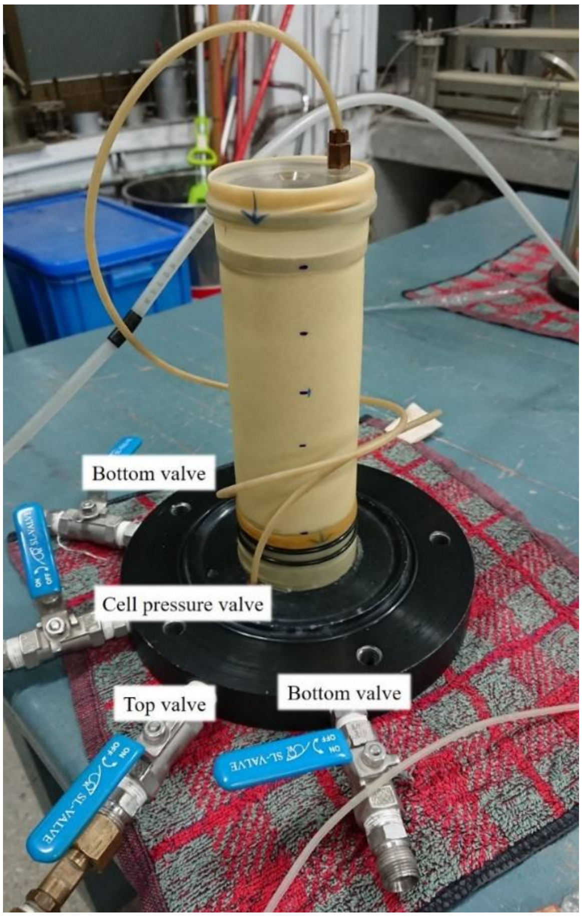

Figure 3.13 Specimen preparation

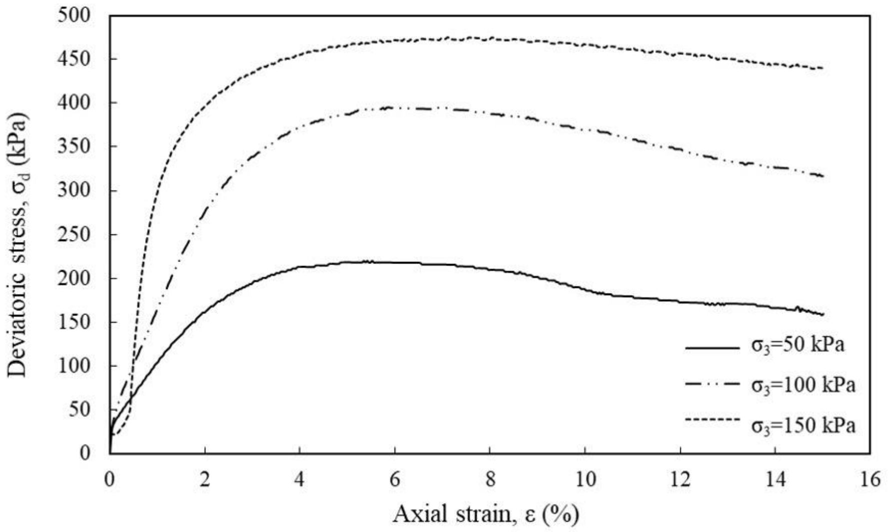

(a) Deviatoric stress versus axial strain

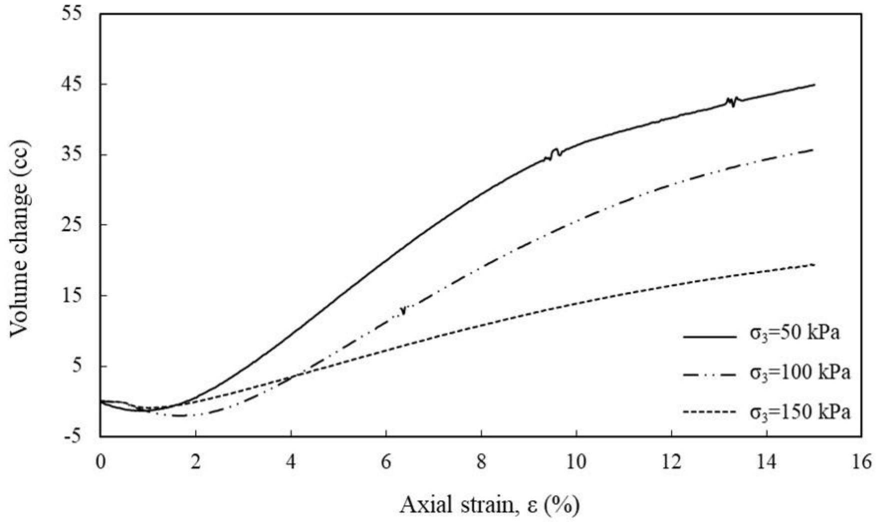

(b) Volume change versus axial strain

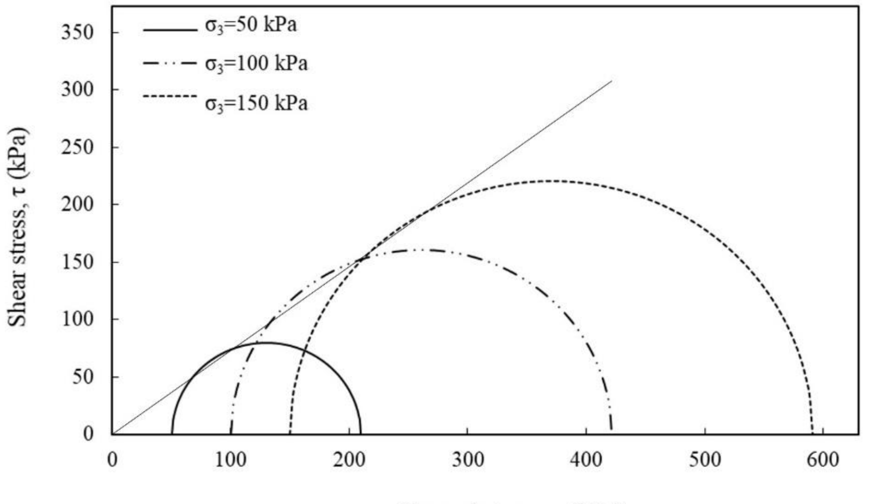

(c) Mohr circles

Figure 3.14 Results of the consolidated drained triaxial tests

doi:10.6342/NTU201901530

3.3.4 Consolidated Undrained Triaxial Test

For testing soil with relatively low permeability (i.e., Vietnam quartz sand with 20% Kaolinite), consolidated undrained triaxial test should be done to evaluate the shearing properties of the testing soil. The testing apparatus and specimen preparation are the same as that used in the consolidated drained triaxial test, as shown in Figure 3.12 and Figure 3.13. What is worth noticing is that during the shearing phase, the valve for drainage remained closed to prevent drainage. Pore water pressure was monitored throughout the test. Mohr circles together with the friction angle of the testing soil can be determined from the tests, and the results are presented in Figure 3.15 and summarized in Table 3.5. The effective cohesion and friction angle of the testing soil is 17.3 kPa and 32.6°, respectively.

Table 3.5 Result of the consolidated undrained triaxial test

Total stress		Effective stress	
Cohesion, *c* (kPa)	Friction angle, ϕ (°)	Cohesion, *c*′ (kPa)	Friction angle, ϕ' (°)
48.7	26.6	17.3	32.6

doi:10.6342/NTU201901530

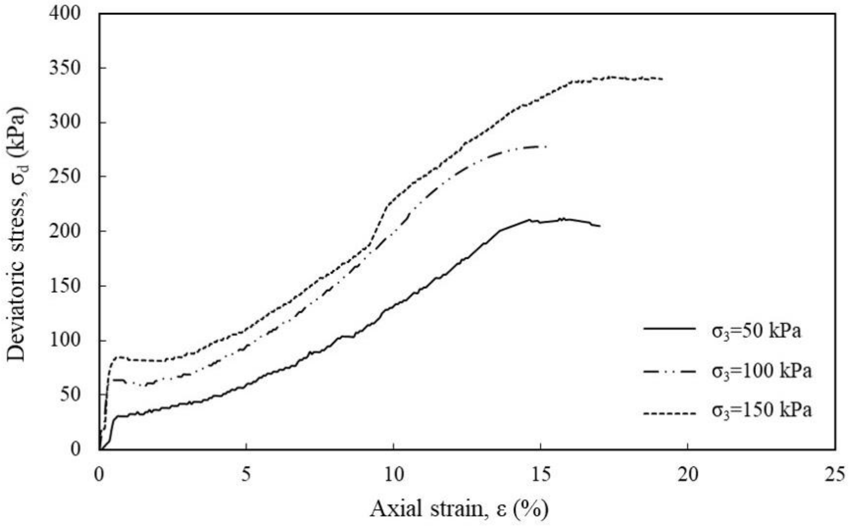

(a) Deviatoric stress versus axial strain

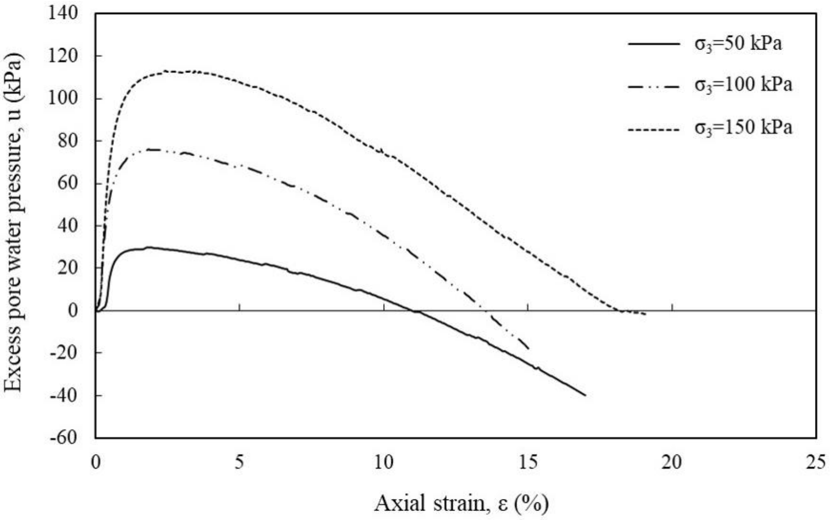

(b) Excess pore water pressure versus axial strain

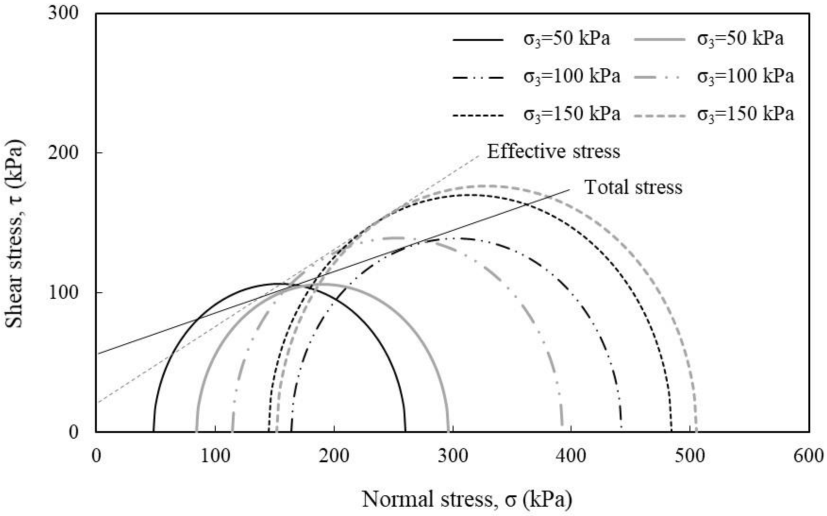

(c) Total and effective stress Mohr circles

Figure 3.15 Results of the consolidated undrained triaxial tests

3.4 Material Properties of Reinforcement

The model test performed in this study had been scaled down to secure a consistent behavior between the model and the prototype. Therefore, the dimensions and the strength of the reinforcement had also been scaled down. Section 2.3 thoroughly introduced the principle of scaling down. Wide width tensile strength tests were carried out to determine the material for reinforcement. A mosquito net is used in this research as the geogrid reinforcement because of its accordance with the requirements of the scaled-down strength. Table 3.6 summarizes the basic properties of the reinforcement. Figure 3.16 shows the picture of the reinforcement and the facing.

Table 3.6 Basic properties of the geogrid reinforcement and geotextile facing

Reinforcement	
Type	Geogrid
Mass per unit area (g/m^2)	13.48
Facing	
Type	Non-woven geotextile
Mass per unit area (g/m^2)	29.60

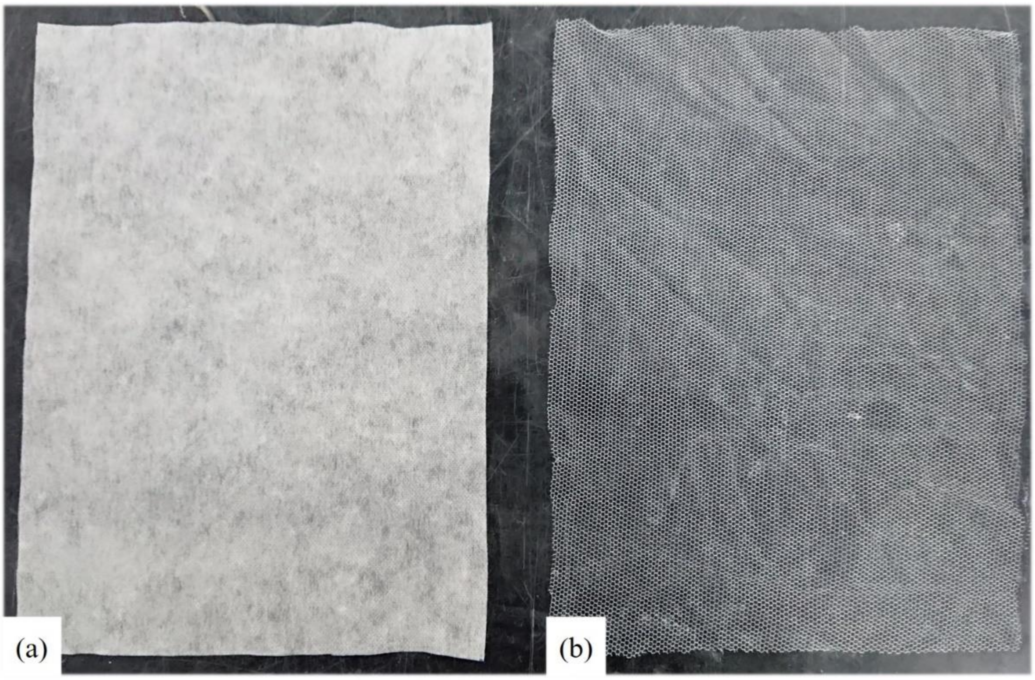

Figure 3.16 Testing materials: (a) Geotextile facing; (b) Geogrid reinforcement

3.4.1 Wide Width Tensile Strength Test

In order to investigate the mechanical properties of the testing material, wide width tensile strength was conducted to get the maximum tensile strength and the allowable strain of the testing material. According to ASTM D4595, the size of the specimen should be at least 200 mm in both length and width, and the pulling rate should be 10±3 %/min. The test was performed in Tamkang University using the universal testing machine from Geotech Testing Machine Incorporation, as shown in Figure 3.17. The specimen is cut to 200×200 mm in length and width. Regarding the clamps, roller clamps and sanders clamp are recommended in the ASTM D4595; sanders clamps were used in the tests. Since the testing material is anisotropic, the test was carried out in both longitudinal and transverse direction. However, based on the test results, only longitudinal direction was used in the model test. Figure 3.18 shows the results of the test in longitudinal direction and Table 3.7 summarizes the test results. The maximum tensile strength of the testing material is 0.5 kN/m and the allowable strain is 6.5 %.

Table 3.7 Test results of the tensile strength test for geogrid along longitudinal direction

	Test 1	Test 2	Test 3	Average
Tensile strength, T_{ult} (kN/m)	0.51	0.48	0.50	**0.50**
Ultimate tensile strain, ε_u (%)	5.5	6.4	7.5	**6.5**
Stiffness at 2% strain, J_2 (kN/m)	6.8	7.5	7.3	**7.2**
Stiffness at 5% strain, J_5 (kN/m)	7.4	8.3	7.6	**7.8**

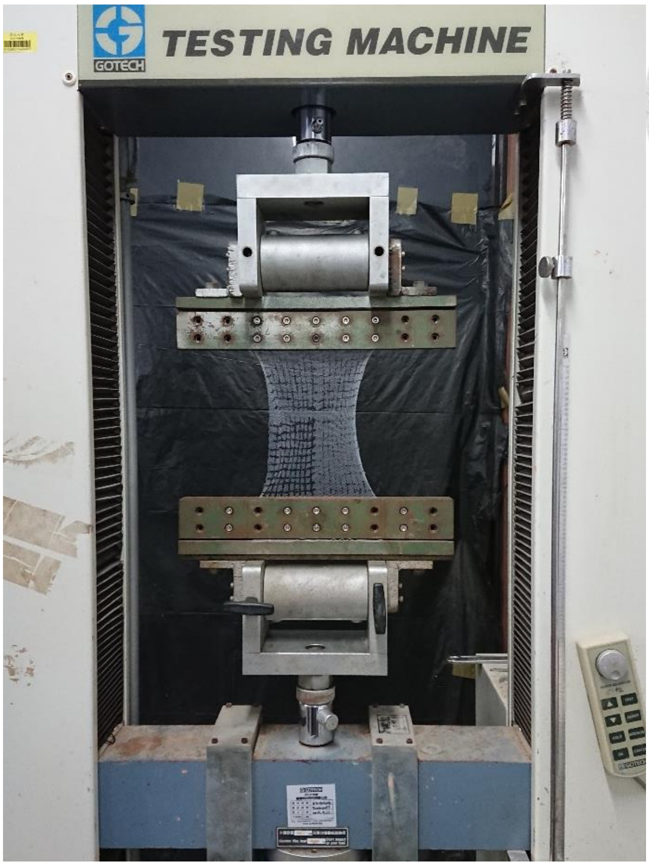

Figure 3.17 Universal testing machine

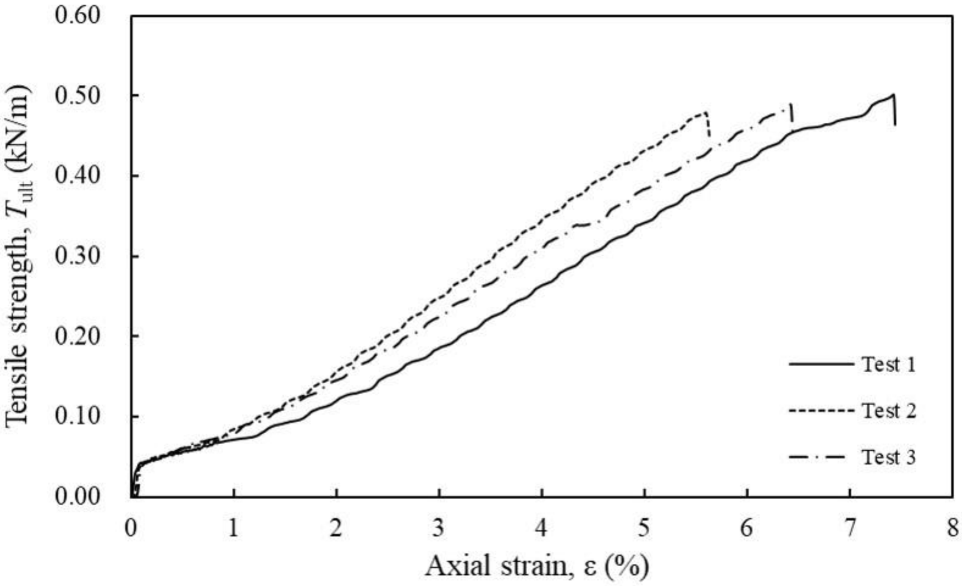

Figure 3.18 Results of the tensile strength test along longitudinal direction

3.4.2 Soil-Geogrid Interface Shearing Strength Test

The overburden pressure along with the surcharge is the antecedent of the existence of the friction between the soil-geogrid interface, as mentioned in Chapter 2. The enhancement of the global stability of GRS walls can be attributed to the increase of the shearing strength, which results from the interaction between the tensile strength of the geogrid and the soil-geogrid friction. Hence, the importance of investigating the shearing properties between soil-geogrid interface cannot be underestimated.

The direct shear apparatus employed in this research was modified from the conventional direct shear apparatus (Tsai, 2011). The lower box was replaced with a steel block, allowing the testing material be fixed on the lower box with screws on the sides, as shown in Figure 3.19. Moreover, sliding was found to occur between the testing material and the steel block if the applied vertical load was too large (Lai, 2018). This will cause the underestimation of the interface friction angle. Hence, the vertical loads of 50, 100, and 150 kPa were applied in this research, for it not only represents the overburden pressure of the model wall in this research but also precisely estimates the interface friction angle. Mohr-Coulomb failure criteria was used to determine the friction angle. The direct shear test was done according to the ASTM D3080. The results of the direct shear tests are summarized in Table 3.8. Efficiency factor E_ϕ was used to understand the difference between the shear strength of soil-soil interface and soil-geogrid interface. The testing material has an efficiency factor of 0.875 and 0.678 in pure sand and silty sand, respectively. The efficiency factor can be calculated from Equation 3.4:

$$E_\phi = \frac{\tan\delta}{\tan\phi} \tag{3.4}$$

where ϕ = friction angle between the soil-soil interface and δ = friction angel between the soil- geogrid interface. The efficiency factor is usually smaller than 1 because during the shearing, the soil particles will fill into the voids of the geogrid and cause a smaller result of the friction angle.

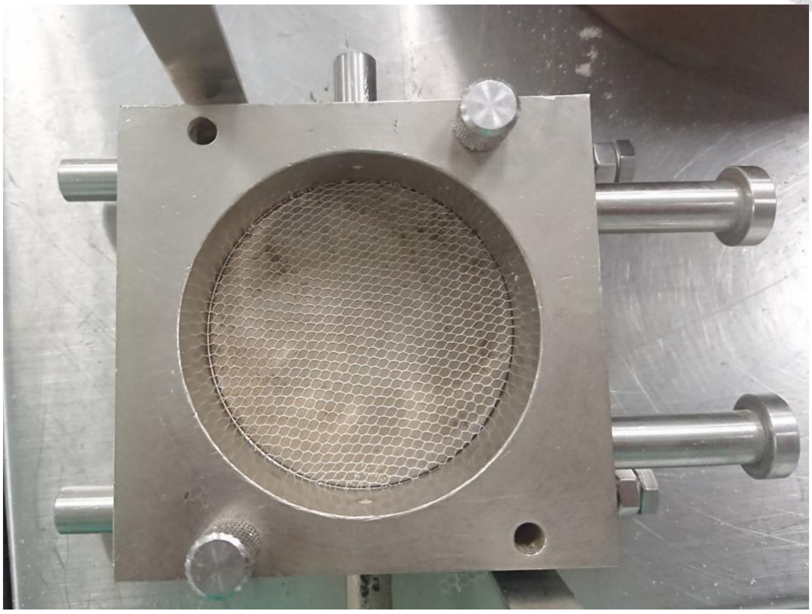

Figure 3.19 Modified direct shear box

Table 3.8 Results of the soil-geogrid interface direct shear test

Vietnam quartz sand	
	E_ϕ
At initial water content	0.88
At saturation	0.86
Silty sand	
	E_ϕ
At initial water content	0.68
At saturation	0.50

Table 3.9 summarizes the properties of the test materials (sand, silty sand, and geogrid).

Table 3.9 Material properties of testing soil and reinforcement

Parameter	Value
Vietnam quartz sand	
Specific gravity, G_s	2.65
USCS classification	SP
Cohesion, c (kPa)	0
Friction angle, ϕ (°)	37
Target unit weight, γ_d (kN/m^3)	14.7
Silty sand	
Specific gravity, G_s	2.62
USCS classification	SM
Effective cohesion, c' (kPa)	17
Effective stress friction angle, ϕ' (°)	32
Total cohesion, c (kPa)	49
Total stress friction angle, ϕ (°)	27
Target unit weight, γ_d (kN/m^3)	16.3
Optimum water content, ω (%)	10.7
Reinforcement	
Mass per unit area (g/m^2)	13.48
Maximum tensile strength, $T_{\max}$ (kN/m)	0.5
Ultimate tensile strain, ε_u (%)	6.5
Sand-geogrid interface friction angle, δ_{SP} (°)	27.1
Efficiency factor between geogrid and sand, $E_{\phi,SP}$	0.875
Silty sand-geogrid interface friction angle, δ_{SM} (°)	17.3
Efficiency factor between geogrid and silty sand, $E_{\phi,SM}$	0.678

Chapter 4 Model Tests and Test Program

In this study, a series of reduced scale model tests was conducted to investigate the performance of GRS walls under rainfall conditions. Different backfill materials and different reinforcement layouts were adopted to evaluate different failure mechanisms. Improved measure using sand cushions was also evaluated. The model wall, model preparation, test procedure, instrumentation, and the digital image analysis are thoroughly introduced in this chapter.

4.1 Model test

4.1.1 Wall model

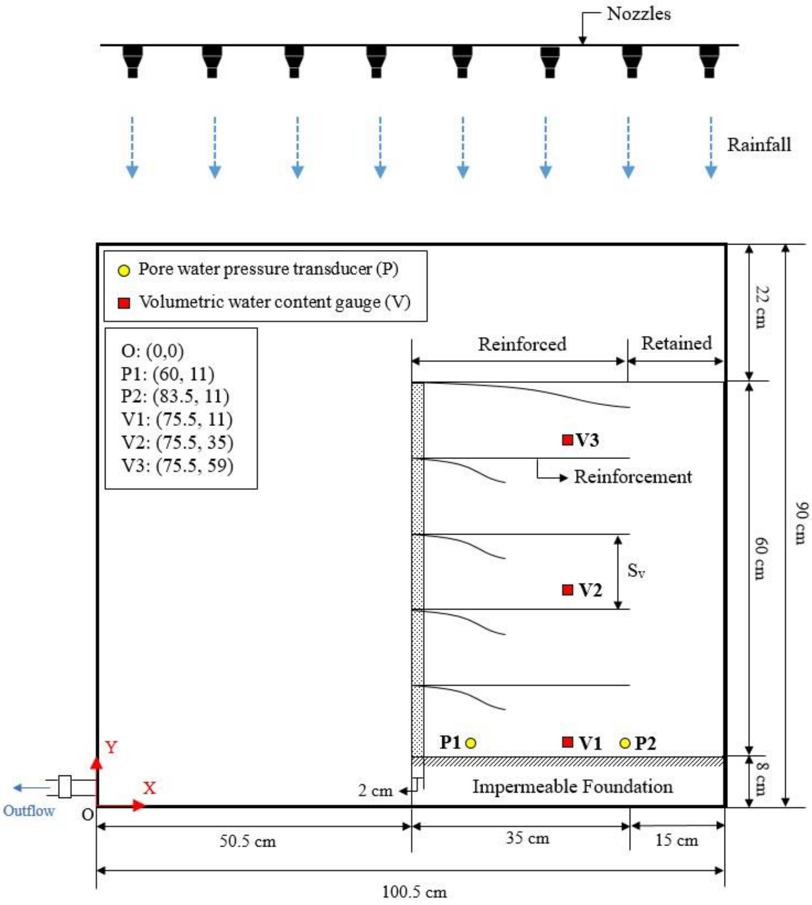

Figure 4.1 Schematic view of the sandbox and the locations of the sensors

The sandbox used in this research has the dimensions of 100 cm, 30 cm, and 90 cm in length, width, and height, respectively. A Plexiglas window is mounted in the front of the sandbox for visual observation during the tests. Four wheels on the steel frame allows the sandbox be moved to or fixed at the designated location. The backside of the sandbox consists of three steel plates. The top one can be removed for the construction of the wall models. Various holes were chiseled on the steel plates for the installation of the measuring devices: two pore water pressure transducers and three volumetric water content gauges were installed to monitor the hydraulic performance during the tests. The details of the measuring apparatus are discussed later in Section 4.2. Figure 4.1 illustrates the schematic view of the sand box and the locations of the sensors, and Figure 4.2 shows a panorama of the experiment.

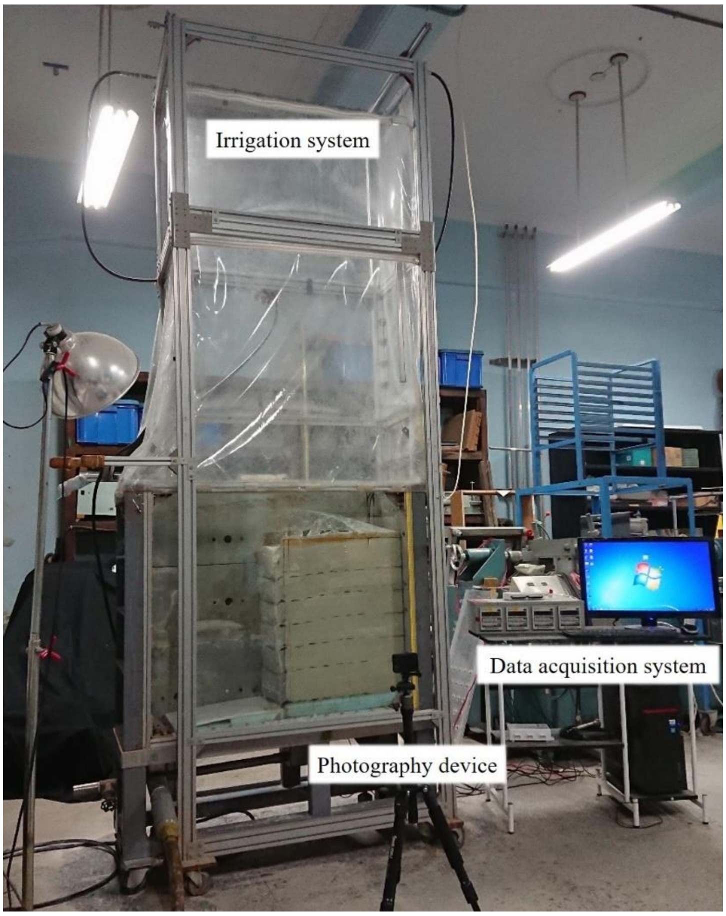

Figure 4.2 Panorama of the experiment

doi:10.6342/NTU201901530

The model GRS wall was designed with a scaling factor *N* equals to 10 based on the reduced scale designation which was elaborated in Section 2.3. Table 4.1 provides the parameters in this research and its corresponding value in the prototype. A GRS wall with dimensions of 50 cm, 30 cm, and 60cm in length, width, and height, respectively, was constructed in the sandbox. The reinforced zone is 35 cm while the retained zone is 15 cm. An 8 cm-thick foam board was sealed at the bottom of the sandbox to serve as an impermeable foundation to simulate the RC slab usually used in the field to increase the bearing capacity. Notably, sandpaper was stuck to the foundation to increase the friction between the GRS wall model and the foundation. The Styrofoam foundation was sealed to the sandbox with silicon to prevent soil particles and water leaking into the foundation.

Table 4.1 Reduced-scale model parameters

Scaling factor *N* = 10				
	Parameters	Scaling factor	Model	Prototype
	Geometry			
	Wall height, *H* (m)	1/*N*	0.6	6
	Wall length, *H* (m)	1/*N*	0.5	5
Sand	**Rainfall parameters**			
	Intensity, *I* (mm/hr)	1	135	135
	Duration, *t* (hrs)	1/*N*	5	50
Silty sand	**Rainfall parameters**			
	Intensity, *I* (mm/hr)	1	75	75
	Duration, *t* (hrs)	1/*N*	18	180

An irrigation system hanging over the sandbox was used to simulate rainfall. The tube at the left side of the sandbox served as the outlet of the rainfall and surface runoff. The irrigation system consists of two series of nozzles, 8 nozzles on each series was hung 160 cm above the sandbox to simulate rainfall conditions. The picture of the irrigation system is presented in Figure 4.3 (a). A pressurized motor connected to a faucet was used to pump the water up to the nozzles (Figure 4.3 (b)). The rainfall sprayed out from the nozzles was smaller than 0.1 mm. The fine sprays were ensured to achieve the terminal velocity upon falling on the GRS wall and do not erode the crest.

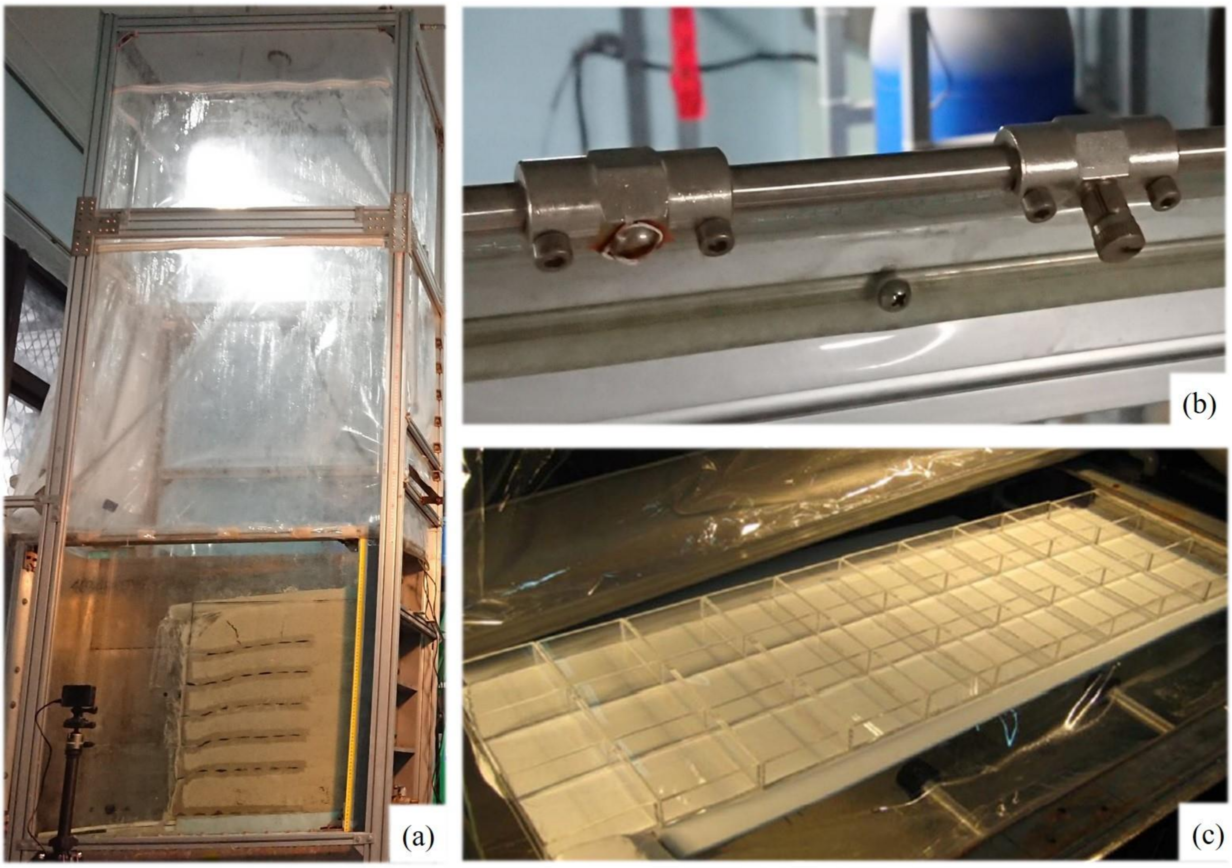

Figure 4.3 (a) Irrigation system; (b) Nozzles; (c) Transparent boxes

doi:10.6342/NTU201901530

Both rainfall intensity and uniformity was ensured before the experiments. 30 transparent boxes (Figure 4.3 (c)) having the dimensions of 10 cm, 10 cm, and 3 cm in length, width, and height, respectively was placed inside the sandbox to collect water, for the purpose of determining the rainfall intensity and uniformity. Regarding the rainfall intensity, the intensity can be calculated from Equation 4.1 given by Technical Regulations for Soil and Water Conservation:

$$I = 600 \frac{Q}{At} \tag{4.1}$$

where I = intensity of the rainfall, (mm/hr), Q = accumulated volume of rainfall in the testing period, (cm^3), A = area that collects rainfall, (cm^2), and t = time (min). The rainfall intensity can be controlled by either adjusting the nozzles or the faucet. The irrigation system can achieve a maximum intensity of 135 mm/hr; lower intensities can be reached by closing part of the nozzles and decreasing the pressure of the pump. The uniformity of the rainfall is determined by Equation 4.2:

$$U_c = 1 - \frac{\sum |X_i - X_m|}{\sum X_i} \tag{4.2}$$

where U_c = uniformity of the rainfall, X_i = rainfall collected in the i^{th} box, and X_m = average value measured from all the boxes. The uniformity of the rainfall (Table 4.2) was within the range of 82% to 92%, which is considered reasonable compared to preceding studies.

Table 4.2 Rainfall uniformity in preceding studies

	Uniformity (%)
Meyer and McCune, (1958)	88
Shelton et al., (1958)	66~84
Fan and Lovell, (1987)	88
Chang, (2009)	80
Chien, (2010)	82
Chen, (2012)	78~93
This study	**82~92**

Filter layer is often adopted in GRS walls with marginal backfill to enhance drainage and prevent erosion. The thickness of the filter layer has no particular specifications; nevertheless, the filter layer cannot be too thick because the pore water pressure would then be dissipated too fast, subverting the intention of investigating the performance of a GRS wall with marginal backfill. A 2 cm-thick filter layer was adopted in this research.

Figure 4.4 is a schematic view of the relationship between the filter and the protected soil. The design of the filter layer should satisfy the two criteria proposed by Terzaghi and Peck (1948). First, the grain size of the smaller particles of the filter material should be smaller than the grain size of the larger particles of the backfill material to prevent internal erosion of the soil and piping, which is referred to as the retention criteria. Second, the grain size of the filter material should be larger than that of the backfill material to ensure the permeability of the filter is large enough to prevent pore water pressure accumulating in the GRS wall. The above-mentioned two criteria can be expressed in Equation 4.4 and 4.5:

$$\frac{D_{15(F)}}{D_{85(S)}} \leq 4-5 \tag{4.3}$$

$$\frac{D_{15(F)}}{D_{15(S)}} \geq 4-5 \tag{4.4}$$

where subscript F denotes the grain size of the filter layer and subscript S represents the grain size of the backfill soil. The design of the filter layer in this research is shown in Figure 4.5.

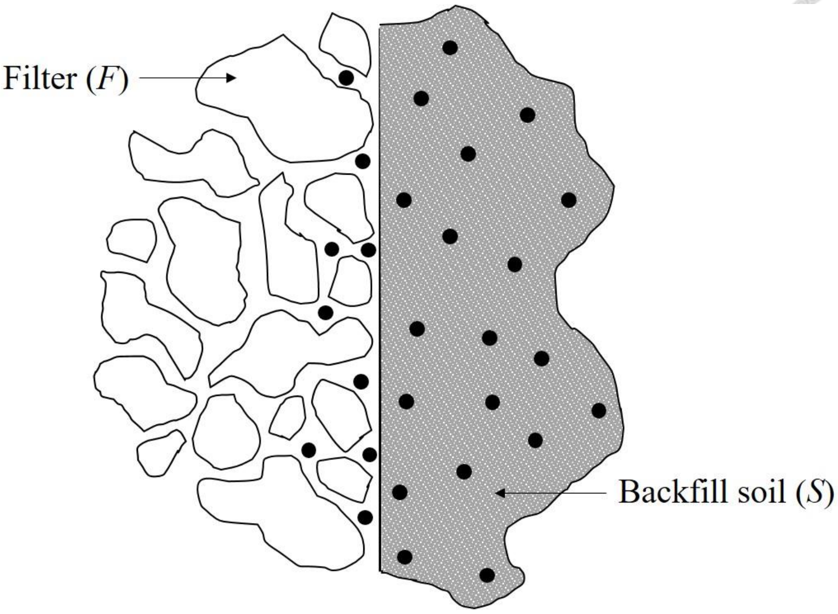

Figure 4.4 Schematic view of the function of filter layer

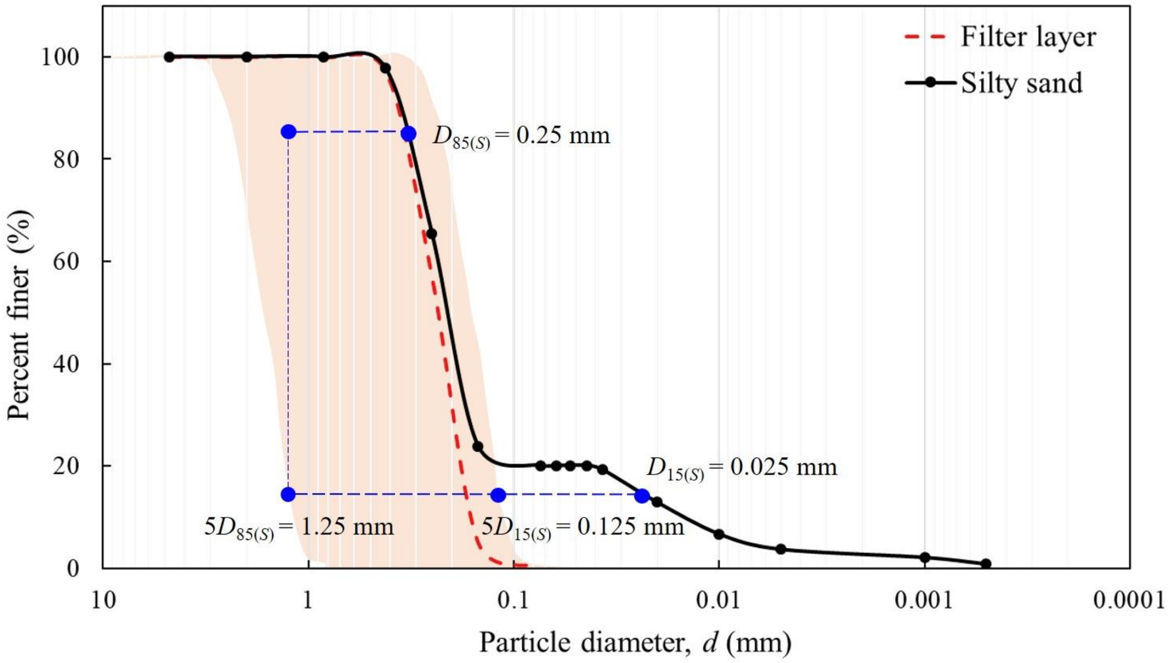

Figure 4.5 Design of the filter layer

4.1.2 Model Preparation

The wall was constructed layer by layer by compacting the soil to the designated height. A reinforcement spacing of 9 cm was used while a larger spacing (S_v = 12 cm) was used as a control group and a smaller spacing (S_v = 6 cm) was used as one of the improved methods. The amount of soil needed per layer is calculated by Equation 4.3, the weight-volume relationship:

$$W = V \times \frac{1}{(1+e)} G_s \times \gamma_w \tag{4.5}$$

where W = weight of the soil needed per layer, V = volume per layer, e = void ratio of the soil, and G_s = specific gravity of the soil.

In this study, the model GRS walls were compacted to 90% of the maximum dry density at optimum water content (ω = 10.7%). Regarding wall models with granular soil for improved methods, the friction angle and the permeability of the soil barely varies with the increase of relative density if the relative density is larger than 60% according to Fong (2010). Thus, the model GRS walls with granular backfill in this study were compacted to 70% relative density. In addition, an initial water content is needed to develop apparent adhesion for the soil to remain stable. It was recommended that an initial water content of 5-10% be used in model GRS walls with granular backfill. However, an initial water content of 10% would make it hard to observe the progression of the wetting front. Hence, 5% initial water content is used in this research for easy investigation of the wetting front while maintaining the initial wall stability.

Blue Styrofoam boards were used as the formwork during the construction of the specimen, as shown in Figure 4.6. The Styrofoam boards were cut according to the designated length, width, and height and were piled up along with the construction of the specimen layer by layer. Moreover, interface treatment to reduce the effect of boundary friction is adopted according Liu et al., (2014), in which they suggested that lubricant sandwiched between PE sheets can reduce up to 67% of the boundary friction. Thus, water-based lubricant sandwiched between two PE sheets were applied to both side of the sand box to reduce the effect of boundary friction in this research. Thorough description of the procedure is enunciated subsequently.

doi:10.6342/NTU201901530

Figure 4.6 Blue Styrofoam mold used for construction

Figure 4.7 presents the picture of the tools used for construction. First, the sandbox was cleaned by a brush. The perforated holes for the pore water pressure transducer were also brushed. The water-based lubricant sandwiched between two PE sheets were applied subsequently. Notably, holes were cut in the PE sheets at the location of the sensors in order to allow contact between the sensors and the specimen. Several 3 cm-thick Styrofoam was put into the sandbox as the mold of the first layer, depended on the spacing (i.e., S_v = 6 cm, 9 cm, or 12 cm). A geogrid was then placed at the bottom of the first layer. Furthermore, black colored coarse sand was applied near the surface with an angle sleeker using an acrylic mold with dimensions of 30 cm in length, 0.5 cm in width, and 0.5 cm in height, forming a dashed line with 2.5 cm spacing. The dashed line formed by colored sand was used to observe soil deformation and to analyze the reinforcement strain. Displacement would be found in the dashed lines when the reinforcement was under tension. Specifically, the grain size of the colored sand is slightly larger than the backfill materials, making it easier to separate them by sieving after the experiment.

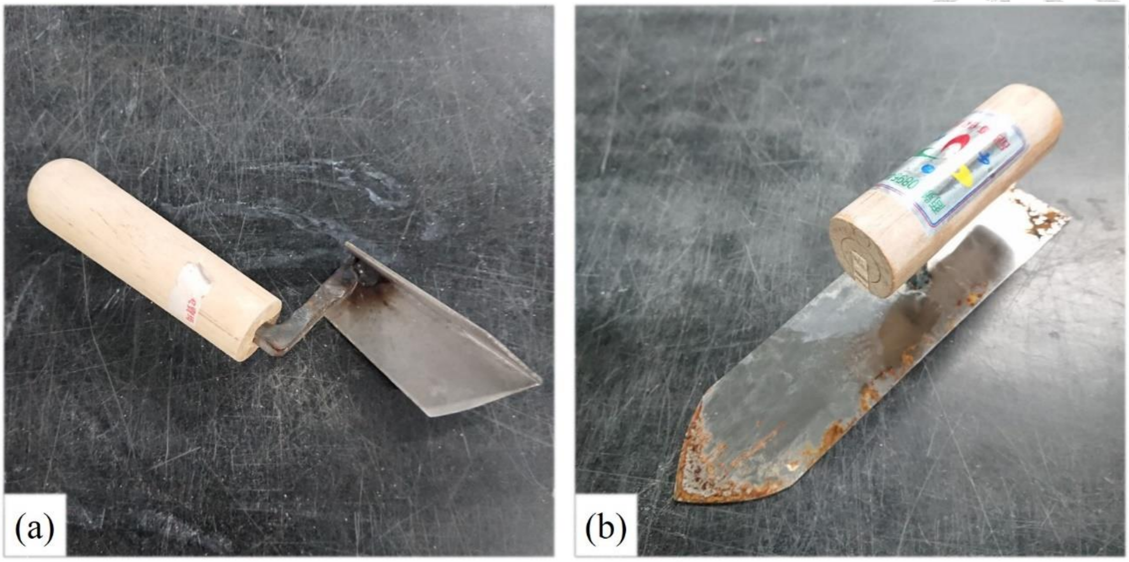

Figure 4.7 Tools used for construction: (a) Angle sleeker; (b) Concrete trowel

Figure 4.8 (a) Hammer; (b) Filter layer; (c) Scarifying between layers

Afterwards, the construction of the first layer started by compacting the backfill soil with a hammer with a diameter of 15 cm, as shown in Figure 4.8 (a). The backfill soil was uniformly mixed in a large bowl in advance. However, a 2 cm thickness near the wall face was blocked by Styrofoam boards. After compaction of each layer, the two Styrofoam boards were removed and Quartz sand was used as the facing filter layer to prevent the erosion of fines contents in the backfill during rainfall. This approach is also to model the sandbags typically adopted as the facing elements in practical design of wrapped-around GRS walls. The facing filter layer was also uniformly mixed in advance with a 5% initial water content, allowing the apparent adhesion to develop. Once the filter layer was constructed, the geogrid was wrapped around into the backfill layer, as shown in Figure 4.8 (b). Notably, a pre-tension was given to the geogrid to ensure the mobilization of the tensile strength upon the start of the test. In addition, the surface and facing of the layer is trimmed with a concrete trowel. Next, the specimen was scarified between each layer to increase the friction between two compacted soil interface, which is critical to the progression of the failure surface. Figure 4.8 (c) shows the scarifying between the layers. The construction procedure was repeated until reaching the design wall height. A picture of the model GRS wall is shown in Figure 4.9.

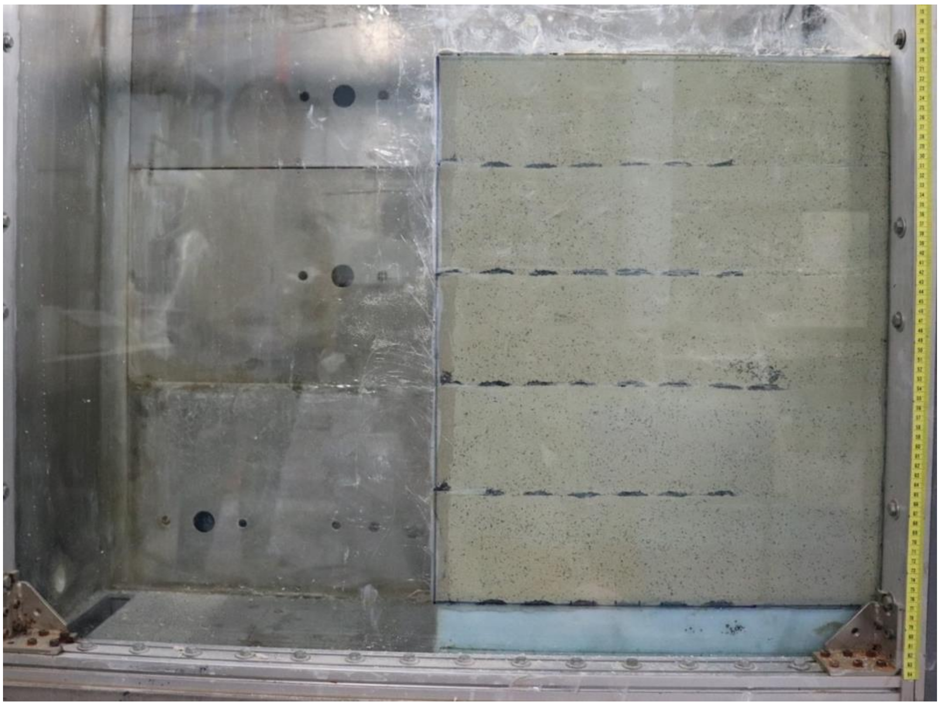

Figure 4.9 Model GRS wall after construction

doi:10.6342/NTU201901530

4.1.3 Improved design measure

Three improved design measures were proposed in this study, namely, reduction of the reinforcement spacing, selection of a better quality backfill, and the adoption of sand cushions. The inclusion of sand cushions can enhance the stability of the GRS walls with marginal backfill. It is often applied to accelerate pore water pressure dissipation and reduce the surficial intrusion and long-term clogging in the nonwoven geotextiles by fine-grained soil. Moreover, sand cushions provide drainage to the GRS wall since the permeability of the sand is larger than that of the marginal backfill. Additionally, the strength and the deformation characteristics were improved because the efficiency factor at the interface between the geogrid and the sand is much larger than that at the interface between the geogrid and the marginal backfill. According to Yang et al. (2018), replacing around 20% of the marginal backfill with sand is the optimization. Thus, in this research, the geogrid was sandwiched between two layers of 2 cm-thick sand cushions, as shown in Figure 4.10.

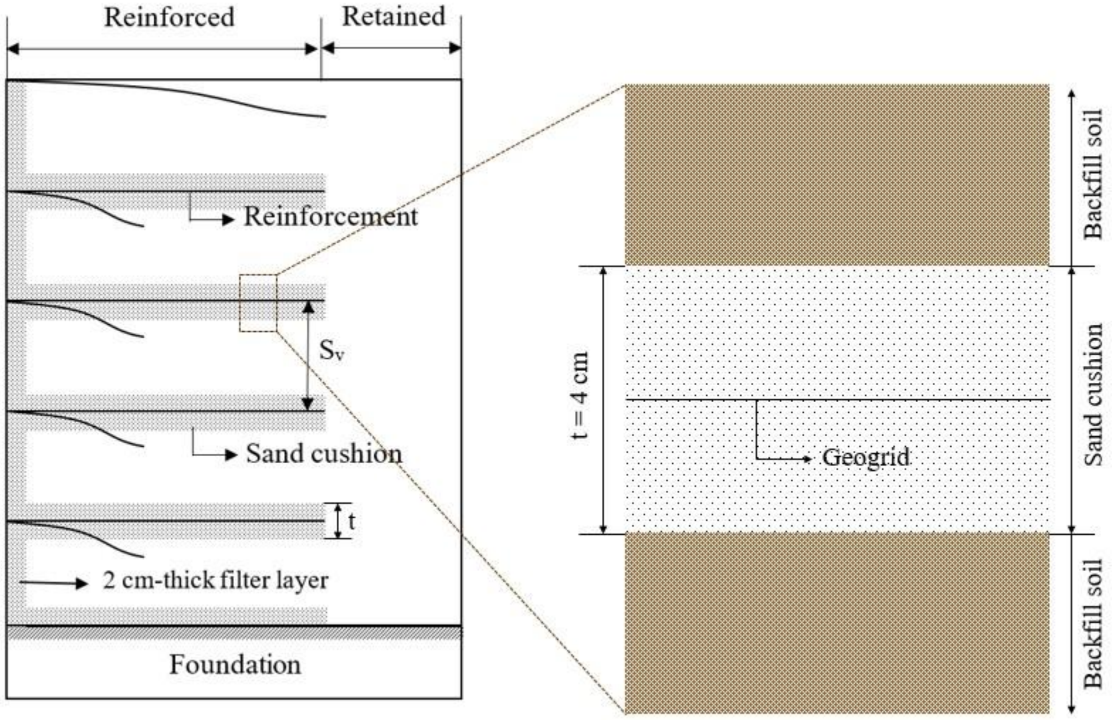

Figure 4.10 Design of sand cushion

doi:10.6342/NTU201901530

4.2 Instrumentation

4.2.1 Specifications of the Measuring Devices

Two pore water pressure transducers and three volumetric water content gauges were used in this research. The pore water pressure transducers were installed at 3 cm from the bottom of the model GRS wall; one was placed near the toe and the other was located near the bottom in order to measure the pore water pressure near the toe and investigate the change of pore water pressure with the progression of the failure. The three volumetric water content gauges were situated at the middle of the wall from the top, middle, to the bottom, for the investigation of the wetting front propagation.

The pore water transducers used in this study were manufactured by KYOWA Electronic Co. Ltd. (Model PGM-02KG). The transducers were considered as highly accurate and stable measurement with a rated output of 0.75 mV/V, a capacity of 0~20 kPa, and an error of less than 0.3%. The signals measured by the transducers were magnified by an amplifier manufactured by KYOWA Electronic Co. Ltd. (Model WGA-670A) and transmit to the data logger manufactured by National Instruments Corp. (Model NI USB-6218). The signals were eventually transmitted to the computer through the LabView 8.6 software. Figure 4.11 presents the pictures of the devices for measuring pore water pressure. Figure 4.12 shows the schematic view of the measuring system.

The amplifier (WGA-670A) used in this research aims to intensify the output power of the signal. The amplifier is able to output a signal that has the same waveform as the input signal but with a lager amplitude. Table 4.3 summarizes the specifications of the amplifier.

doi:10.6342/NTU201901530

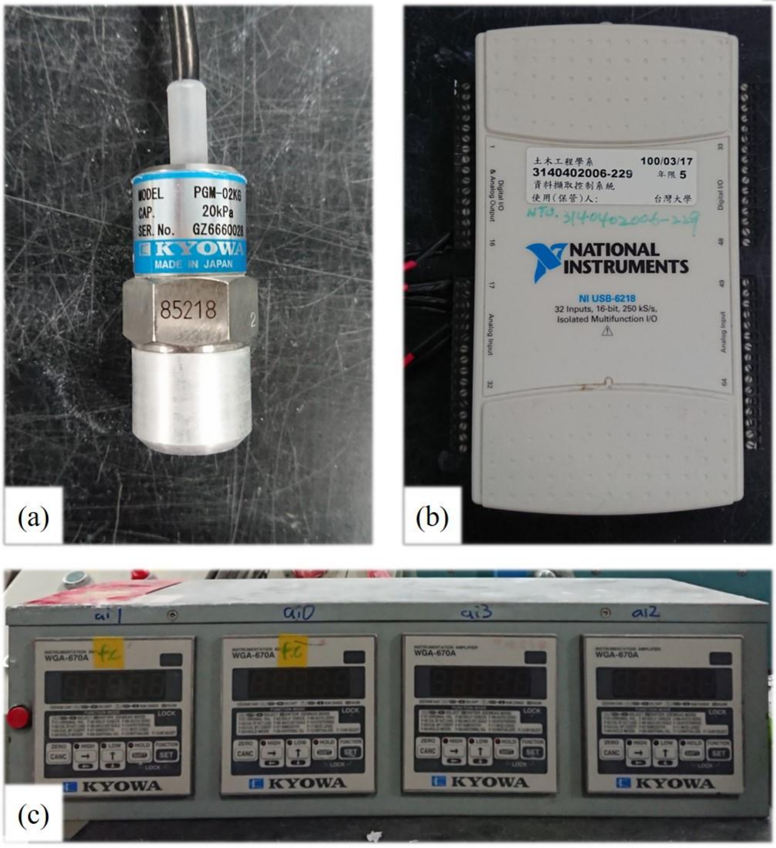

Figure 4.11 (a) Pore water pressure transducer; (b) Data logger; (c) Signal amplifier

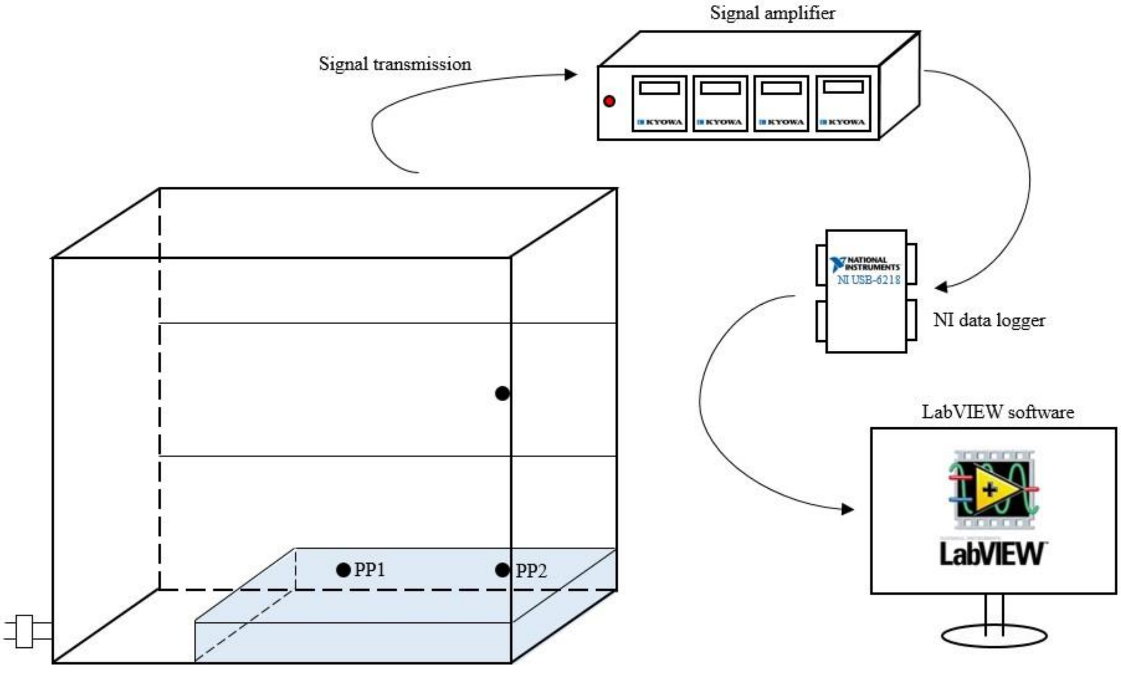

Figure 4.12 Schematic view of the data acquisition system

Table 4.3 Specifications of WGA-670A amplifier

WGA-670A Amplifier	
Number of measuring channels	1
Applicable bridge resistance	87.5 Ω to 10 Ω
Measuring range	±3.2 mV/V
Analog output (D/A outpout)	±10 V
Output speed	500 times/sec
Power supply	100 to 240 VAC
Nonlinearity	±(0.03% FS+1 digit)

Table 4.4 Specifications of USB-6218 data logger

Analog Input	
Number of channels	16 differential or 32 single ended
Sample rate	250 kS/s
Input coupling	DC
Input range	±0.2 V, ±1 V, ±5 V, ±10 V
Maximum working voltage for analog	±10.4 V of AI GND
Analog output	
Number of channels	2
Output range	±10 V
Output coupling	DC
Output impedance	0.2 Ω
Output current drive	±2 mA

Regarding the data logger (USB-6218), 32 different signals can be recorded simultaneously. The data were then recorded in the computer through a data acquisition software, LabView 8.6. Table 4.4 summarizes the specifications of the data logger.

Figure 4.13 demonstrates the system for the measuring of the volumetric water content, which contains three volumetric water content gauges manufactured by Decagon Devices (Model EC-5) and a corresponding data logger (Model EM50). The sensor determines volumetric water content by measuring the dielectric constant of the media using capacitance/frequency domain technology. Its 70 MHz frequency minimizes salinity and textural effects, making the sensor accurate in almost any soil or soilless media. The sensor can measure the volumetric water content between the range of 0% to 100% with and error less than 0.03 m^3/m^3. The data logger has five channels which can be connected to five volumetric water content gauges simultaneously. The data logger can store up to a maximum of 36,000 records. Further considering the test period is long, it was set to record a value every minute to precisely investigate the change of volumetric water content in the specimen throughout the test.

Figure 4.13 (a) Volumetric water content gauge (b) EM 50 data logger

4.2.2 Calibration of the Measuring Devices

The purpose of calibration is to determine the error between the measured value and the true value. The measured value is well affected by the uncertain factors such as temperature, pressure, and personal factors. Hence, calibration is mandatory before conducting experiments to minimize the error of the measurements.

Figure 4.14 presents the calibration device used to calibrate the pore water pressure and its amplifier in this research the portable pressure calibrator model DPI 601. The calibrator was a microprocessor-based instrument with a pneumatic hand-pump and can measure pressure within the range of 0-20 kgf/cm^2, 0-290 psi, or 0-20000 cmH$_2$O. In addition, either pressure, voltage, or current can be displayed by the pressure calibrator.

doi:10.6342/NTU201901530

Figure 4.14 DPI 601 portable pressure calibrator

First, the pore water pressure transducer was attached to the calibrator through a specially made adaptor to calibrate the rated output of the amplifier by fine tuning the calibration coefficient given by the original equipment manufacturer. Once the modified coefficient is correct, the value displayed by the amplifier should equal to the pressure given to the pneumatic hand-pump. Since the pore water pressure transducers used in this research have a capacity of 0-20 kPa, the calibrator was set to the range of 0-20 kgf/cm^2. Notably, the pressure given to the pneumatic hand-pump cannot exceed 20 kPa. Next, the calibrated amplifier was connected to the computer through the data acquisition system (Model NI USB-6218). The software Labview 8.6 was used to acquire data from the data logger into the computer. Furthermore, the built-in calibrating equation in LabView should be set as X=Y, meaning that the value displayed by LabView equals to the pressure given to the pneumatic hand-pump. The relationship between the measured value and the true value can therefore be obtained. Figure 4.15 and Figure 4.16 presents the calibration curves of the two pore water pressures. According to the figures, the linearity of both pore water pressure transducers are considered satisfactory.

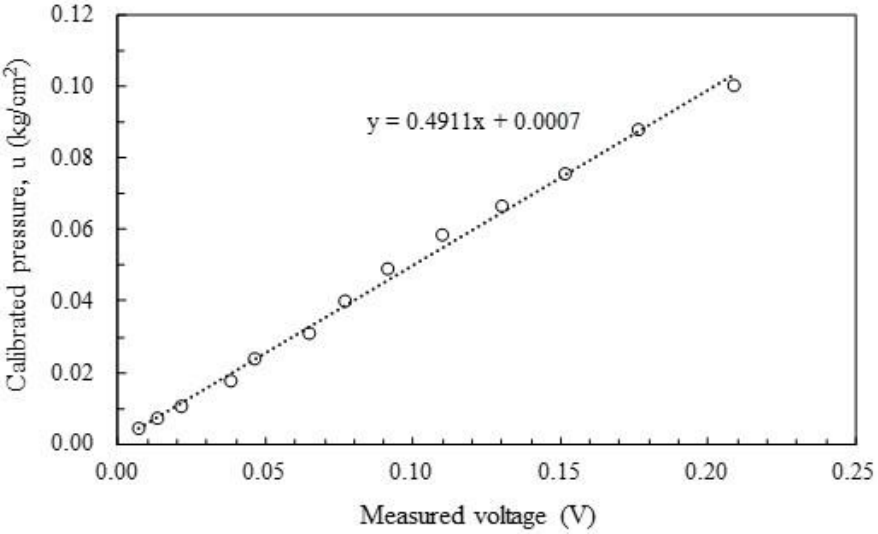

Figure 4.15 Calibration curve of pore water pressure transducer 1

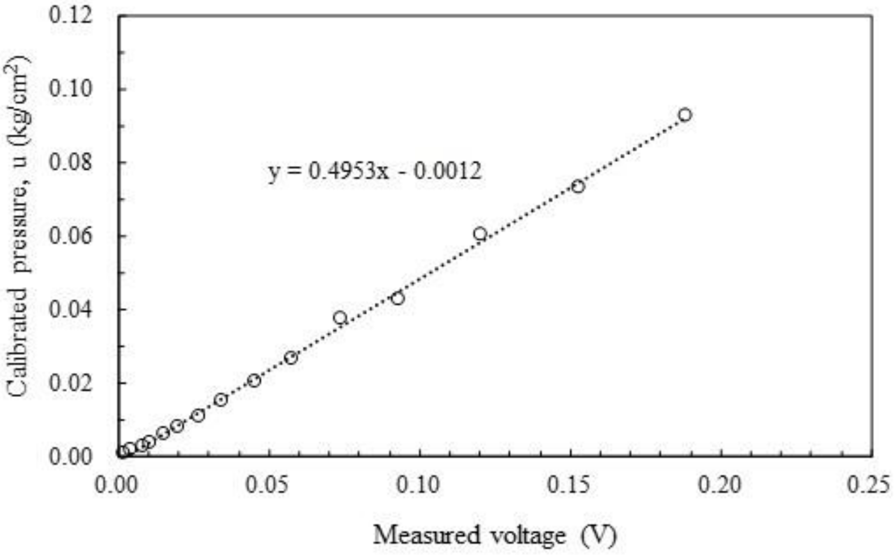

Figure 4.16 Calibration curve of pore water pressure transducer 2

doi:10.6342/NTU201901530

The volumetric water content gauges (Model EC-5) were originally calibrated using an in-situ soil in the United States. However, the backfill used in this research are Vietnam quartz sand and Kaolinite, which are different from that used to calibrate. Thus, samples with different gravimetric water content were prepared to calibrate the volumetric water content gauges. The corresponding volumetric water content of each sample can be calculated by Equation 4.6:

$$\theta = \frac{\omega \times \rho_{soil}}{\rho_{water}} \tag{4.6}$$

where θ = volumetric water content of the sample, ω = gravimetric water content of the sample, ρ_{water} = density of the water, and ρ_{soil} = density of the sample. The volumetric water content gauges were then put into each sample to obtain the measured volumetric water content. The calibration curves can be obtained by plotting the measured volumetric water content versus the actual volumetric water content, as shown in Figure 4.17 and Figure 4.18.

doi:10.6342/NTU201901530

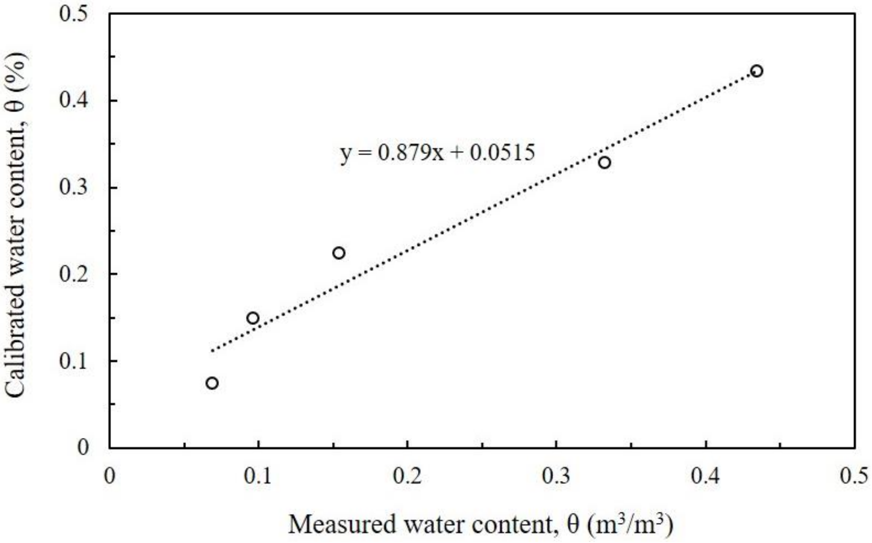

(a) VWC 1

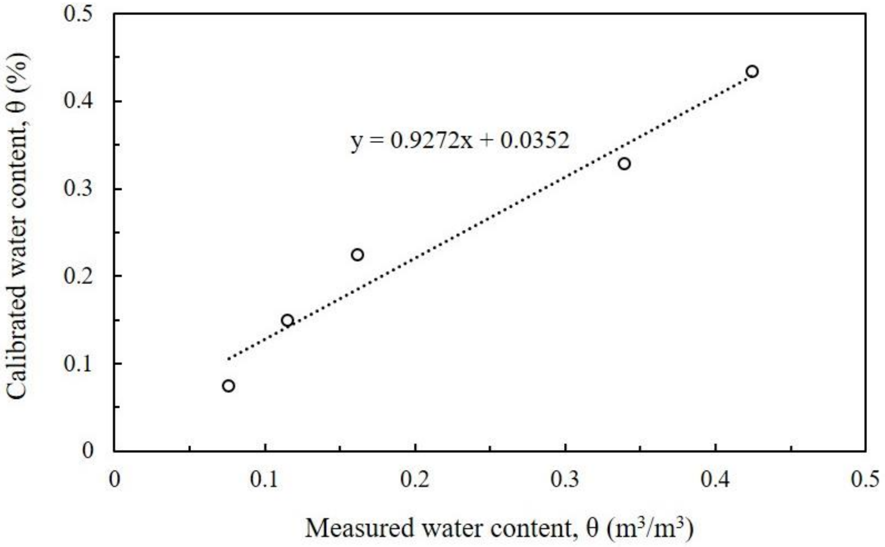

(b) VWC 2

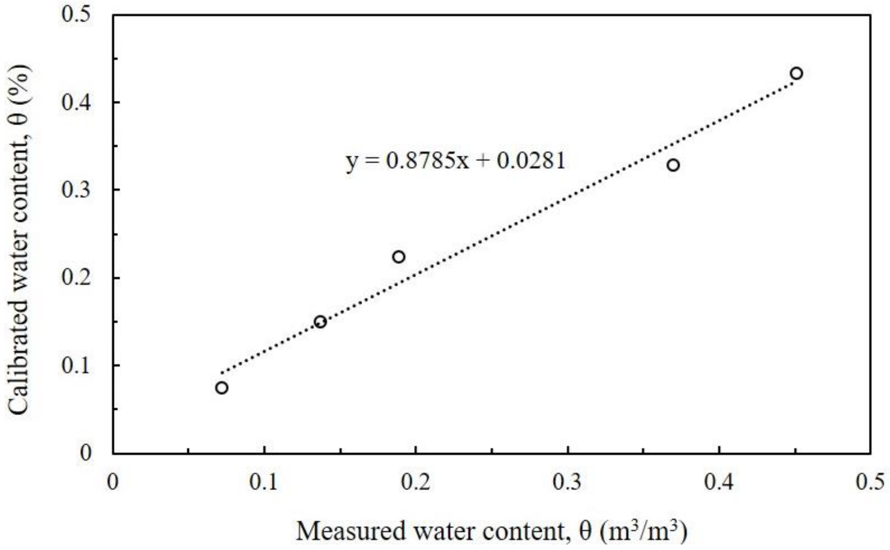

(c) VWC 3

Figure 4.17 Calibration curves of VWC gauges for pure sand

doi:10.6342/NTU201901530

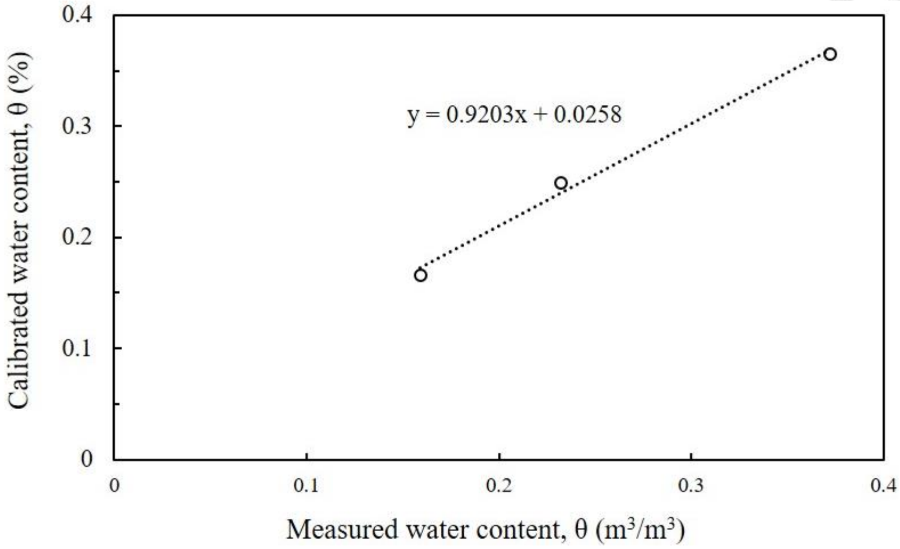

(a) VWC 1

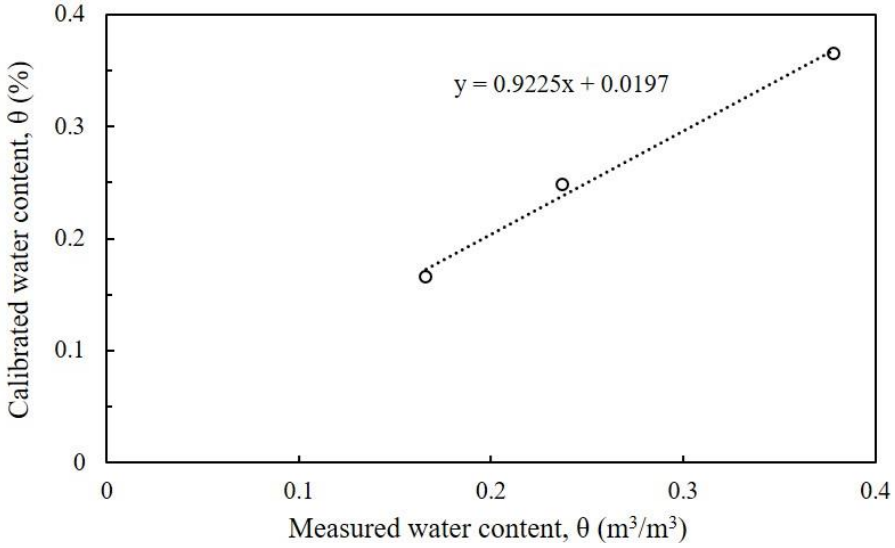

(b) VWC 2

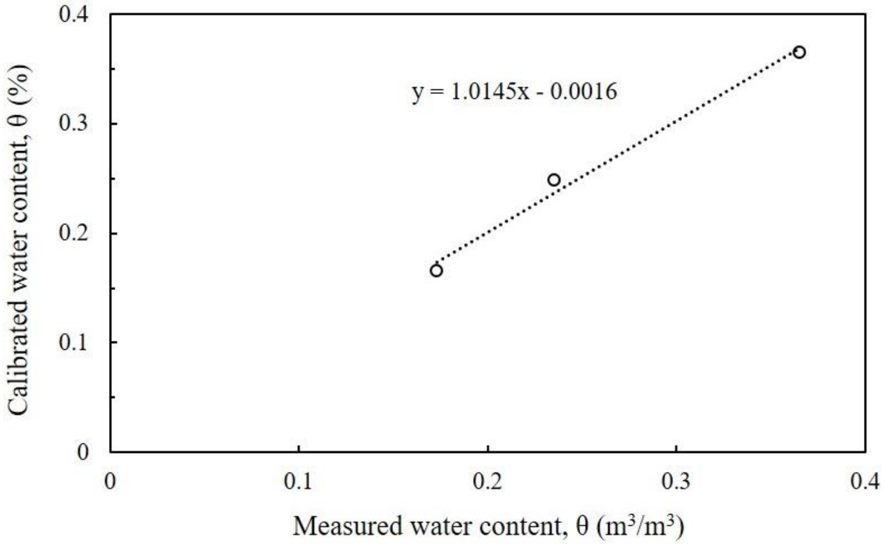

(c) VWC 3

Figure 4.18 Calibration curves of VWC gauges for silty sand

doi:10.6342/NTU201901530

4.2.3 Photography Equipment

Figure 4.19 shows the photography equipment used in this research, Canon EOS 800D and GoPro 4. The digital single-lens reflex camera has greater sensitivity and has more capability of resolution. Moreover, shutter speed, ISO sensitivity, aperture, and focal distance can be adjusted manually to procure the ideal photo. Thus, Canon EOS 800D was used to take pictures of the wall model before and after the tests. GoPro 4 was used to record the experiment because it is waterproof and has excellent 4K image quality, which is favorable for subsequent investigation and post image analysis. More importantly, GoPro has the capability of recording a long-period video which outweighs the camera. Table 4.5 summarizes the specifications of the photography equipment.

Every experiment was filmed to observe the wetting front, the wall deformation, and the progression of the failure surface. Furthermore, the time lapse enabled the precise determination of the commencement of an incident and the corresponding time. A tripod was used to fixed the GoPro in place to take the video. Notably, the widescreen function was disabled to procure an orthographic video, minimizing the error of further investigation and post image analysis. The camera was adjusted to the designated aperture and shutter speed to take photos of the specimen during and after construction.

(a) (b)

Figure 4.19 Photography equipment: (a) GoPro 4; (b) Canon EOS 800D

doi:10.6342/NTU201901530

Table 4.5 Specifications of the photography equipment

Canon EOS 800D	
Lens mount	EF-S 18-55 mm f/4-5.6 IS STM
Effective resolution	24.20 megapixels
ISO sensitivity	ISO 100-25600
Shutter speed	30-1/4000 sec
Image format	JPEG
Image size	24 megapixels (6000 x 4000)
GoPro 4	
Effective resolution	12 megapixels
ISO sensitivity	ISO 100-6400
Image format	JPEG
Image size	12 megapixels
Video format	H.264
Video resolution	3840 x 2160

4.3 Test Procedures and Test Repeatability

4.3.1 Test Procedures

This study investigated the performance of a marginal backfilled GRS wall under rainfall conditions and improved methods were evaluated. The improved measures include reducing the spacing of the reinforcement, using granular backfill, and applying sand cushions at the soil-geogrid interface. The effects of the improved approaches were evaluated and compared and eventually the most efficient way was recommended.

First, the dimensions, including the spacing of the reinforcement and the backfill material were designed. The target rainfall intensity was then determined based on Taiwan Central Weather Bureau, the limitation of the irrigation system, and the permeability of the backfill soil. The weight and volume of the backfill soil needed for each layer was calculated subsequently. Next, the model GRS wall was constructed according to the procedures enunciated in Section 4.1.2. More specifically, the volumetric water content gauges were installed at the first, third and fifth layer. Finally, the blue Styrofoam molds were removed and the construction of the model GRS wall was completed.

doi:10.6342/NTU201901530

The amplifier, NI data logger, and the EM50 data logger were connected to the computer and the corresponding software was activated. The pore water pressures transducers were mounted at the designated locations and were checked before the experiment if the sensors were fully contacted to the model GRS wall. Afterwards, all the channels of the amplifier were tared. The water outlet of the sandbox is connected to a tube that guide the water to a ditch. The rainfall was activated once the light and camera were set. The rainfall lasted for 18 hours, which is equivalent to 7 days in the prototype. In addition, a drying period of 3 hours was adopted to observe the dissipation of the water. For the case of improved methods using granular backfill, a rainfall period of 5 hours, which is equivalent to 2 days in the prototype, was selected since the monitoring values reach the steady state in a much shorter time. The rainfall would be stopped earlier if failure commenced. Aside from recording the experiment, both the pore water pressure and the volumetric water content were monitored during the test.

4.3.2 Test Repeatability

Repeatability tests aim to convince the accuracy and precision of the test by administering the same test with the same materials, equipment, and configuration under the same condition by the same person. This section justifies the accuracy of the model tests by a repeatability test.

The model GRS walls for the repeatability test were backfilled with silty sand and were subjected to rainfall with an intensity of 75 mm/hr for 18 hours. The reinforcement spacing is 6 cm. The tests results were compared in terms of the volumetric water content and the wall displacement. Figure 4.20 shows the picture of the model GRS walls after the two experiments. It can be clearly seen that the two model walls looked the same after the tests. Figure 4.21 is the change of the volumetric water content during the repeatability tests. In both experimental group and control group, the water reached the bottom of the wall by 80 minutes and eventually achieved steady state at 110 minutes. The change of the volumetric water content in both tests followed the same pattern and had similar values. The wall displacement of the two model GRS walls is presented in Figure 4.22. It was suggested that the displacement of the walls was similar and were both small, with a maximum value of less than 0.5% of the wall height. The results of the repeatability test were in good agreement, suggesting that the result of the sandbox test is systematic and reliable.

doi:10.6342/NTU201901530

(a) (b)

Figure 4.20 Pictures of tests SM-S_v9: (a) Experimental group; (b) Control group

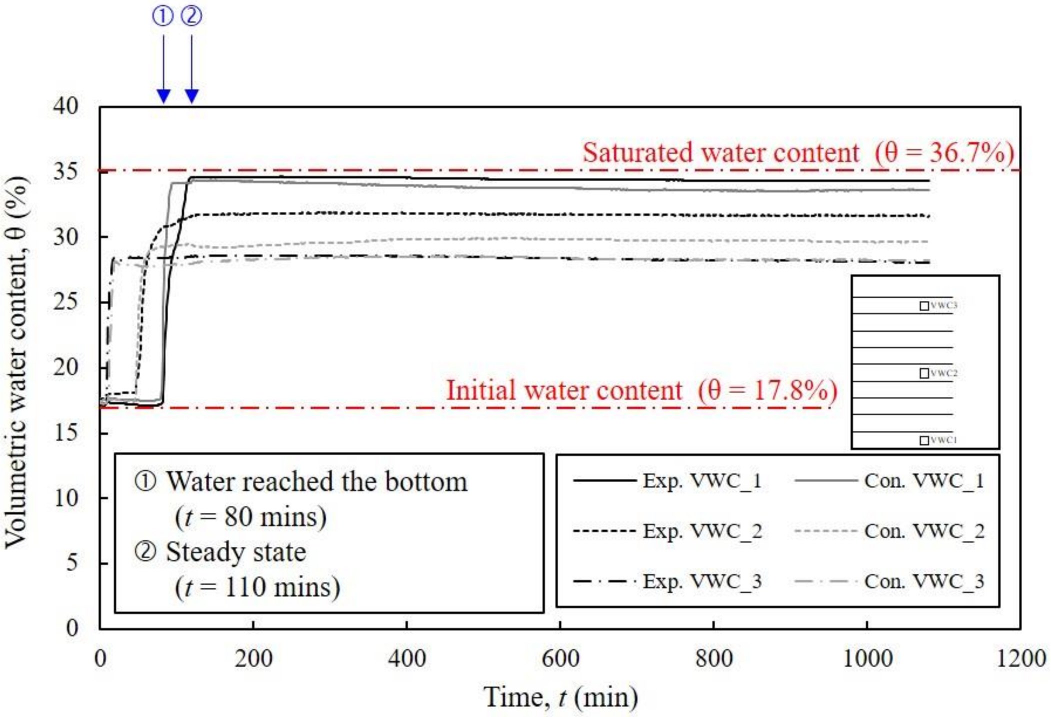

Figure 4.21 Variation of VWC throughout the test

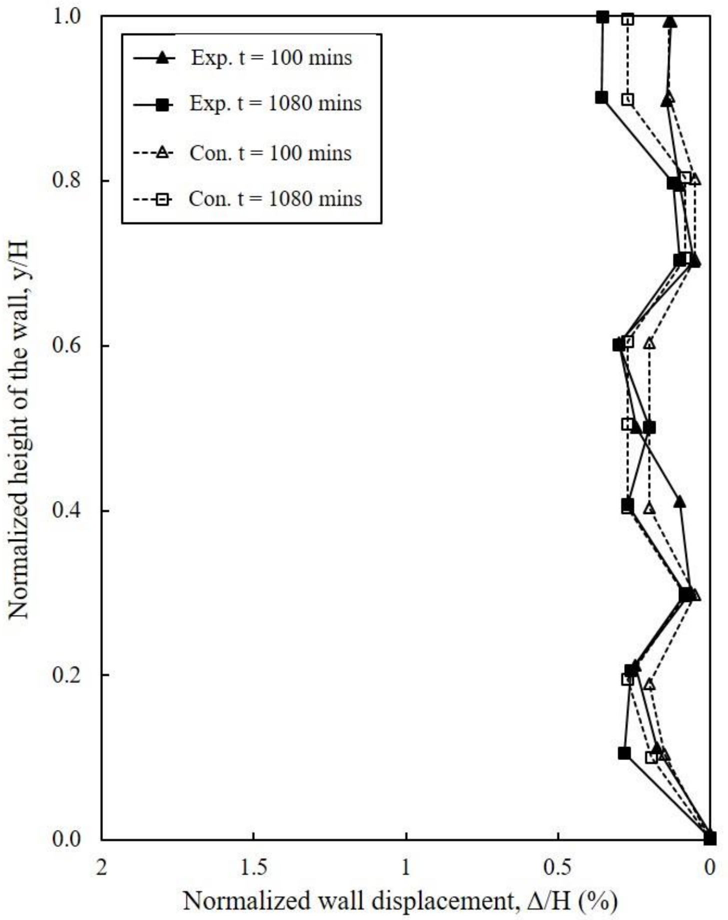

Figure 4.22 Wall displacement profile

4.4 Test Program

Table 4.6 summarized the test program and the factor of safety against breakage and pullout failure for each test. Test SM-S_v9 is the baseline case. The tests were numbered by the following rules. The first letter SM, or SP indicates silty sand or sand used as backfill. Moreover, S_v denotes that the reinforcement spacing is equal to 6, 9, and 12 cm. Finally, C4 indicates that sand cushions with 4 cm thickness were applied.

doi:10.6342/NTU201901530

Table 4.6 Test program

Model test		Measures	Number of reinforcement layers	Reinforcement spacing (cm)	Thickness of sand cushions (cm)	FS_{breakage}	FS_{pullout} (dry)	FS_{pullout} (wet)
Marginal backfill	SM-S_v9	(Baseline)	6	9	-	2.1	3.6	2.5
	SM-S_v12	Increase spacing	5	12	-	1.6	2.7	1.9
	SM-S_v6	Reduce spacing	10	6	-	2.8	3.6	2.5
Improved designs	SP-S_v9	Better backfill	6	9	-	2.4	6.5	6.4
	SM-S_v9-C4	Sand cushions	6	9	4	2.1	4.4	4.3
	SM-S_v12-C4	Sand cushions	5	12	4	1.6	3.3	3.2

doi:10.6342/NTU201901530

Chapter 5 Results of GRS Walls with Marginal Backfills

A series of reduced-scale model test of GRS walls with marginal backfill subjected to rainfall was conducted in this study. Six model tests were performed considering different reinforcement spacing, backfill material, and configurations. Among various remedial methods of designing a GRS wall with marginal backfill, this study investigated the effects of reducing the reinforcement spacing, selecting a backfill with better quality, and adopting sand cushions at the soil-geogrid interface.

The results of the GRS walls with marginal backfills are enunciated in this chapter. The results are presented in terms of the volumetric water content, the wall displacement, and the reinforcement strain. A thorough description of the failure mechanism is also provided.

5.1 Test Results

This section presents the results of the three model tests with marginal backfills. In addition to the demonstration of the results, the failure pattern and the mechanism were thoroughly discussed.

5.1.1 Test SM-S_v9 (Baseline Case)

Figure 5.1 shows the results of the test SM-S_v9. Both calculated *FS* and the photos of test results indicated that no internal failure was found; neither did pullout nor breakage failure occurred. However, the reinforced wall experienced a large deformation. Distinct cracks induced by wall deformation was observed inside the backfill.

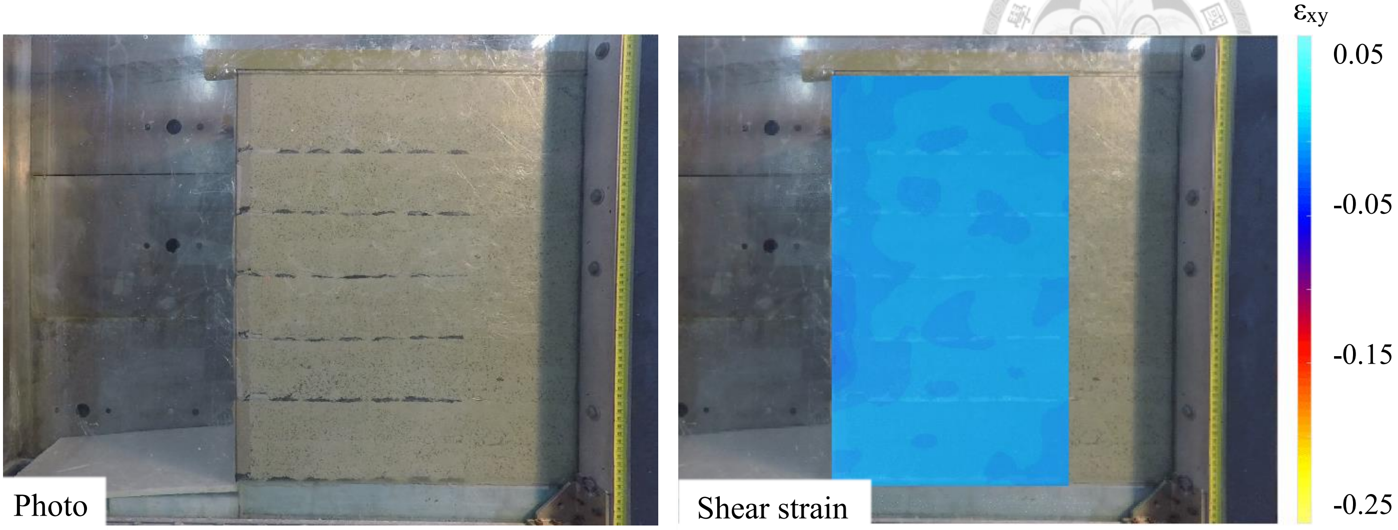

(a) ① Start of the test ($t = 0$ min)

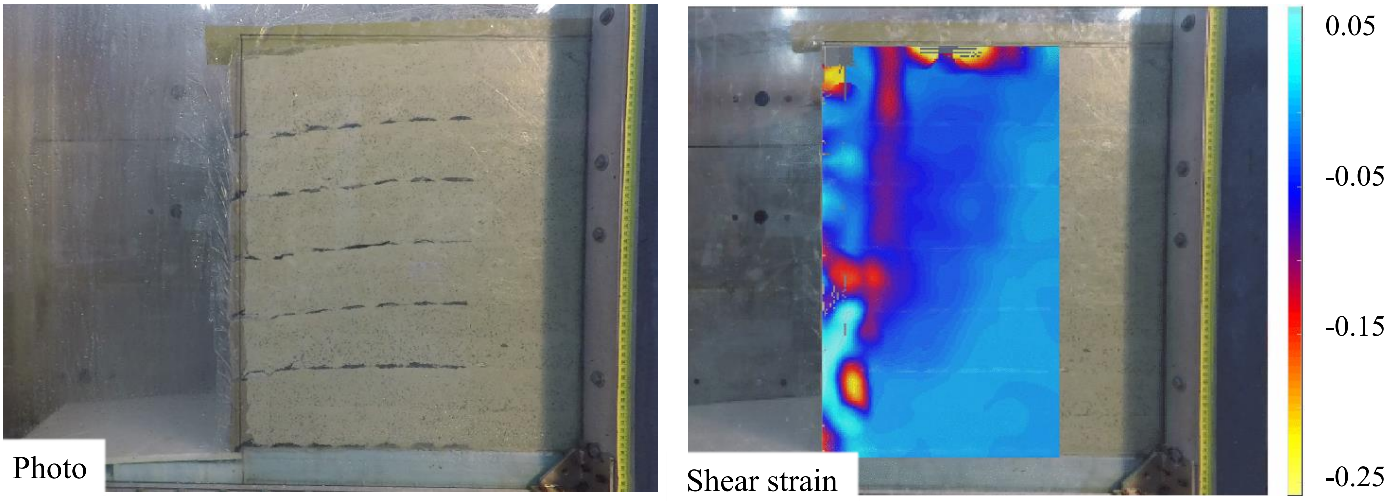

(b) ② Water reached the bottom ($t = 80$ mins)

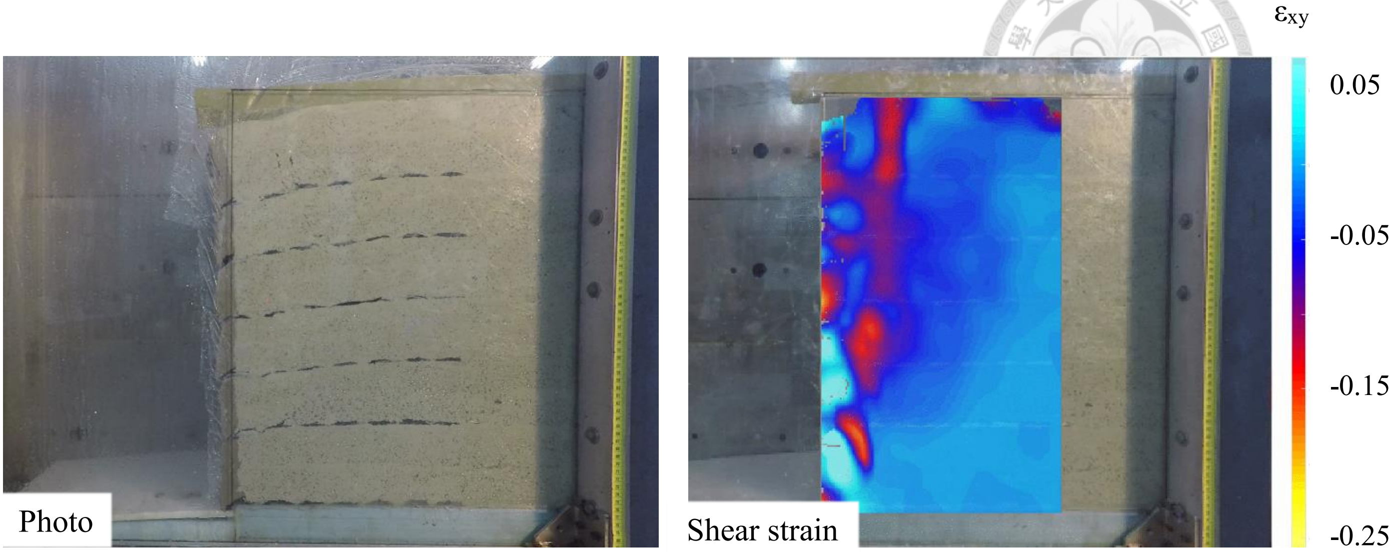

(c) ③ Steady state (t = 840 mins)

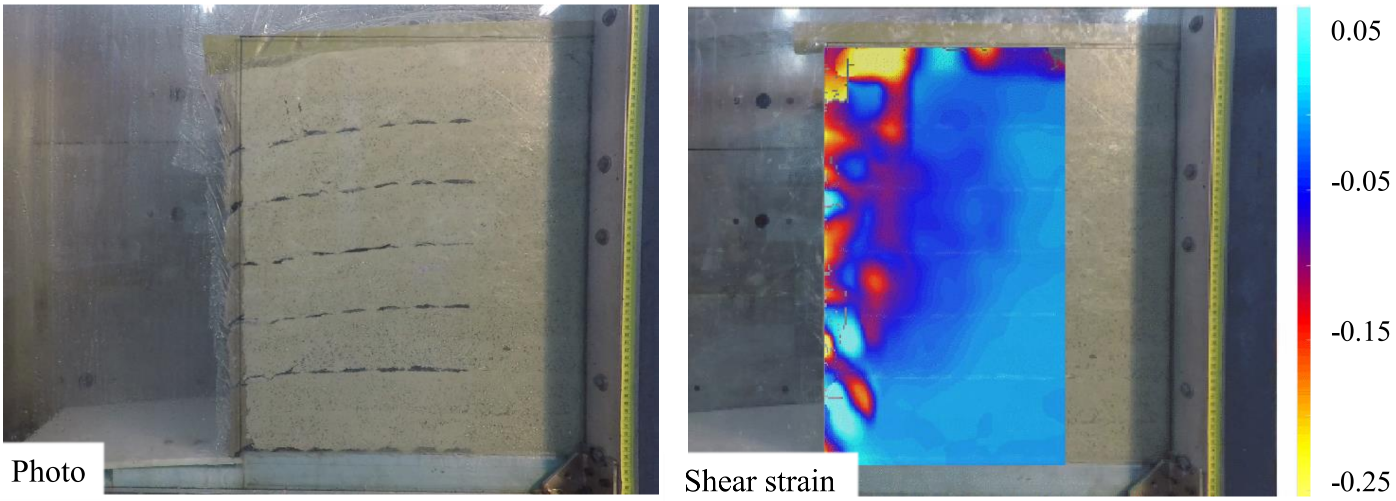

(d) ④ End of the test (t = 1080 mins)

Figure 5.1 Pictures of the model test SM-S_v9

doi:10.6342/NTU201901530

Figure 5.2 indicates the variation of the volumetric water content throughout the test. The important events were marked on the figure. It was suggested that VWC3 first sensed the flow of the water, followed by VWC2 and VWC1, conforming with the direction of water infiltration. Measured value is the same as the initial water content for soil preparation (θ = 17.8%). VWC3 showing a value exceeding saturation resulted from the displacement-induced crack inside the model wall. The cracks (Figure 5.3) led to the phenomenon that the volume of the water is larger than the volume of the soil particles, making the original calibration curve no longer applicable. VWC1 and VWC2 were not able to reach saturation because the permeability of the backfill soil was extremely small compared to the rainfall intensity (i/k = 5.4). VWC1 has larger value than VWC2 because of gravity; the water tended to flow down while some was still trapped in the top layers.

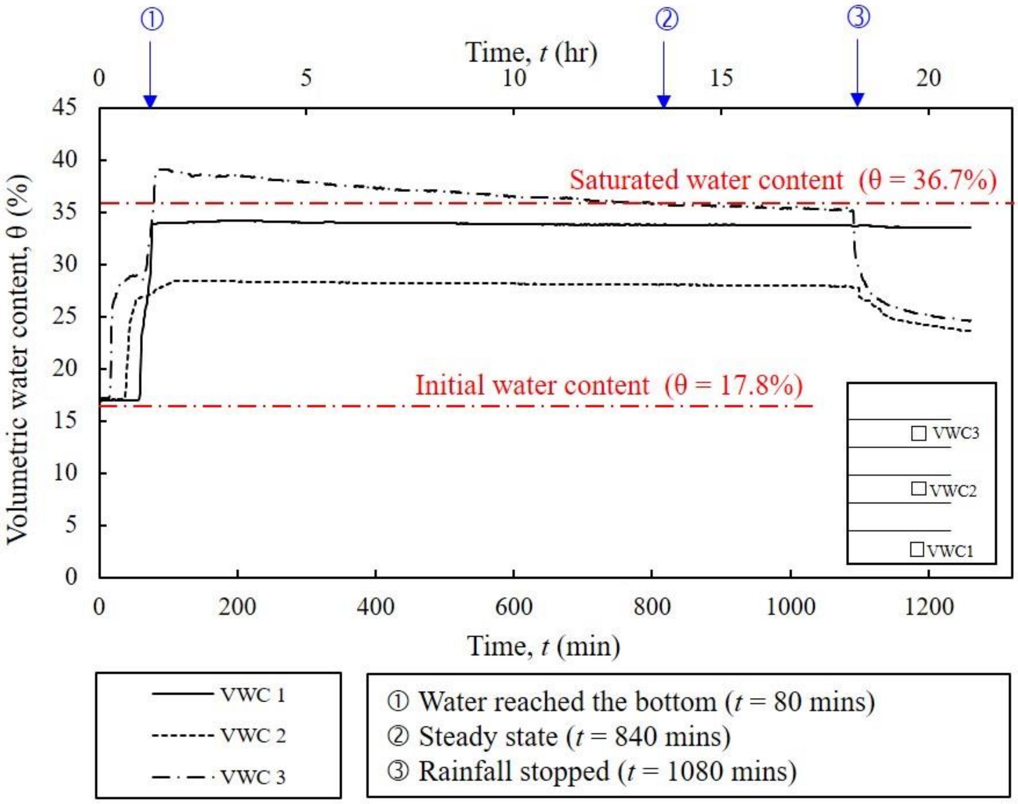

Figure 5.2 VWC with time elapse

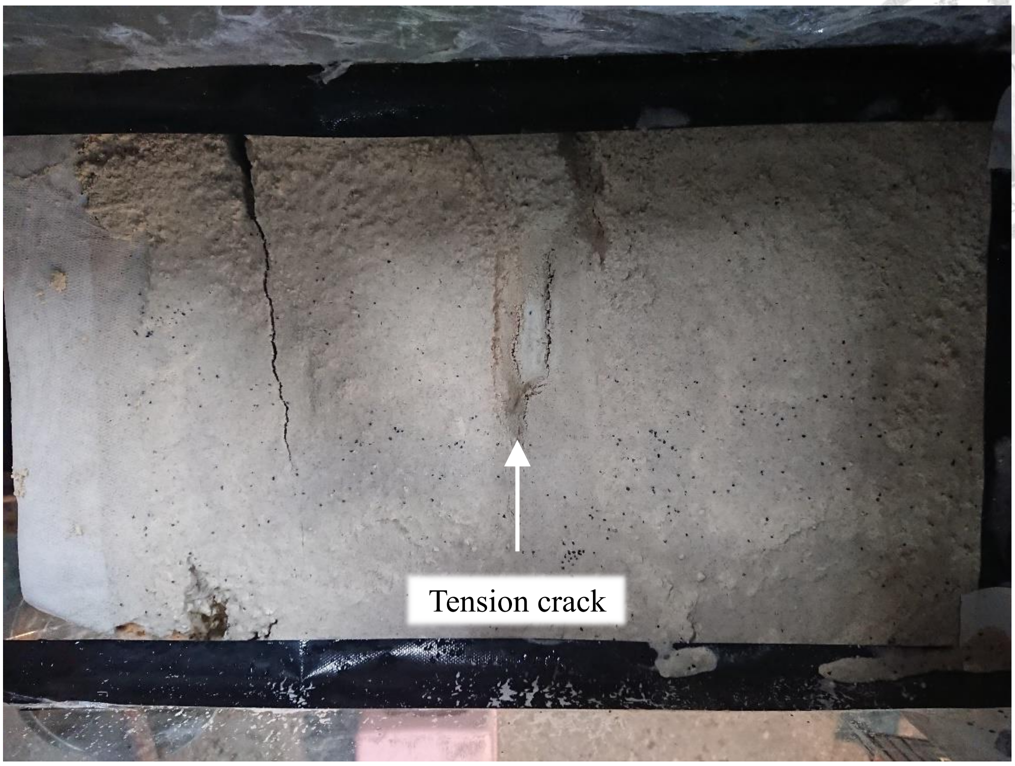

Figure 5.3 Picture of the cracks

Figure 5.4 indicates the wall facing displacement profile at different time of the test. The figure suggested that the wall had moved when the water reached the bottom (t = 80 mins). Since the permeability of the backfill is relatively low, the infiltrated rainfall concentrated at the top. Therefore, the maximum displacement was found at the topmost layer, around 15% of the wall height, forming a cantilever type of deformation. The bottom of the wall hardly moved because the friction between the model wall and the foundation was large enough to prevent sliding.

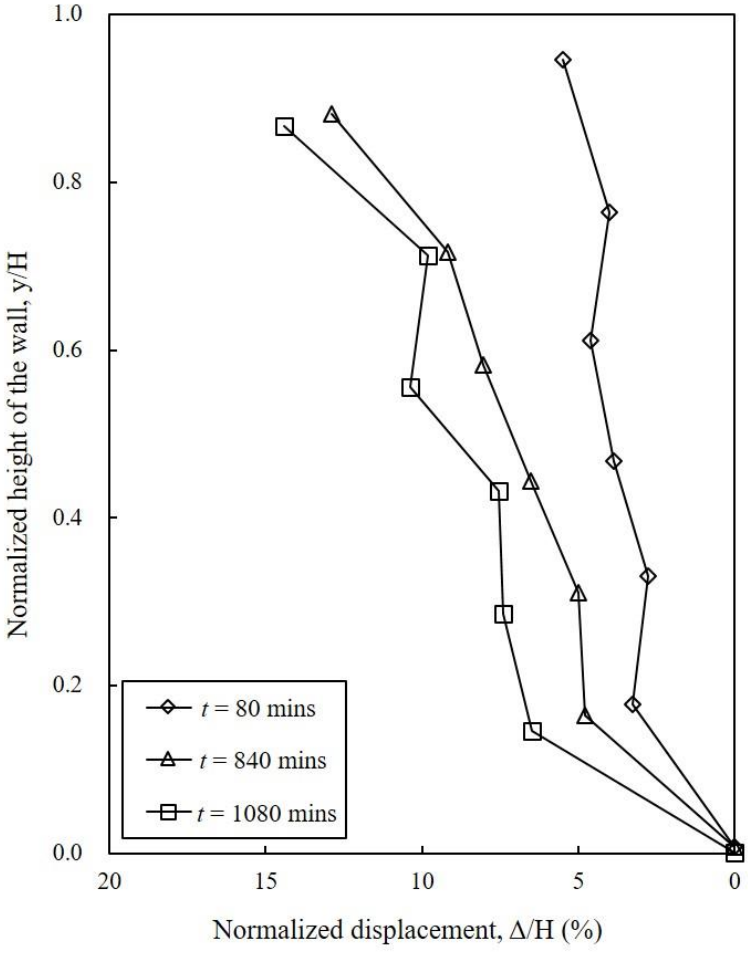

Figure 5.4 Wall displacement profile

doi:10.6342/NTU201901530

Figure 5.5 presents the maximum wall displacement and settlement versus time. The major displacement of 5 cm happened 1 hour after the rainfall started because of the influence of water infiltrated into the specimen, which caused the loss of matric suction in the backfill. Afterward, the wall displacement was progressively developed. A relatively small successive movement (3 cm) as rainfall proceeded and the wall eventually reached steady state. The geogrid reinforcement was able to minimize excessive wall displacement. The allowable displacement after construction indicated in the figure was based on the regulations of FHWA and AASHTO. In this study, a model GRS wall with 60 cm high and extensible geogrid as the reinforcement, the allowable displacement upon construction is 0.96 cm.

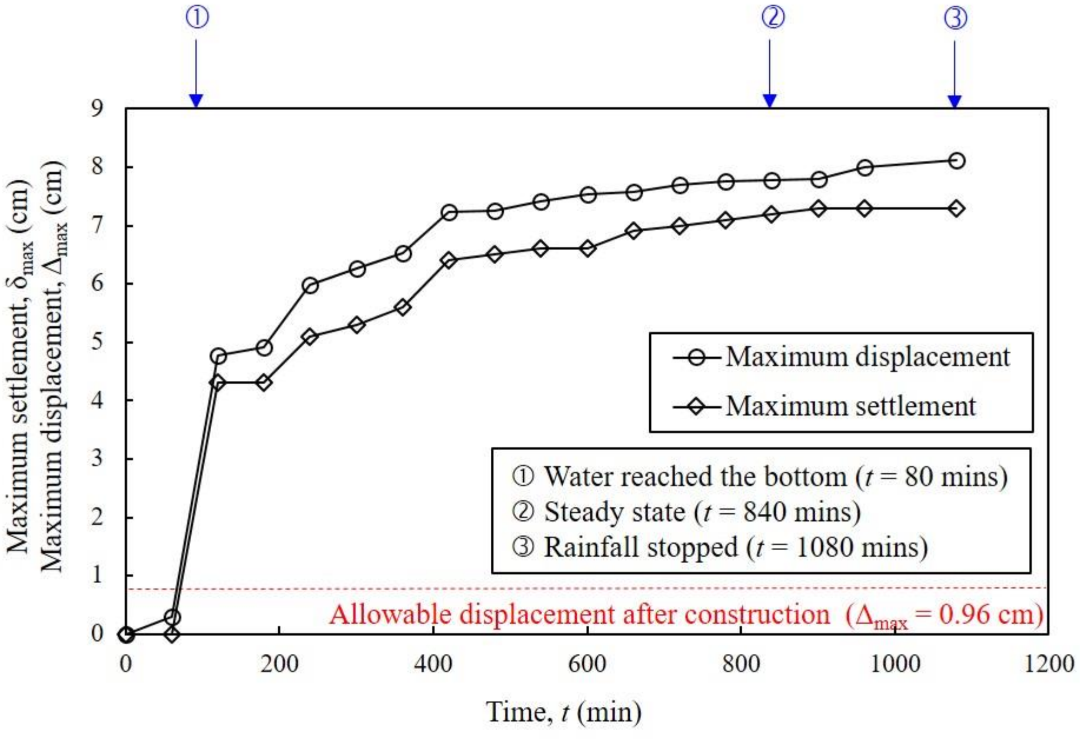

Figure 5.5 Maximum wall displacement and settlement versus time

Figure 5.6 presents the reinforcement strain mobilized in each layer, analyzed via PIV analysis. The reinforcement strain is significantly larger in the top layers ($\varepsilon = 4\%$), which corresponds to the observed wall displacement. Specifically, the reinforcement strain at the first layer is barely mobilized because of the limitation from the foundation friction, whereas the maximum strain of around 4% occurred in the 6th layer where the largest displacement took place. The locus of maximum reinforcement strain in each layer, as shown in Figure 5.6, indicates the potential sliding surface Strain contour from PIV analysis is also shown on the figure. The potential sliding surface corresponded with the area with intense shear strain. Notably, the maximum shear strain estimated by the PIV analysis was equivalent to 36%, this value is considered beyond the soil failure strain according to the triaxial test results, suggesting the soil along the potential sliding surface had reached the limit state. The stability of the reinforced wall at this stage was mainly sustained by the mobilized reinforcement tensile force. The shear band indicated by the locus of the maximum tensile strain corresponds to the strain contour from the PIV analysis; meanwhile, both results coincide with the potential sliding surface as observed.

Figure 5.7 displays the maximum reinforcement tensile force profile. The dashed line is calculated from Rankin's earth pressure method. The figure indicates that the mobilized reinforcement tensile force at the top layers was much larger than that calculated from earth pressure method. Moreover, the wall displacement was cantilever, causing the maximum mobilized reinforcement tensile force at the top, which was significantly different from that indicated by the earth pressure method.

doi:10.6342/NTU201901530

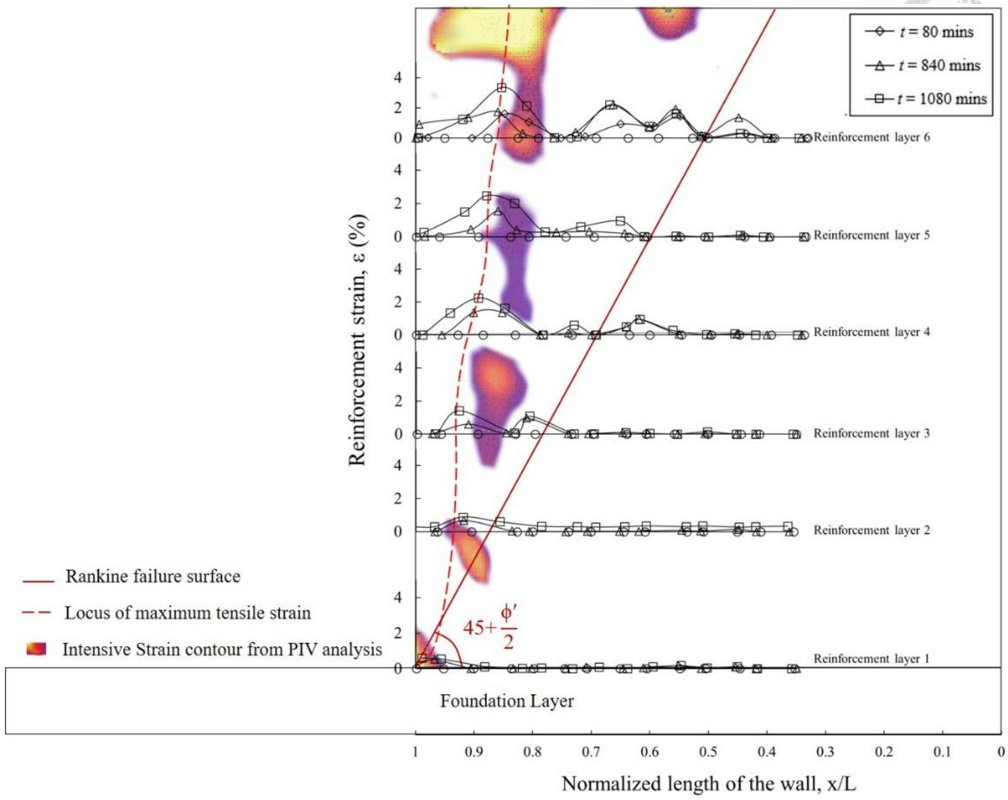

Figure 5.6 Reinforcement tensile strain and comparison of potential sliding surface

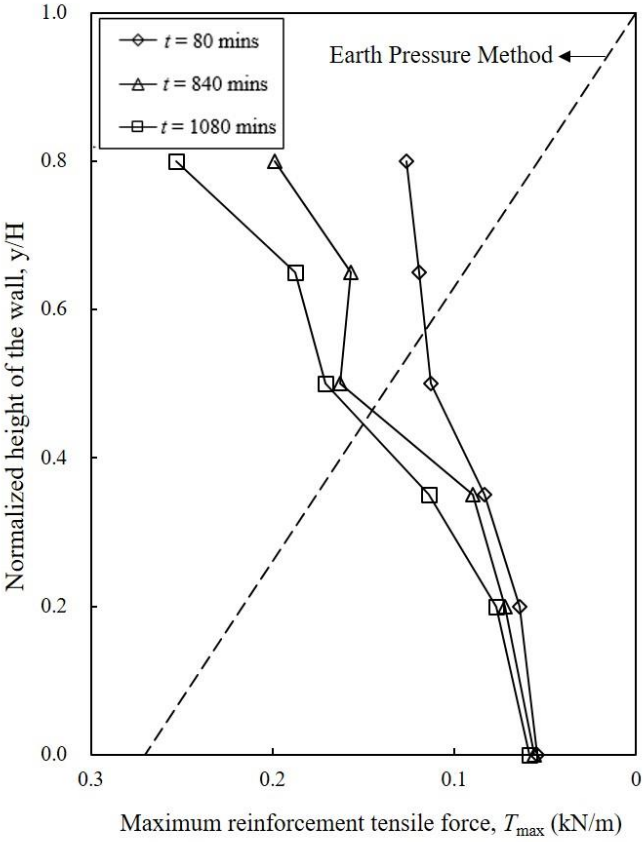

Figure 5.7 Maximum reinforcement tensile force profile

doi:10.6342/NTU201901530

In summary, due to the development of large wall deformation and the soil shear strain, the reinforced wall of test SM-S_v9 was considered unstable under the prescribed rainfall condition. Large wall displacement and tensions cracks were observed, albeit the high factor of safety. The displacement was issued from the loss of matric suction owing to the infiltrated rainfall confined at the top layers. Furthermore, reinforcement tensile strain was mobilized and the soil had reached its limit state, forming a potential sliding surface. Improved methods should be proposed to optimize the design of GRS walls with marginal backfill.

5.1.2 Test SM-S_v12 (Increase Spacing)

Figure 5.8 presents the photos of the test SM-S_v12. The reinforced wall in this test failed in interlayer sliding mode. The wall displacement was too large for the PIV software to estimate the soil shear strain, so only the pictures during the test were presented. At t = 85 mins, the development of the first tension crack was observed at the top of the wall. At t = 94 mins, the second tension crack developed. Figure 5.9 shows a picture of the wall after collapse. Excessive wall displacement had ensued as rainfall proceeded, consequently causing the flip over of the wrap-around part of the top two layers.

(a) ① Start of the test (t = 0 min)   (b) ② First tension crack (t = 85 mins)

(c) ③ Second tension crack (t = 94 mins)   (d) ④ Before wall collapsed (t = 126 mins)

Figure 5.8 Pictures of the model test SM-S_v12

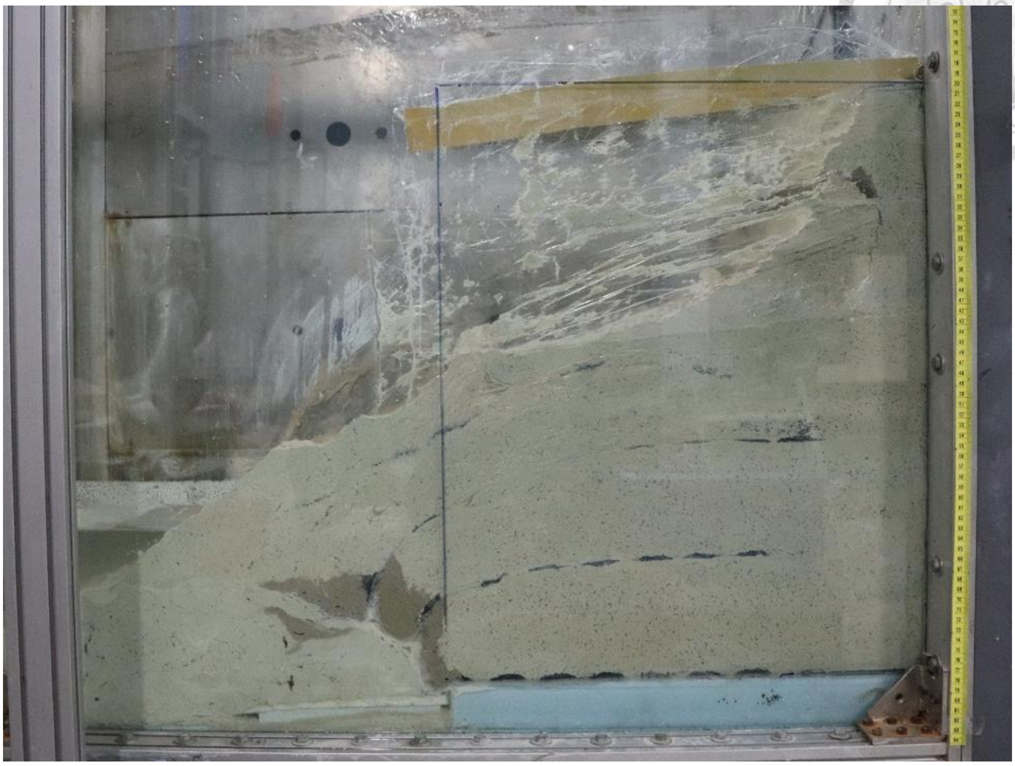

Figure 5.9 Collapse of the wall

doi:10.6342/NTU201901530

Figure 5.10 shows the change of the VWC with time elapse. The increase of θ commenced in the order of VWC3, VWC2, and VWC1 as the water flowed from the top to the bottom. Notably, the water filled in the cracks, causing the measured VWC value exceeded saturation. The values for VWC3 and VWC2 were therefore cut off in succession upon the development of the tension cracks at 85 mins and 94 mins, respectively. The development of the cracks might issue in the longer time for water to reach the bottom of the wall (t = 115 mins) compared to the test SM-S_v9 (t = 80 mins). VWC3 registered the highest θ value, indicating that the water was confined in the top layers, causing the loss of matric suction. This is correlated to the observation that the deformation was the largest at the top layer where failure first commenced.

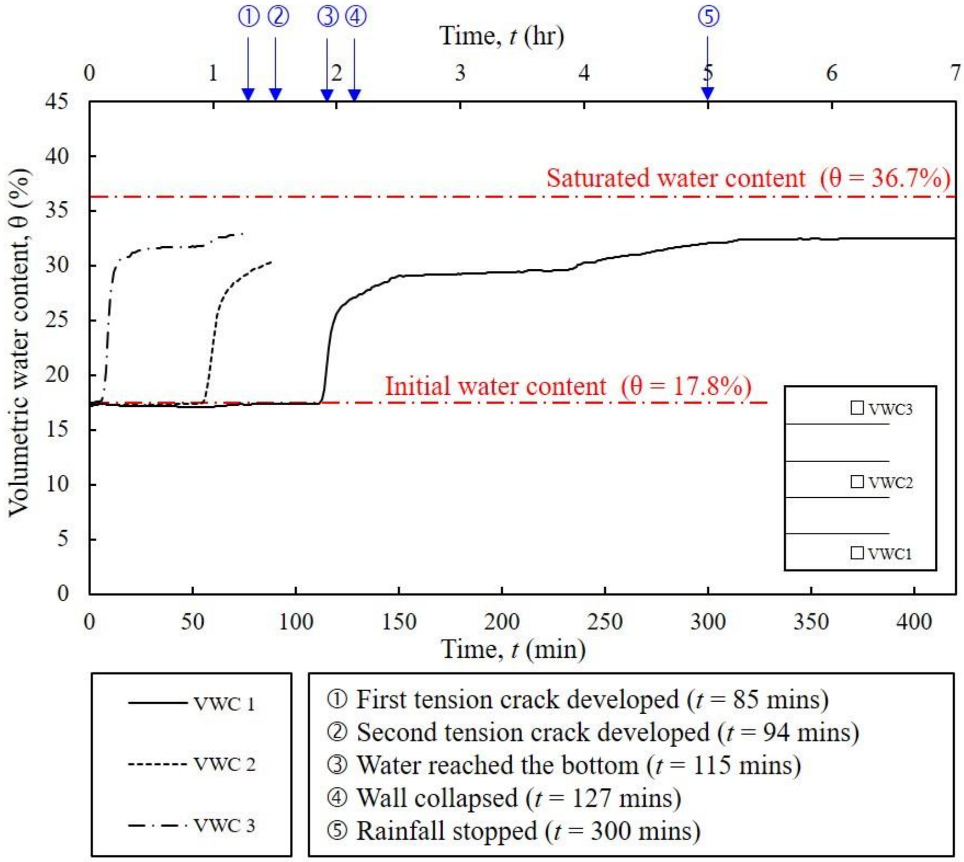

Figure 5.10 VWC with time elapse

doi:10.6342/NTU201901530

Figure 5.11 shows the development of the wall displacement profile of the reinforced wall before failure. When $t \leq 94$ mins, before the two tension cracks were fully developed, the wall only deformed around 6% of the wall height. The wall continued to deform in the following 30 minutes and eventually collapsed. The maximum wall displacement before the wall failure was 32% of the wall height. The wall displacement increased with the increase of the elevation, displaying same deformation pattern as the test SM-S_v9. The excessive deformation eventually dismissed the effect of the wrap-around although the wrap-around length for the topmost layer was extended.

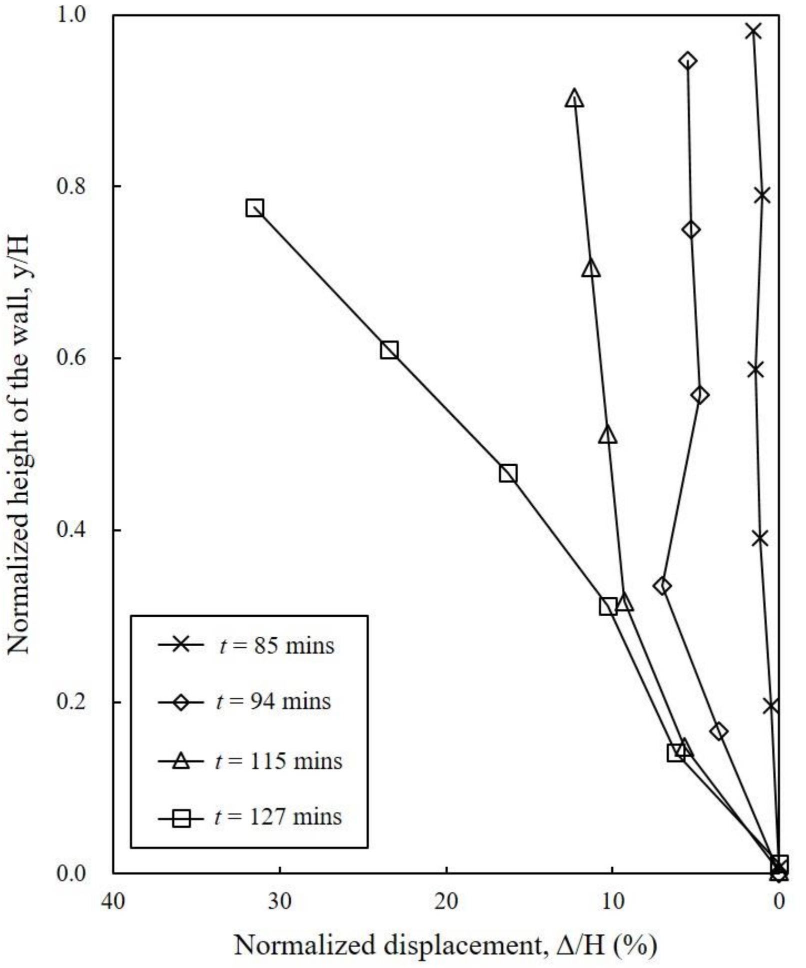

Figure 5.11 Wall displacement profile

Figure 5.12 presents the maximum wall displacement with time. Displacement increased dramatically after the two tension cracks fully developed (t = 94 mins) likely because the water filled into the voids, resulting in the reduction of the shear strength a t the soil-geogrid interface. The wall displacement was only 2 cm at $t \leq 94$ mins; however, the displacement continued increasing in the next 30 minutes and reached a maximum displacement of 11 cm right before the wall collapse. The soil can no longer withstand the lateral earth pressure due to the failure of the soil mass induced by the loss of matric suction and soil shear strength. The wrap-around of the topmost layer flipped over and the second layer failed in a resembling manner 90 minutes after that. The collapsed soil piled up and block the lower part of the reinforced wall. The remaining layers, layers 3, 2, and 1, would have failed in the resembling manner in succession without the limitation of the sandbox.

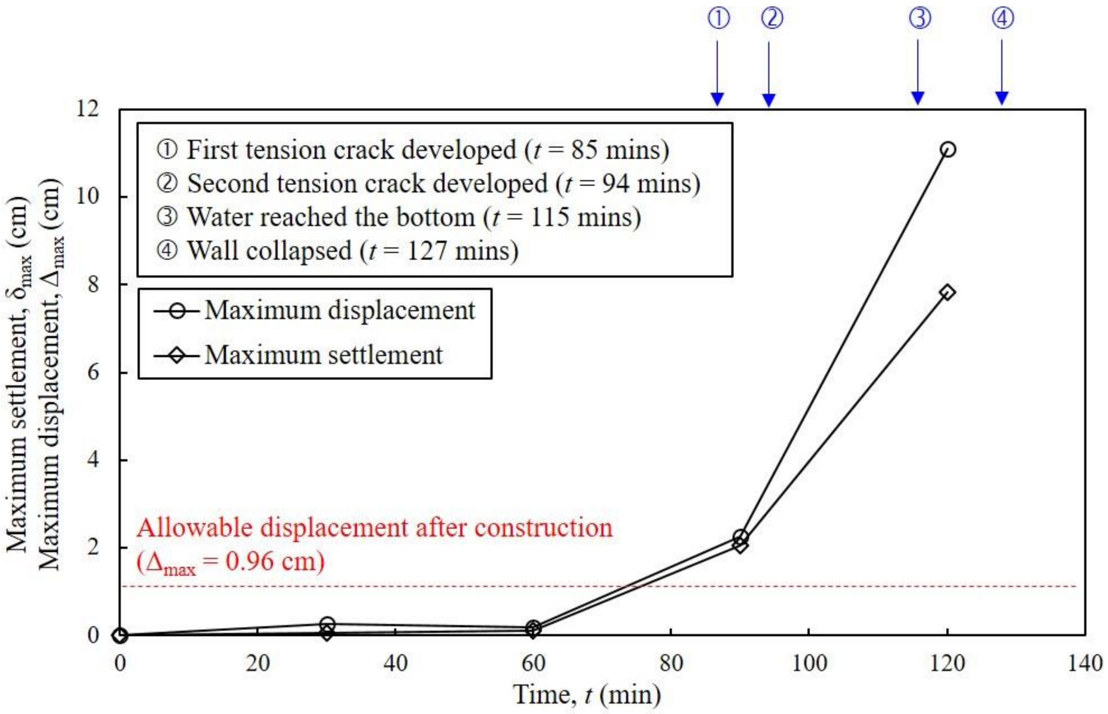

Figure 5.12 Maximum wall displacement and settlement versus time

doi:10.6342/NTU201901530

Figure 5.13 shows the mobilized reinforcement tensile strain in each layer before the wall collapsed. The largest displacement occurred in the top two layers, causing large reinforcement tensile strain be mobilized ($\varepsilon = 5\%$). The soil shear strain could not be estimated in the test SM-S_v12 due to the limitation of the PIV software. The locus of maximum reinforcement strain in each layer was connected, indicating the critical failure surface. Notably, Rankine's failure surface corresponded to the secondary potential sliding surface indicated by the locus of larger reinforcement tensile strain.

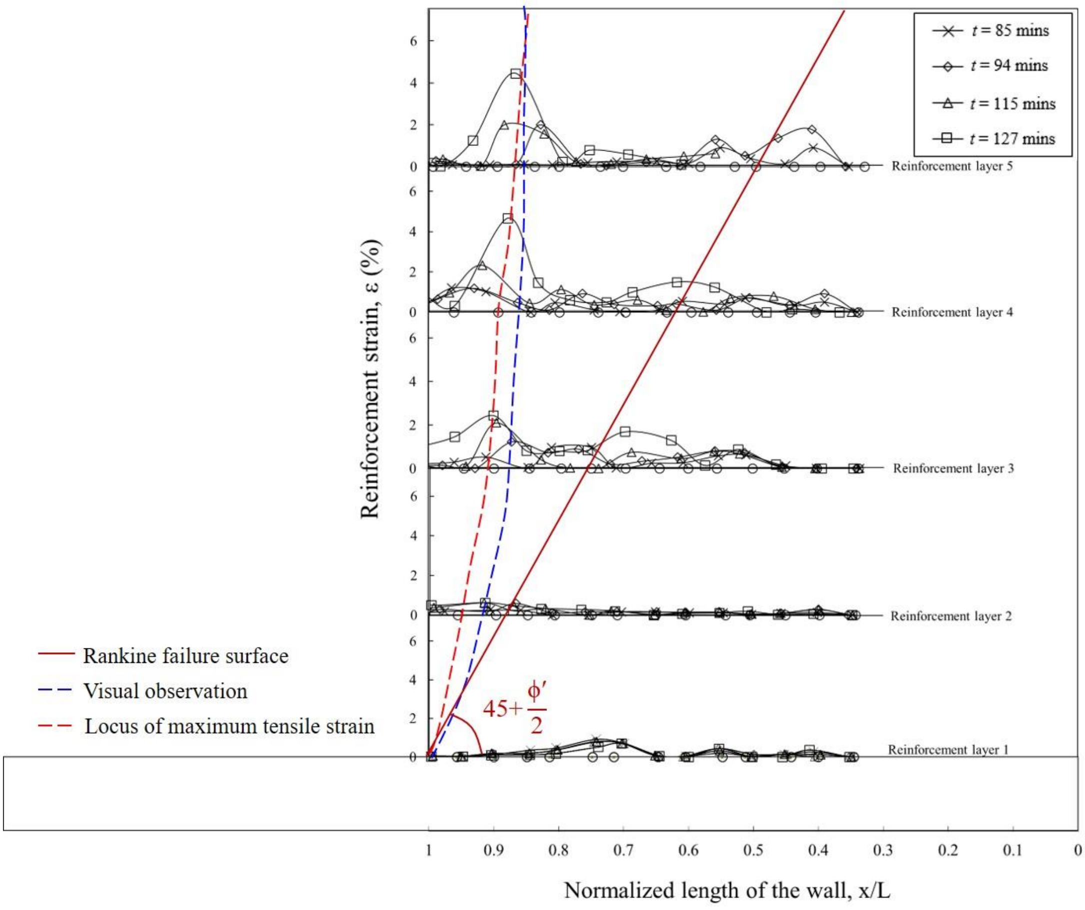

Figure 5.13 Reinforcement tensile strain and comparison of potential sliding surface

Figure 5.14 presents the maximum reinforcement tensile force profile. The mobilized reinforcement tensile strain showed similar pattern, cantilever type, as the wall displacement, which is different from the pattern suggested by the Rankine's earth pressure method. Therefore, the reinforcement at the top layers should be enhanced.

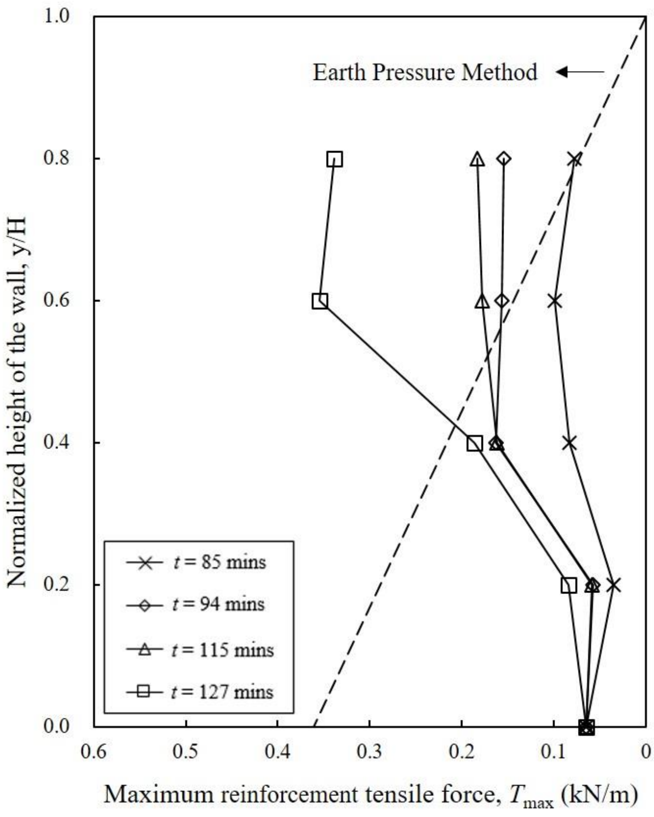

Figure 5.14 Maximum reinforcement tensile force profile

In summary, the reinforced wall of the test SM-S_v12 failed under the prescribed rainfall condition. The failure mode observed from the test is the interlayer sliding failure. The failure occurred at t = 127 mins, shortly after the rainfall was applied. The infiltrated rainfall led to the increase of θ in the top layer, causing the loss of matric suction and soil shear strength. Afterward, tension started to develop (t = 85 mins). At this stage, the lateral earth pressure was all resisted by the geogrid reinforcement. With continuous decrease in the soil-geogrid interface shear strength induced by the water accumulation in the tension cracks, the reinforcement eventually flipped over and the reinforced wall collapsed, even with a doubled wrap-around length.

5.1.3 Test SM-S_v6 (Reduce Spacing)

Figure 5.15 presents the photo of the model wall at the initial condition and the end. The wall remained stable and negligible displacement developed throughout the test because the spacing of the reinforcement is small enough to reinforce the marginal backfill. No failure was found as indicated by the rather high factor of safety and the observation after the test; neither was the displacement observed.

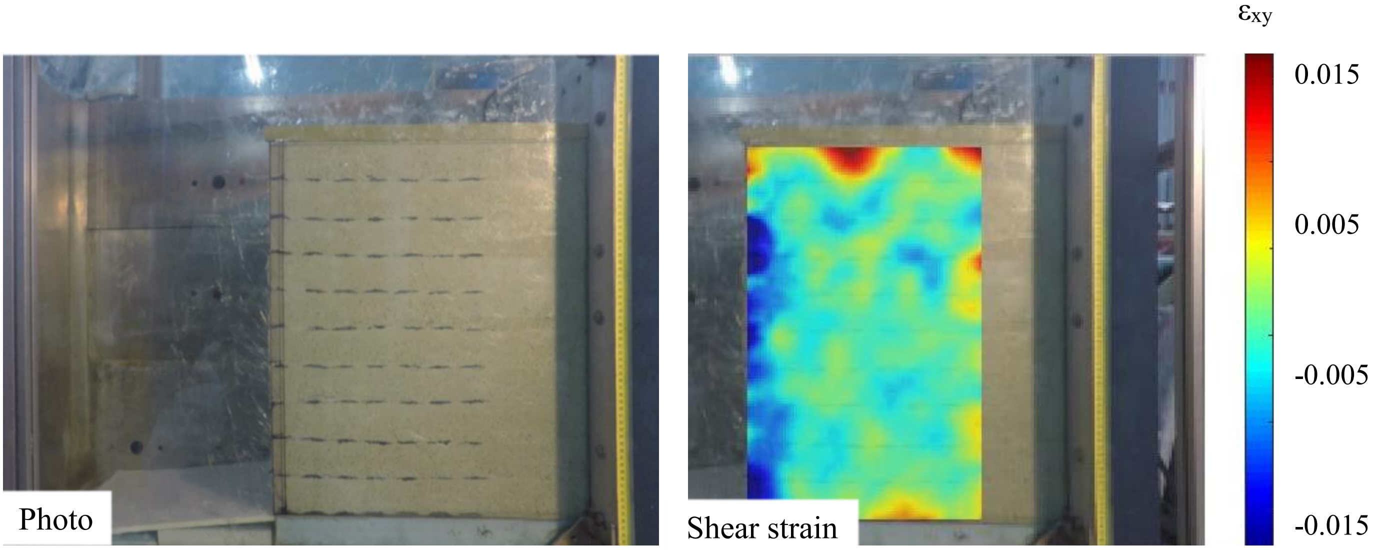

(a) Start of the test (t = 0)

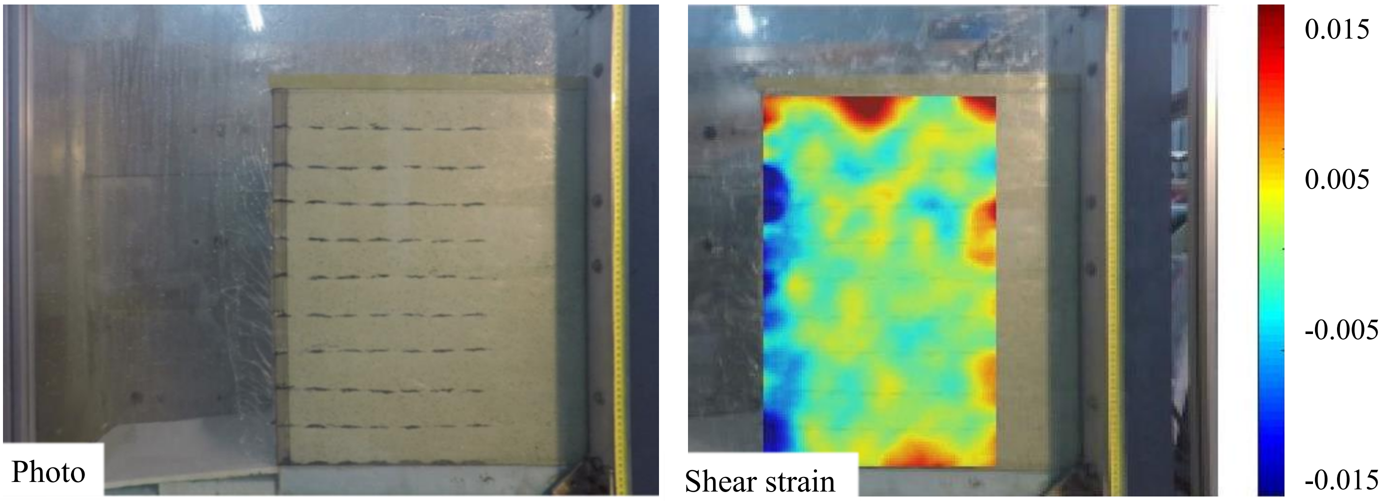

(b) End of the test (t = 1080 mins)

Figure 5.15 Pictures of the model test SM-S_v6

doi:10.6342/NTU201901530

Figure 5.16 presents the change of the volumetric water content during the test. Clearly, VWC3, which was located at the top, sensed the wetting front first as the water infiltrated from the top to the bottom, followed by the increase at VWC2 and VWC1. Eventually, VWC1 registered the highest water content and reached saturation approximately.

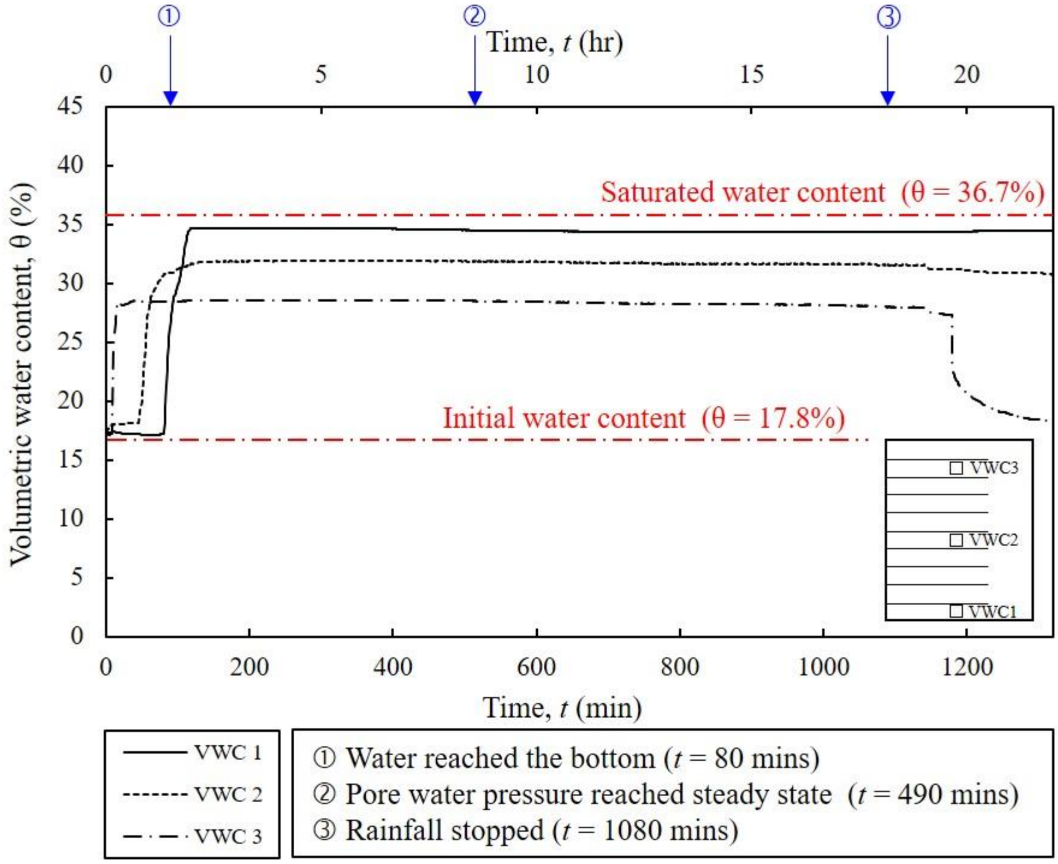

Figure 5.16 VWC with time elapse

Figure 5.17 shows the wall displacement profile. The figure suggests that the maximum wall displacement was less than 0.3% of the wall height, which is considered too small to be observed by visual investigation. Since the reinforcement spacing is very small, the wall is stable enough to experience only minor displacement less than 1 cm.

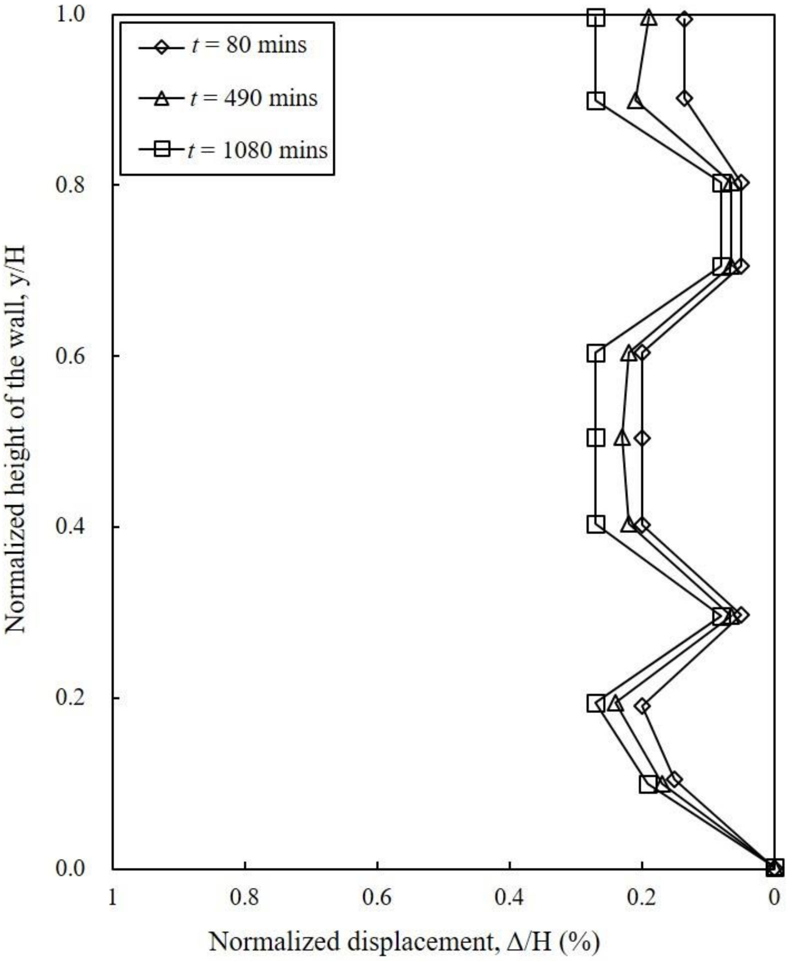

Figure 5.17 Wall displacement

doi:10.6342/NTU201901530

Figure 5.18 demonstrates the mobilized reinforcement strain in each layer. Little reinforcement strain was mobilized (less than 0.4%) since there was no significant relative displacement, as indicated by the wall displacement curve. Moreover, the shear strain contour and Rankine's failure surface were not plotted on the figure because only small displacement was investigated, and no potential sliding surface was observed as the reinforcement strain is minor.

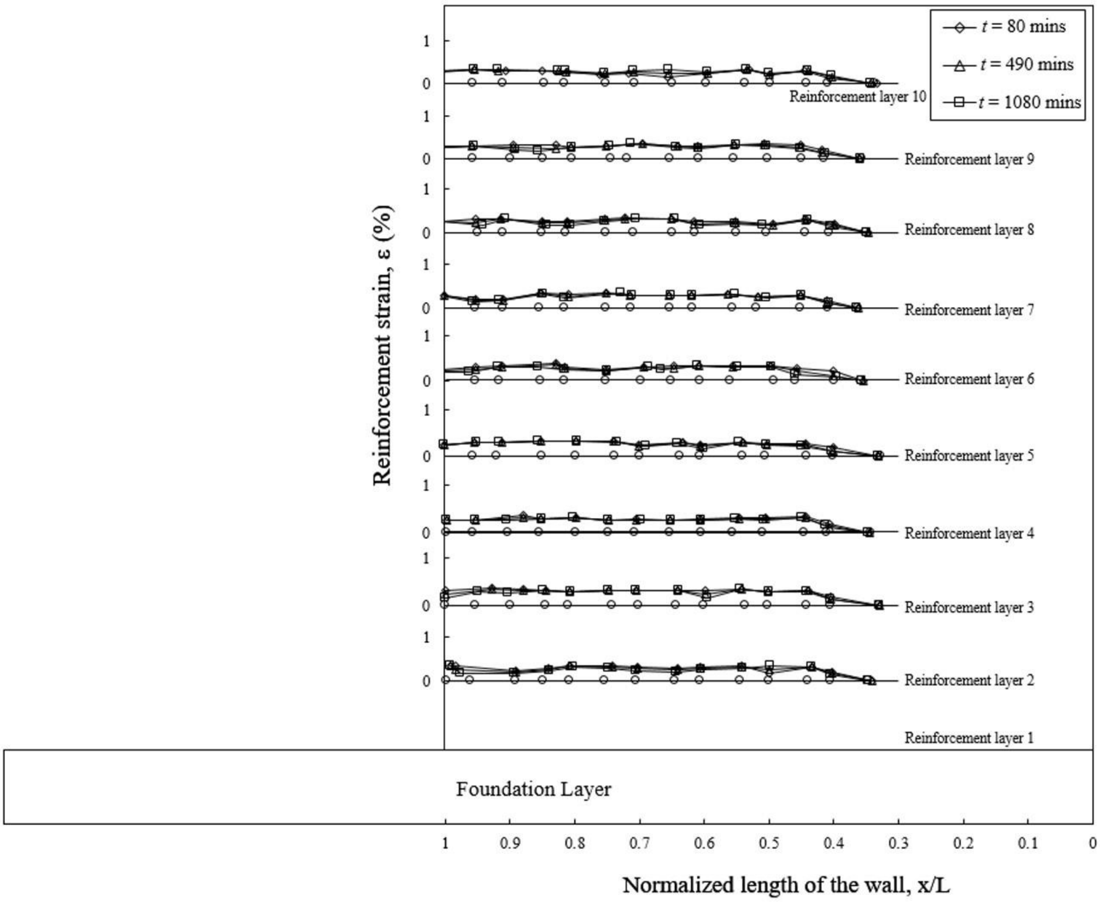

Figure 5.18 Reinforcement strain

Figure 5.19 displays the maximum reinforcement tensile force profile. The mobilized reinforcement tensile strain was smaller than the values indicated by the earth pressure method since the wall hardly moved. The mobilized reinforcement tensile strain was uniformly small; the earth pressure method overestimated the tensile strain at the bottommost layer by 3.5 times.

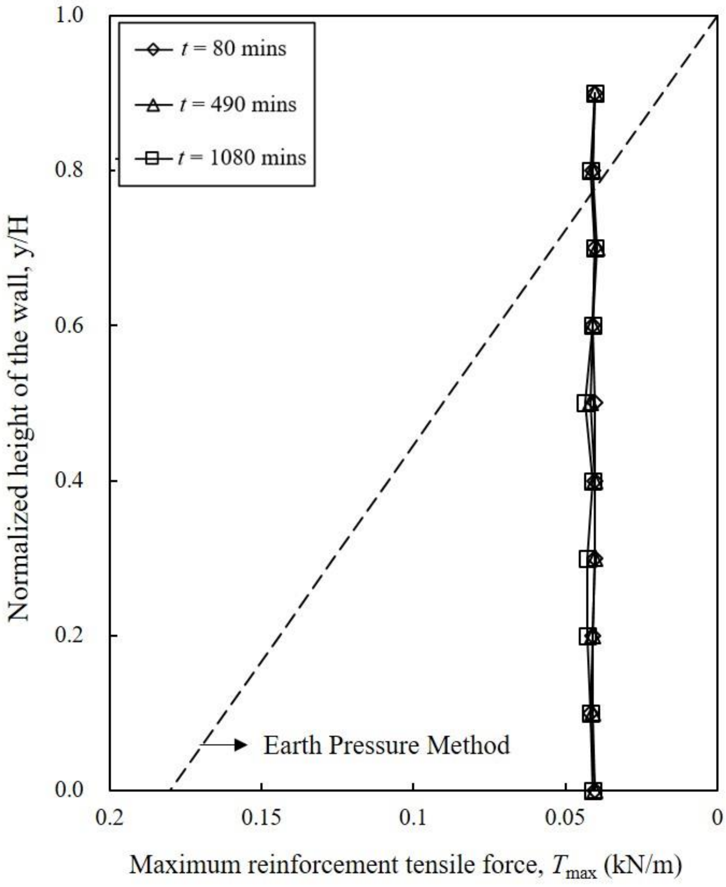

Figure 5.19 Maximum reinforcement tensile force profile

In summary, the spacing is small enough to ensure high stability of the wall so that there is no significant locus of the maximum tensile strain. Failure did not occur in this case.

doi:10.6342/NTU201901530

5.2 Effects of Spacing

The test results of reinforced walls with three different spacing, S_v = 6, 9, and 12 cm, were compared in this section. Figure 5.20 shows the pictures of the three wall models at the end of the tests. The comparison of the *FS*, wall displacement, and the overall performance of the three tests is provided in this section.

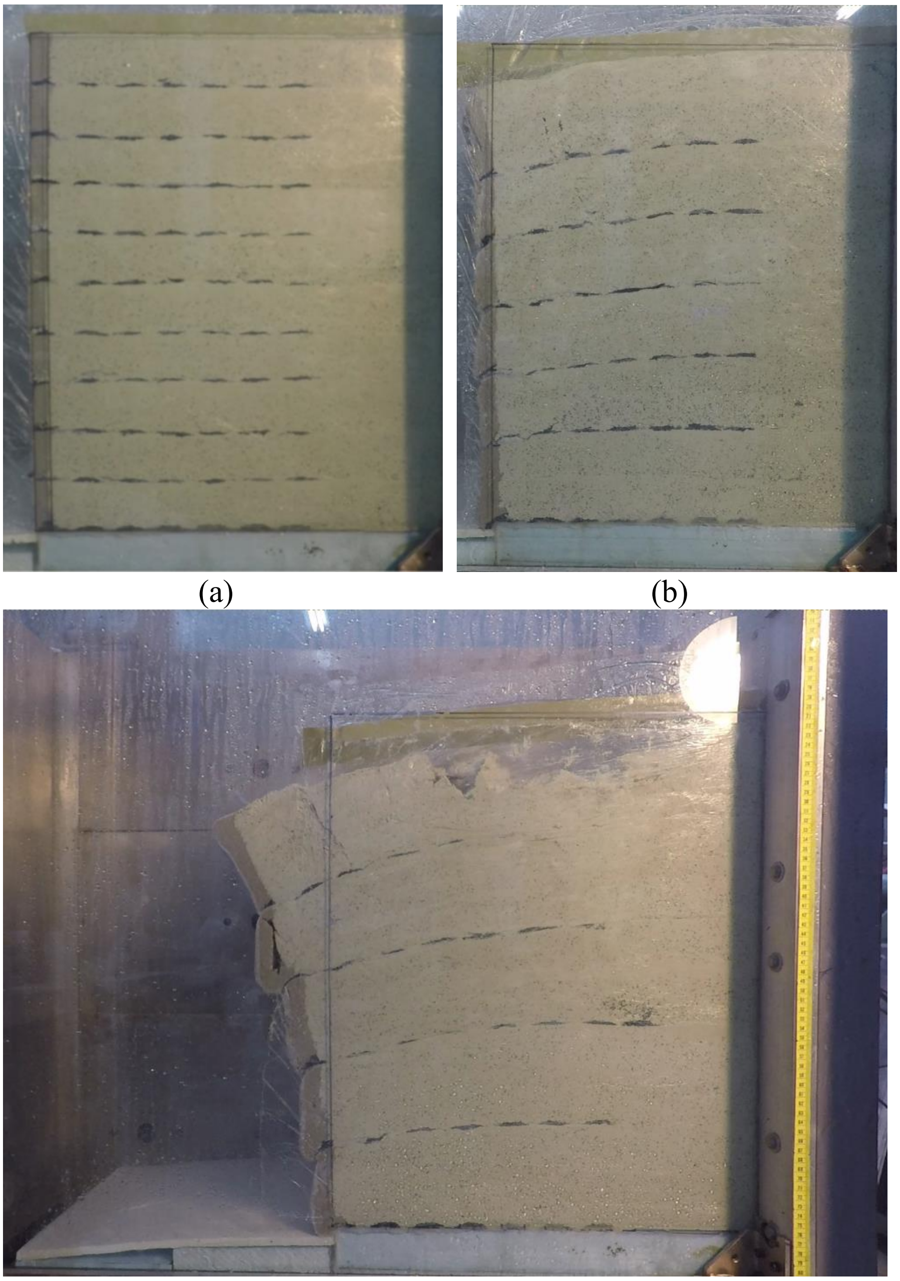

(a) (b)

(c)

Figure 5.20 Pictures of tests: (a) SM-S_v6; (b) SM-S_v9; (c) SM-S_v12

Figure 5.21 presents the factor of safety against breakage and pullout failure for the three cases. The factor of safety increases with the decrease of the reinforcement spacing. The *FS* in the test SM-S_v6 is the highest ($FS_{\text{breakage}} = 2.8$ and $FS_{\text{pullout}} = 3.6$) whereas the *FS* in the test SM-S_v12 is the lowest ($FS_{\text{breakage}} = 1.6$ and $FS_{\text{pullout}} = 2.7$). FS_{breakage} in the test SM-S_v12 is only slightly larger than the required value (*FS* = 1.5). Notably, the required *FS* was designed under normal condition. The test SM-S_v12 failed under the prescribe rainfall condition, therefore indicating that the *FS* under rainfall conditions needs further modification.

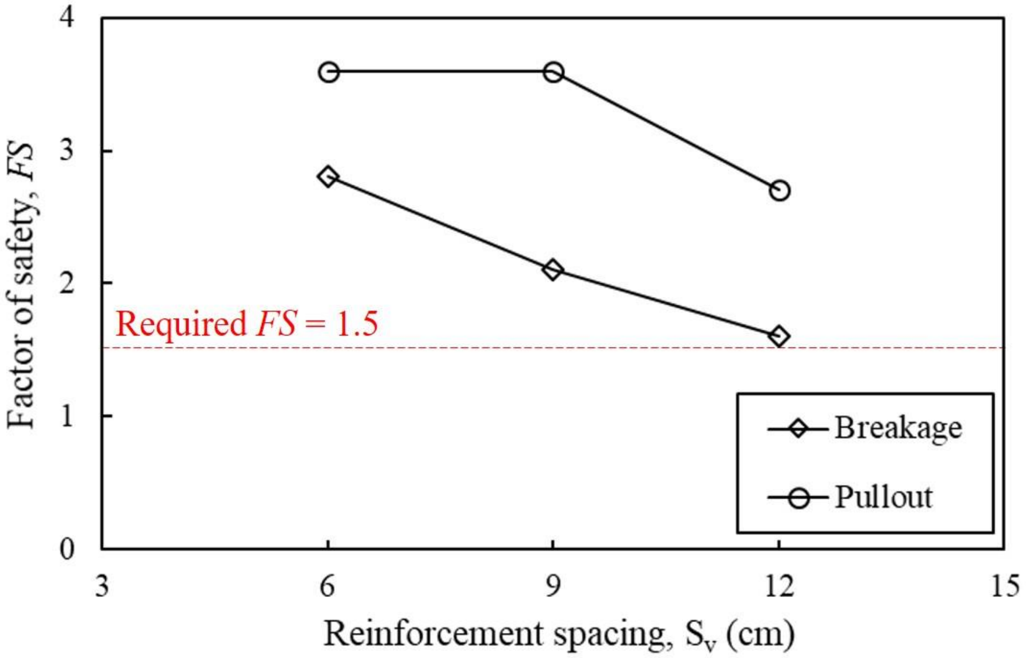

Figure 5.21 Factor of safety under different reinforcement spacing

doi:10.6342/NTU201901530

Figure 5.22 shows the comparison of the wall displacement profile of reinforced walls with marginal backfills under different reinforcement spacing. The maximum wall displacement increased with the increase of reinforcement spacing. The maximum wall displacement was 32%, 13%, and 0.1% of the wall height in the test SM-S_v12, SM-S_v9, and SM-S_v6, respectively. The figure suggests that with 25% reduction in the reinforcement spacing, a maximum of 50% wall displacement can be reduced.

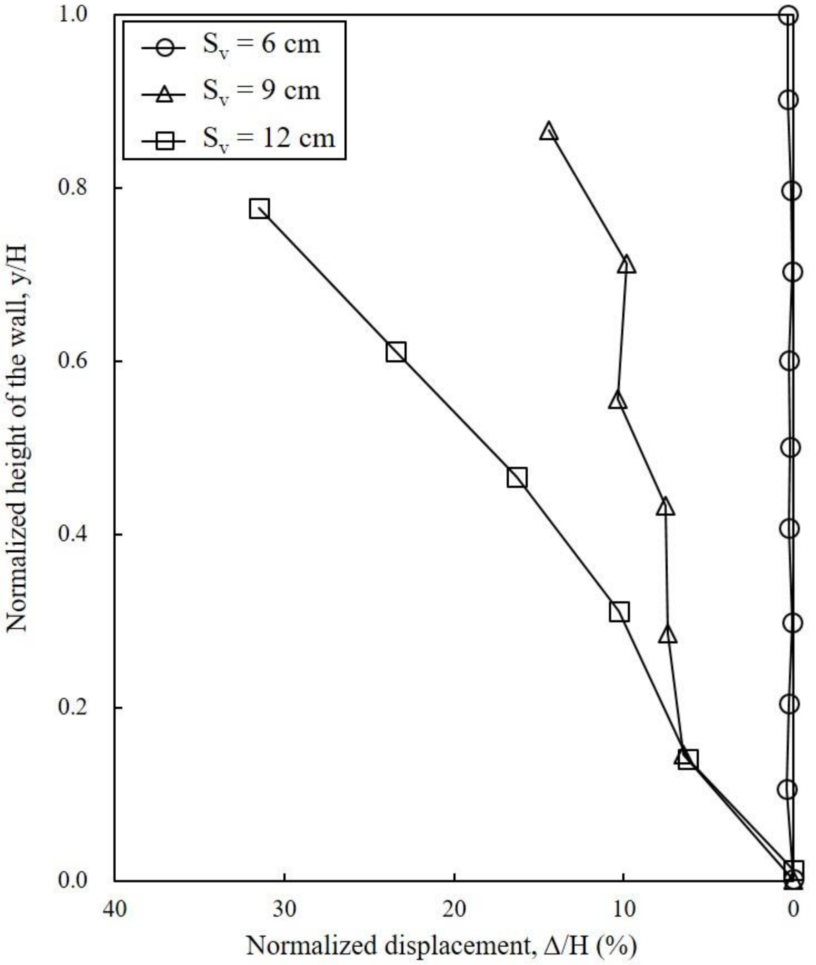

Figure 5.22 Wall displacement profile under different reinforcement spacing

Figure 5.23 displays the maximum wall displacement versus time. Aside from the reduction in the maximum wall displacement, the advancement of the wall displacement was more progressive as the reinforcement spacing was reduced. This can be attributed to the fact that lower earth pressure was distributed to a single reinforcement as the layers of reinforcement increased. Moreover, the development of the displacement had become more progressive as the reinforcement spacing decreased.

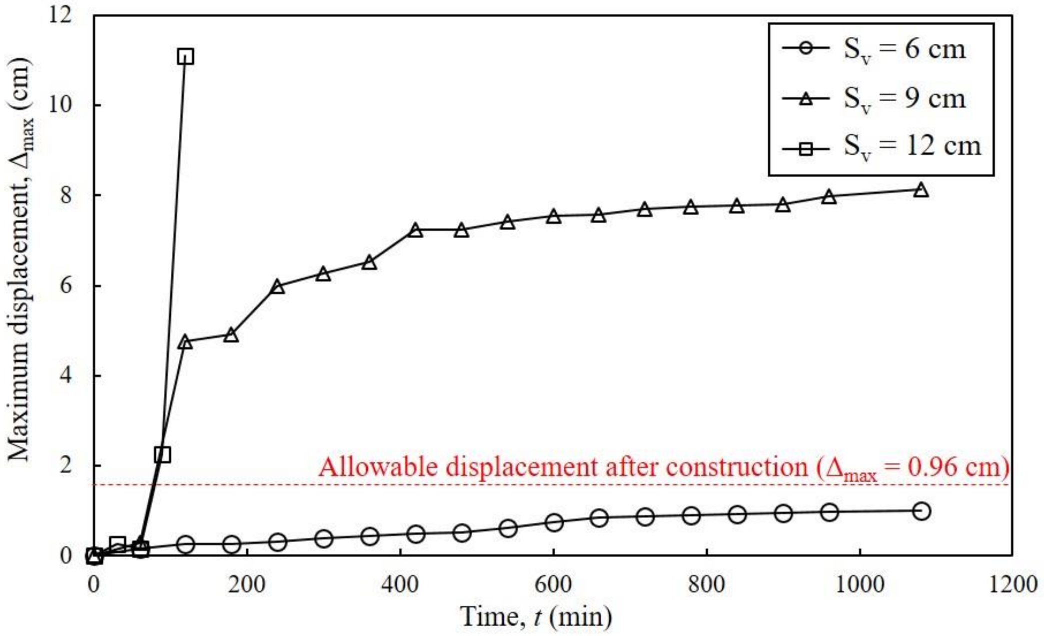

Figure 5.23 Maximum wall displacement versus time

doi:10.6342/NTU201901530

Figure 5.24 presents the maximum mobilized reinforcement tensile force profile. The figure suggests that the redution of the reinforcement spacing can effectively restrain the mobilized reinforcement tensile strain. When the reinforcement spacing was small, the mobilized reinforcement tensile strain was small and uniform. When reinforcement spacing was large, the reinforcement tensile strain was also large, especially at the top layers.

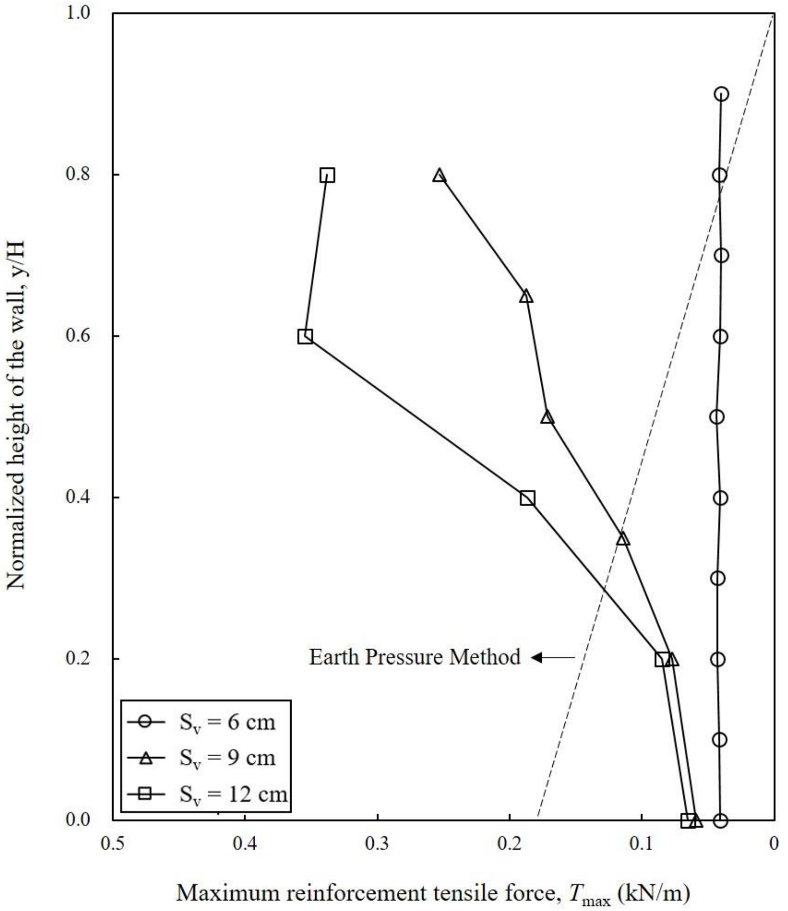

Figure 5.24 Maximum reinforcement tensile force profile

doi:10.6342/NTU201901530

Figure 5.25 indicates the corresponding *FS* with different maximum displacement and reinforcement tensile strain. The figure shows that the FS_{breakage} is very sensitive to the wall displacement. The *FS* significantly increases with the decrease of the maximum wall displacement. When the wall displacement is large (11 cm), $FS_{\text{breakage}} = 1.6$, only slightly larger than the required value ($FS_{\text{breakage}} = 1.5$). When FS_{breakage} was very large, the wall would only experience little displacement. Hence, this figure can serve as an indicator for GRS walls with marginal backfills under rainfall conditions. The designed *FS* should be increased 1.8 times under rainfall conditions in accordance with the allowable wall displacement.

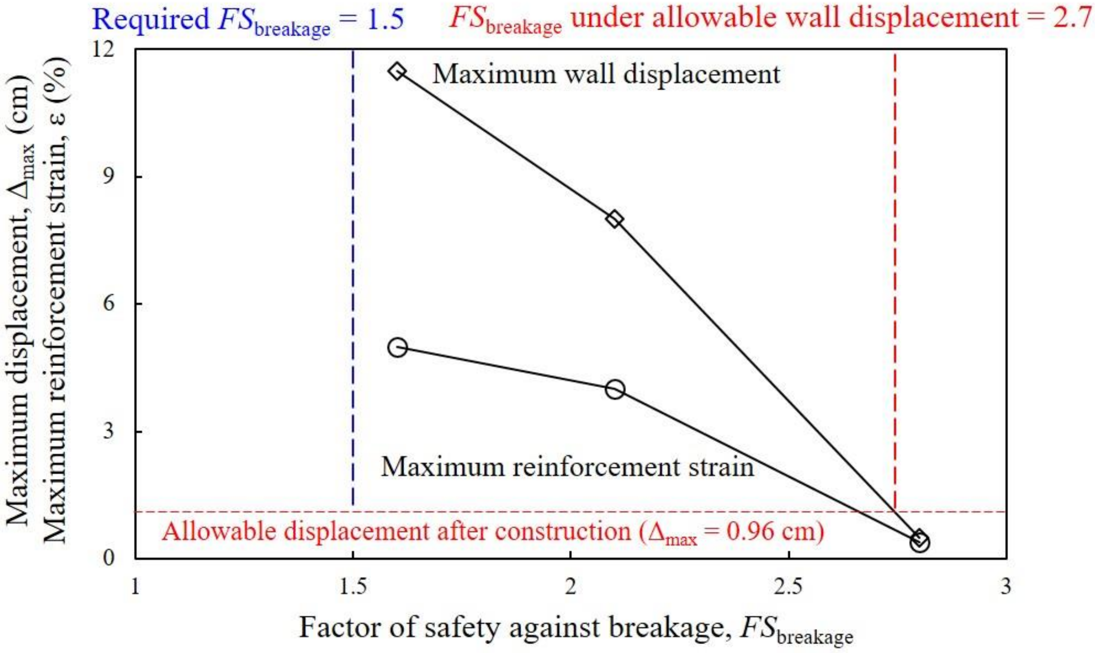

Figure 5.25 FS_{breakage} versus maximum displacement and reinforcement tensile strain

doi:10.6342/NTU201901530

In summary, the reduction of reinforcement spacing can effectively enhance the wall stability under rainfall conditions. Table 5.1 summarizes the performance of the test SM-S_v6, SM-S_v9, and SM-S_v12. The factor of safety increases with the decrease of reinforcement spacing and is much larger than the value specified by the regulations ($FS = 1.5$). The displacement can be significantly restrained by applying a small reinforcement spacing and the development of the wall displacement is more progressive. The mobilized reinforcement tensile strain was therefore smaller in the case with smaller spacing. The maximum strain mobilized in SM-Sv9 was 3% while only less than 1% strain was mobilized in SM-Sv6.

Table 5.1 Summary of test results

Test	SM-Sv6	SM-Sv9	SM-S_v12
FS_{breakage}	2.8	2.1	1.6
FS_{pullout} (dry)	3.6	3.6	2.7
FS_{pullout} (wet)	2.5	2.5	1.9
Maximum wall displacement, $\Delta_{\max}$ (cm)	0.5	8	11.5
Maximum reinforcement tensile strain, $\varepsilon_{\max}$ (%)	0.4	4	5
Tension cracks	N	Y	Y
Final stage	Stable	Excessive deformation	Collapsed
Failure mode	-	Progressive	Sudden

Chapter 6 Improved designs

This study proposed three improved methods for the design of GRS walls with marginal backfills. Aside from the reduction of the reinforcement spacing, the application of a better quality backfill and the adoption of the sand cushions to the reinforcement were proposed. A series of model tests was conducted to evaluate the effects of the improved methods and a comprehensive comparison is presented herein.

6.1 Influence of Backfill Quality

Two different backfill materials, sand (SP) and silty sand (SM), were used as the backfill materials to evaluate the influence of the backfill quality on the performance of GRS walls under rainfall conditions. The test results and a comprehensive discussion are provided in this section.

6.1.1 Test SP-S_v9 (Granular Backfill)

Figure 6.1 presents the photos of the model test SP-S_v9. Cracks appeared at $t = 50$ mins and thereafter no further significant deformation was observed. Notably, the location of the crack corresponds to where the reinforcement was embedded to form the wrap-around facing.

doi:10.6342/NTU201901530

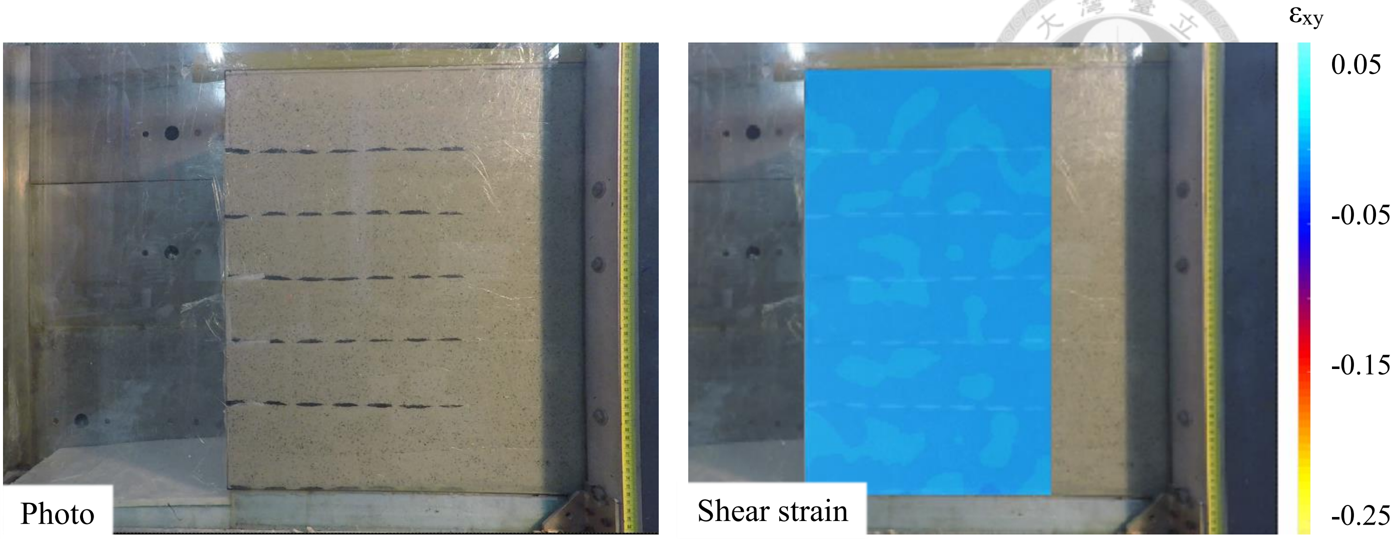

(a) ① Start of the test (t = 0 min)

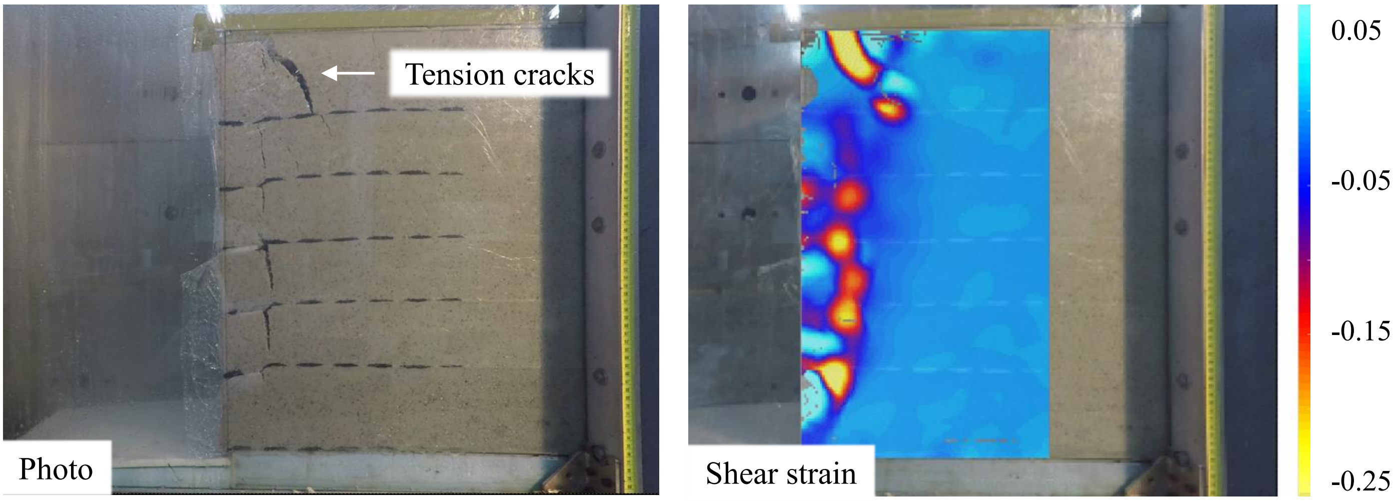

(b) ② Cracks developed (t = 50 mins)

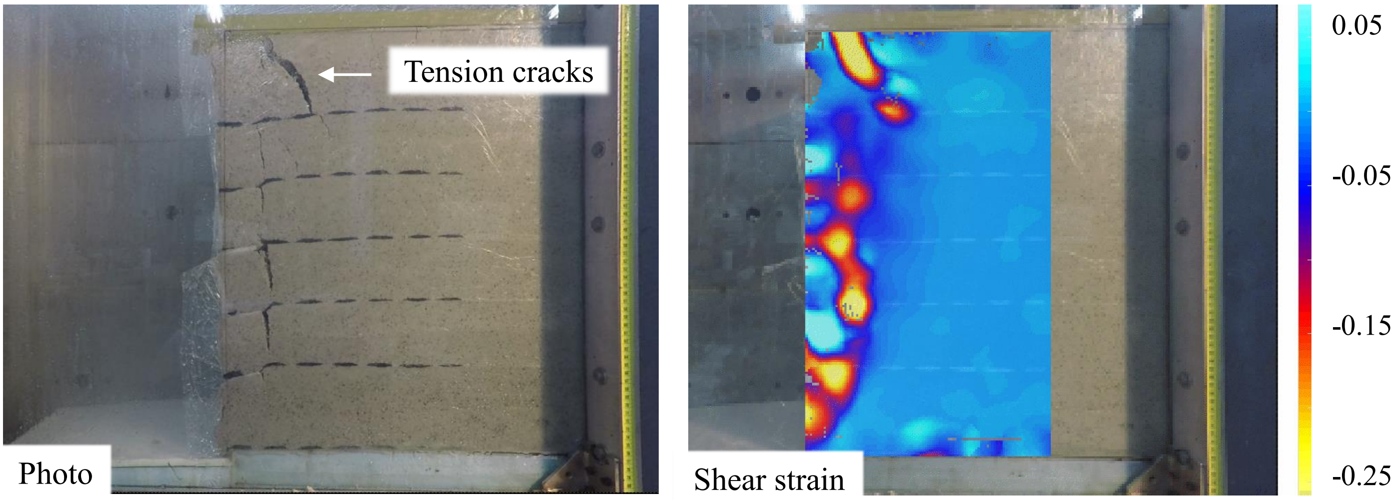

(c) ③ End of the test (t = 300 mins)

Figure 6.1 Pictures of the model test SP-S_v9

doi:10.6342/NTU201901530

Figure 6.2 presents the variation of the volumetric water content throughout the test. Water infiltrated from the top to the bottom as the increase of the VWC gauges initiated from VWC3, VWC3, to VWC1. Since the permeability of the backfill soil is much larger than the rainfall intensity, the water was able to flow to the bottom, making VWC1 the sensor that registered the highest water content.

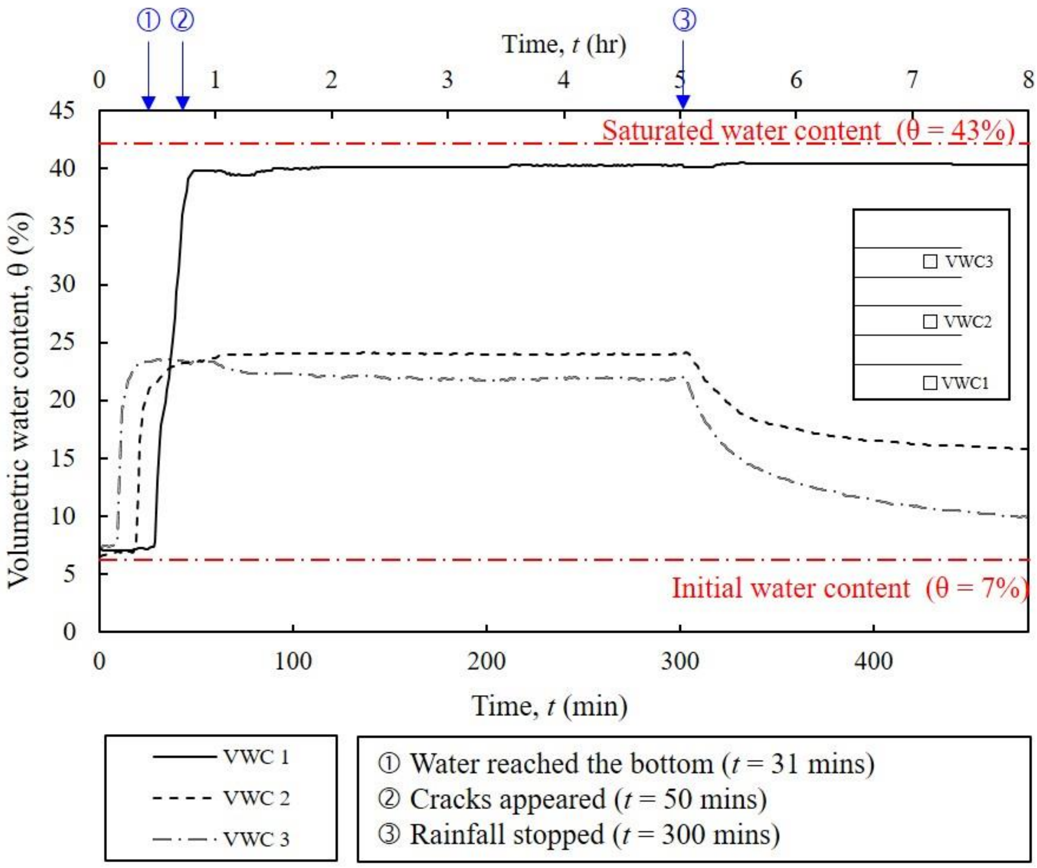

Figure 6.2 VWC with time elapse

Figure 6.3 shows the wall displacement profile throughout the test. The maximum displacement was around 6% of the wall height, which was much smaller than the displacement observed in the case SM-S_v9 (13% wall height). Contrary to the model wall with silty sand backfill, the model wall deformed more uniformly; large displacement was also found in the middle of the wall. The maximum difference between the displacement in each layer is less than 2%.

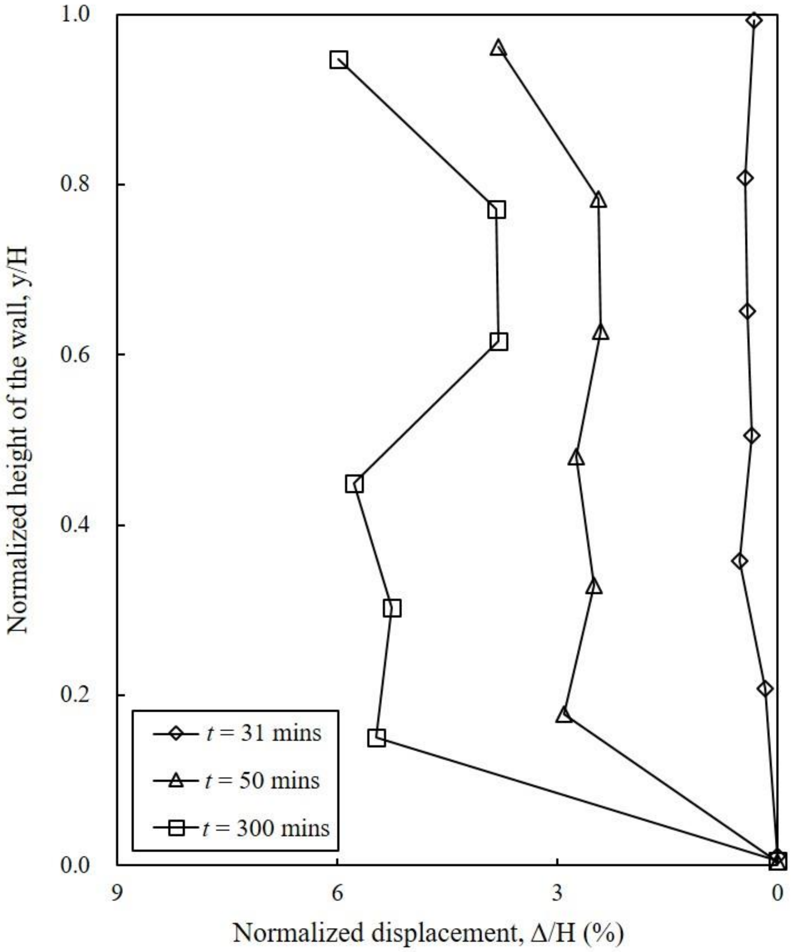

Figure 6.3 Wall displacement profile

doi:10.6342/NTU201901530

Figure 6.4 presents the development of the maximum wall displacement and settlement. The development of the wall displacement is significantly different between reinforced walls with marginal backfill and granular backfill. For reinforced wall with granular backfill (SP-S_v9), the tension cracks developed suddenly at t = 50 mins. The major deformation was induced by the sudden development of the cracks. The reinforced wall of the test SP-S_v9 soon reached the equilibrium state at t = 150 mins. Settlement commenced suddenly upon the development of the cracks, resembling the development of wall displacement.

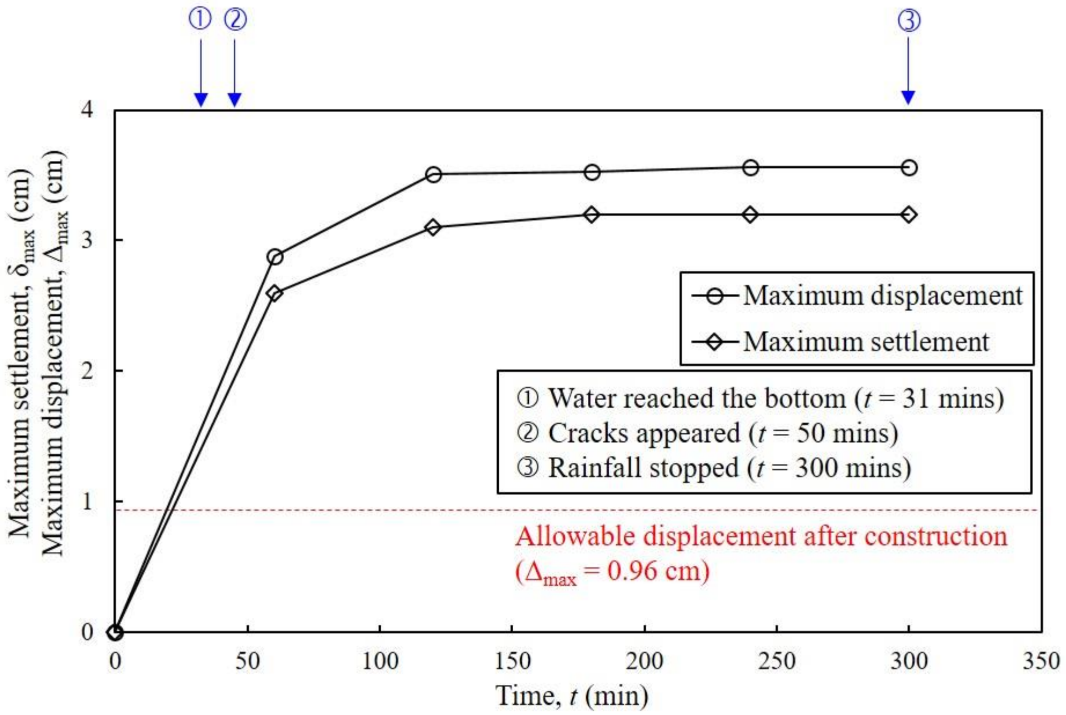

① Water reached the bottom (t = 31 mins)
② Cracks appeared (t = 50 mins)
③ Rainfall stopped (t = 300 mins)

Allowable displacement after construction
(Δ_{max} = 0.96 cm)

Figure 6.4 Maximum wall displacement and settlement versus time

Figure 6.5 shows the mobilized reinforcement strain in each layer. The wall displacement was small; the mobilized reinforcement strain was therefore small, with a maximum value less than 2%. The potential sliding surface can be obtained by connecting the locus of the maximum reinforcement strain in each layer. The potential sliding surface observed by visual inspection and the PIV analysis were also plotted. The three potential sliding surfaces acquired from visual observation, locus of maximum tensile strain, and intensive strain contour were consistent. Moreover, the strain contour shown in Figure 6.5 had a maximum value of 36% strain, which is far beyond the soil peak strain according to the triaxial tests. The soil indeed failed along the maximum strain band detected from the PIV analysis as the visual inspection verified so.

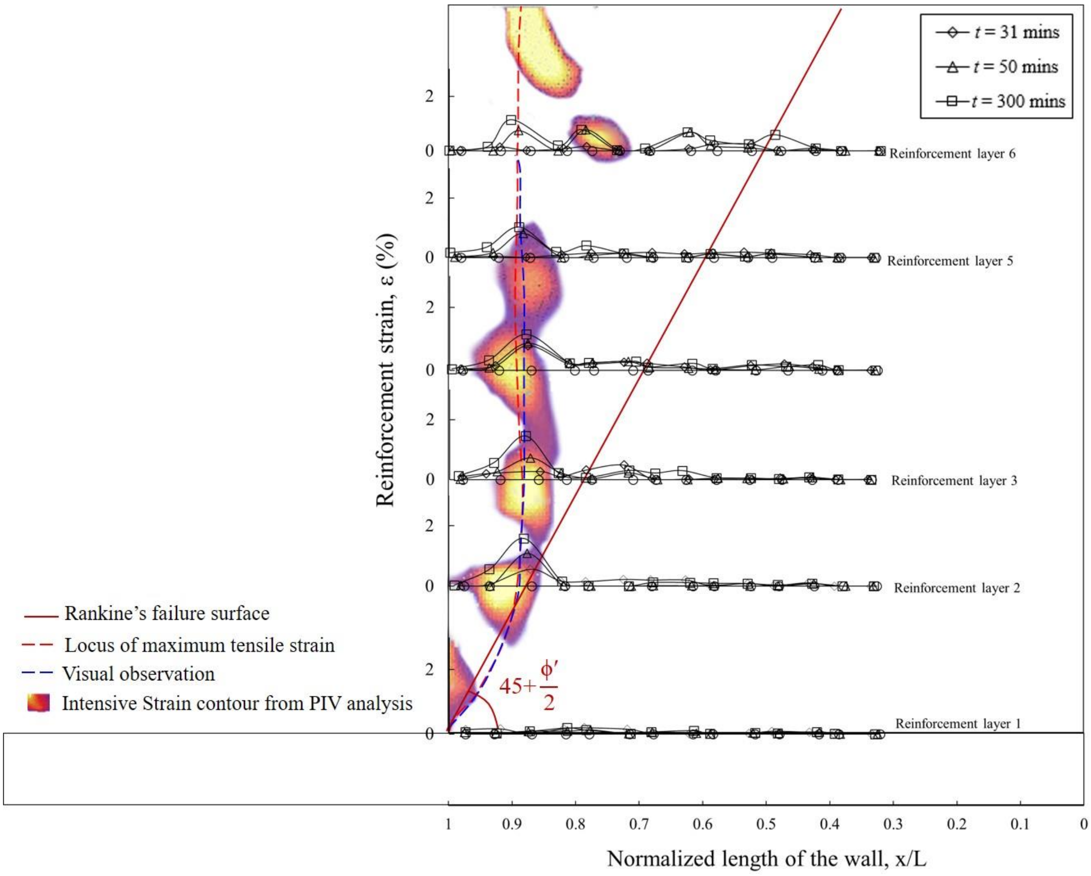

Figure 6.5 Reinforcement tensile strain and comparison of potential sliding surface

doi:10.6342/NTU201901530

Figure 6.6 shows the mobilized maximum reinforcement tensile force profile. In the test SP-S_v9, the mobilized reinforcement tensile strain displayed a uniform profile. The tensile strain at the top layers was slightly larger than that estimated from the earth pressure method while the tensile strain at the bottom layers was smaller than the value calculated from the earth pressure method.

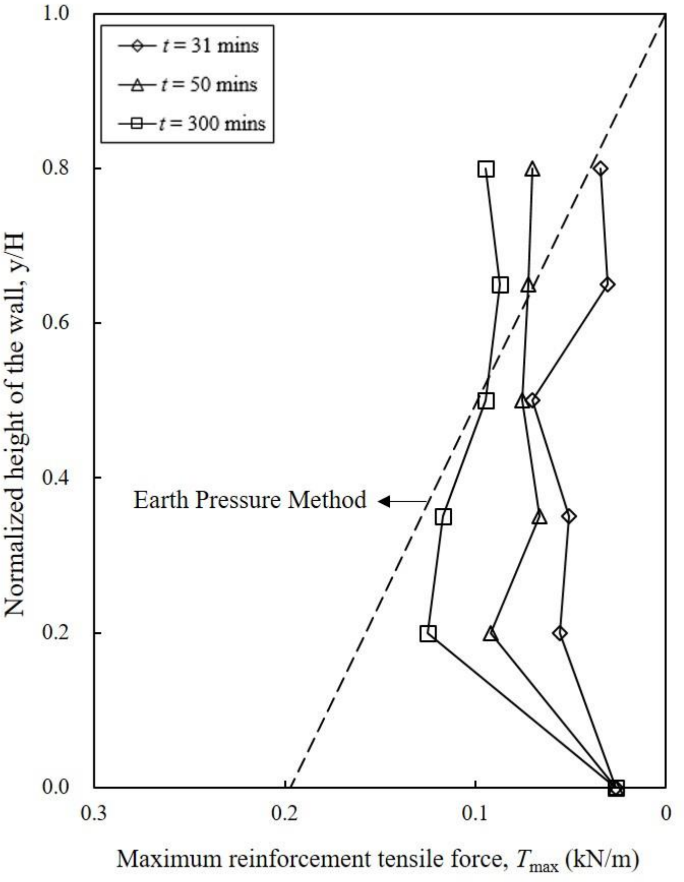

Figure 6.6 Maximum reinforcement tensile force profile

In summary, the failure mode is determined as surficial shallow failure vertically along the end of the secondary reinforcement (i.e., the location of the wrapped-around portion). Major displacement occurred suddenly as the tension cracks developed and the potential sliding surface propagated through all the layer. Soon after the wall reached steady state.

doi:10.6342/NTU201901530

6.1.2 Comparison

The effect of applying a better quality backfill was investigated. Table 6.1 summarizes the factor of safety against breakage and pullout failure, and Figure 6.7 presents the pictures of the two model tests. The factor of safety against pullout was significantly larger in the case with granular backfill owing to the high friction angle and soil-geogrid interface friction.

Table 6.1 Factor of safety

Model test	FS_{breakage}	FS_{pullout} (dry)	FS_{pullout} (wet)
SM-S_v9	2.1	3.6	2.5
SP-S_v9	2.4	6.5	6.4

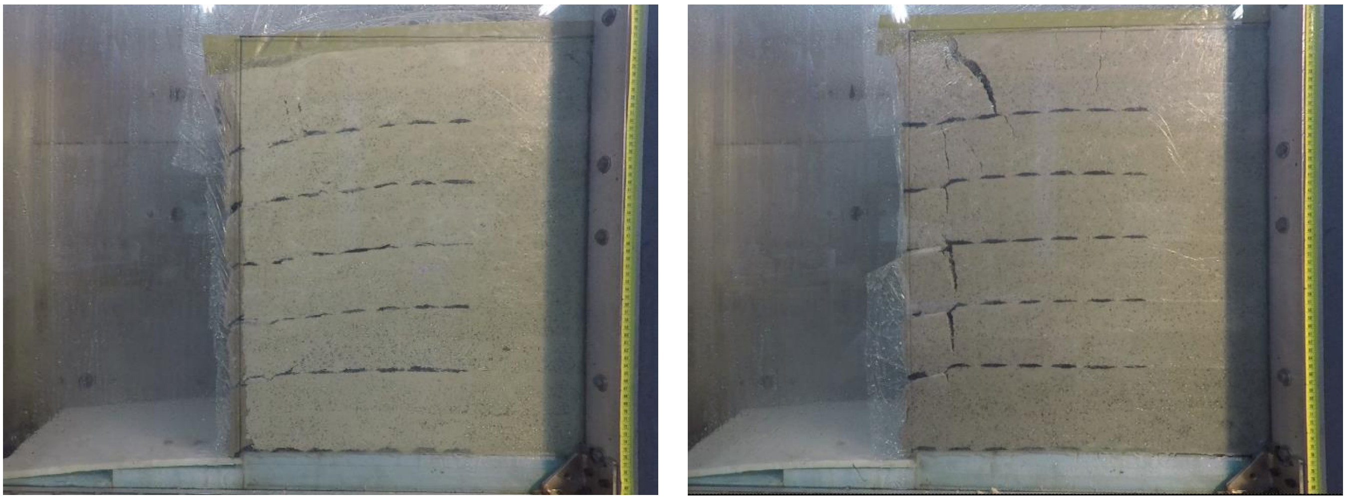
(a) (b)

Figure 6.7 Pictures of the tests: (a) SM-S_v9; (b) SP-S_v9

doi:10.6342/NTU201901530

Figure 6.8 displays the wall displacement profile in the two cases, and Figure 6.9 demonstrates the maximum wall displacement versus time. For the same spacing (S_v = 9 cm), the reinforced wall with granular backfill displayed a smaller displacement of 6% wall height in maximum. Contrarily, marginal backfilled GRS wall demonstrated larger wall displacement up to 14% wall height. The application of a better quality backfill can reduce up to 50% of the maximum wall displacement. Moreover, the maximum wall displacement of the wall with marginal backfill occurred at the top and decreased with elevation whereas the wall displacement showed a more uniform profile in the wall with granular backfill. This can be attributed to the high water retention characteristic in marginal backfill; the water was confined at the top layers and caused displacement. In addition, the wall displacement was progressive in the case SM-S_v9, which was issued from the gradual loss of matric suction and soil shear strength upon the infiltration of rainfall. Conversely, tension cracks developed suddenly in granular backfilled wall without cohesion, and no further significant displacement was observed afterward.

doi:10.6342/NTU201901530

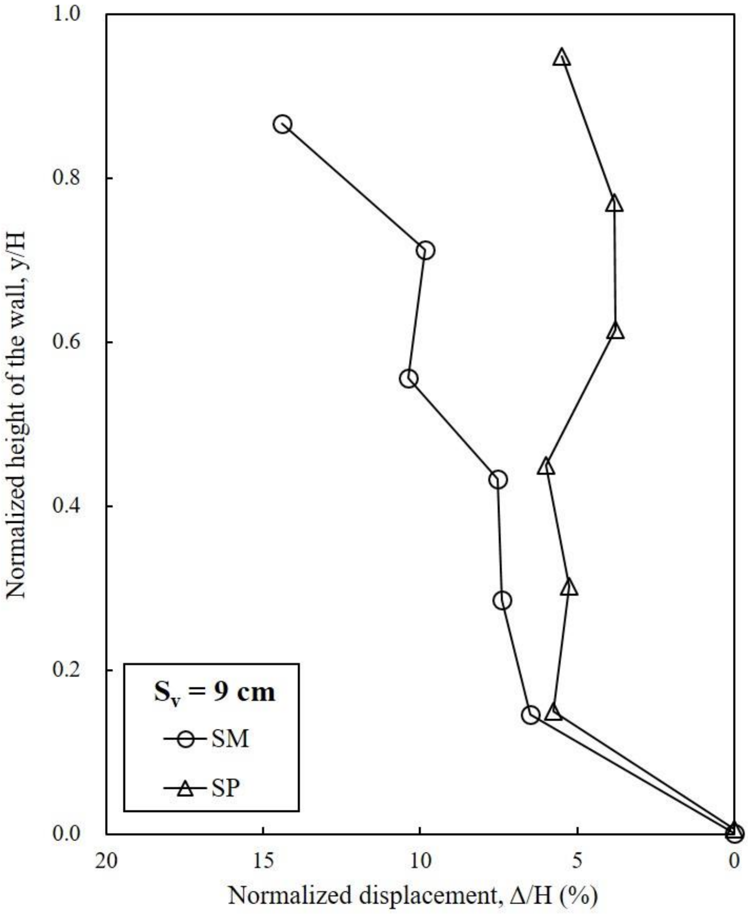

Figure 6.8 Wall displacement profile

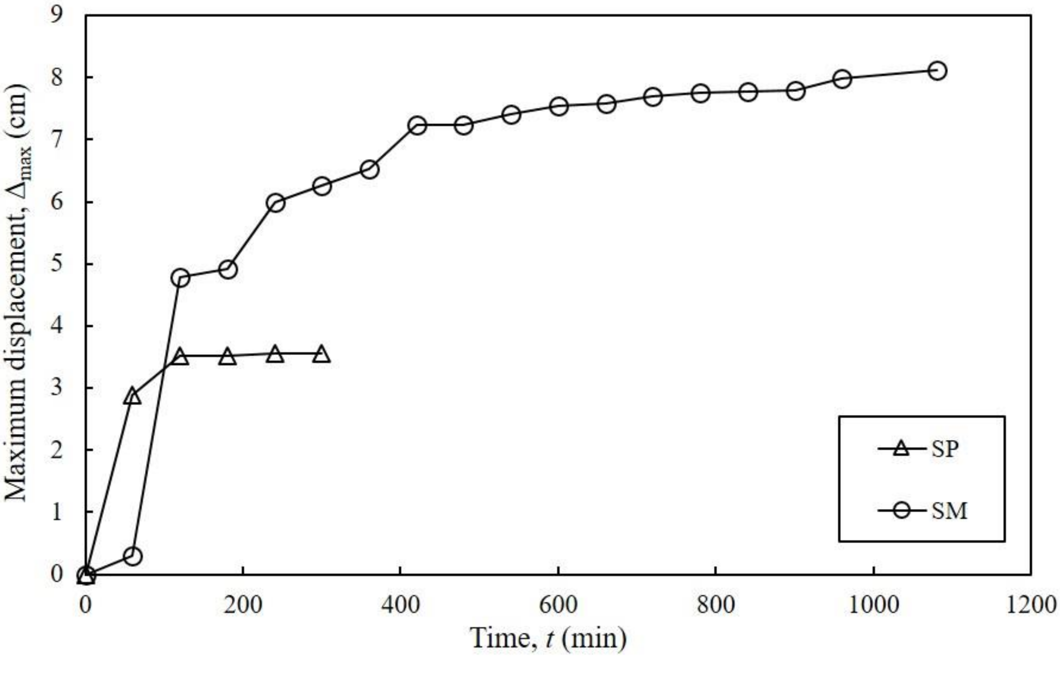

Figure 6.9 Maximum wall displacement versus time

doi:10.6342/NTU201901530

Figure 6.10 presents the mobilized tensile strain in the two cases. With larger wall displacement, SM-S_v9 had larger reinforcement tensile strain than SP-S_v9, especially in the top layers. Notably, in reinforcement layer 2, the mobilized reinforcement tensile strain in the tests SM-S_v9 was smaller than that in the test SP-S_v9. This can be attributed to different wall displacement profile. Maximum displacement was observed to be at the top in SM-S_v9 whereas the wall displacement along each layer are similar in SP-S_v9. The maximum strain mobilized in the test SM-S_v9 was around 4%, whereas the maximum strain mobilized in the test SP-S_v9 was 1.5%. Notably, as the elevation decreased, the tensile strain in SM-S_v9 decreased. Nevertheless, the tensile strain remained a similar value in each layer for the case SP-S_v9 because the tension cracks developed through all the layers and the displacement in each layer was similar.

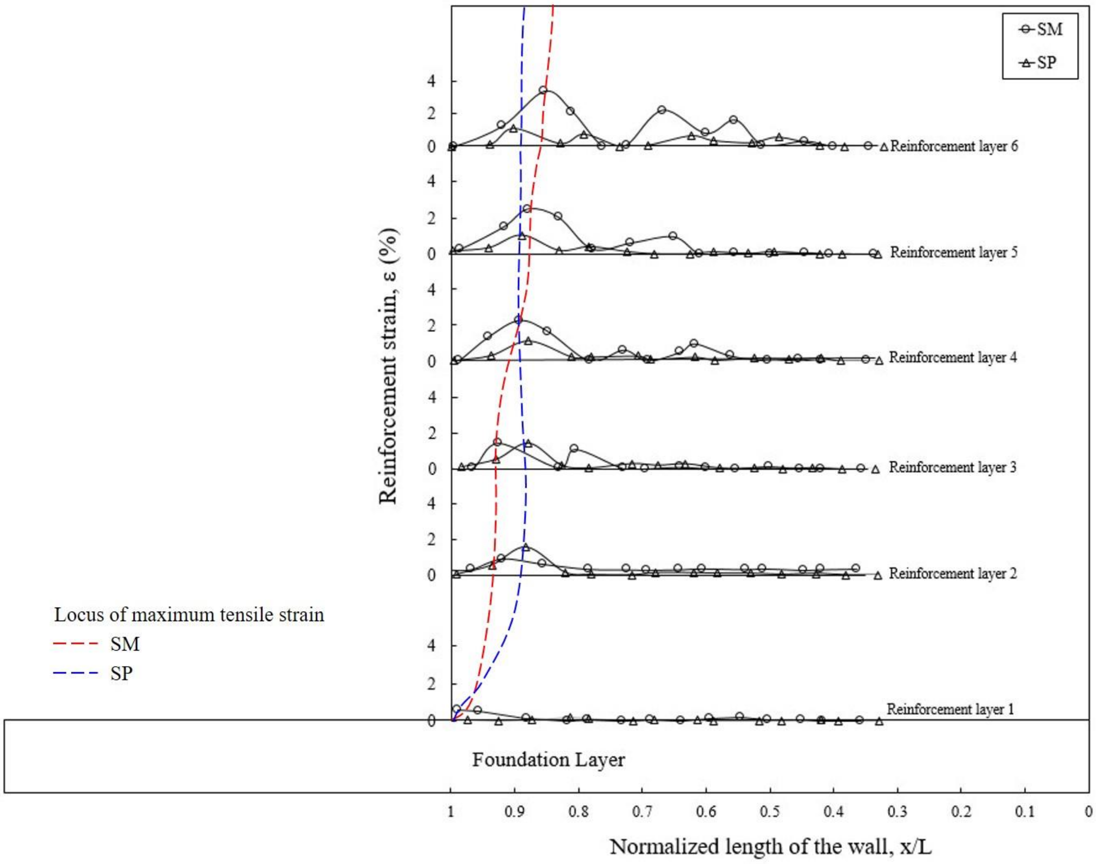

Figure 6.10 Reinforcement tensile strain

Figure 6.11 displays the maximum reinforcement tensile force profile. The mobilized reinforcement tensile force resembled the same pattern as the wall displacement. In the test SM-S_v9 (baseline case), the tensile force was largest at the top, forming a cantilever type. In the test SP-S_v9, the tensile force mobilized in each layer remain similar values since the wall displacement was uniform. The tensile force mobilized in the test SP-S_v9 was mostly within the allowable values estimated from the earth pressure method. Both pattern did not correspond to the values calculated from Rankine's earth pressure method.

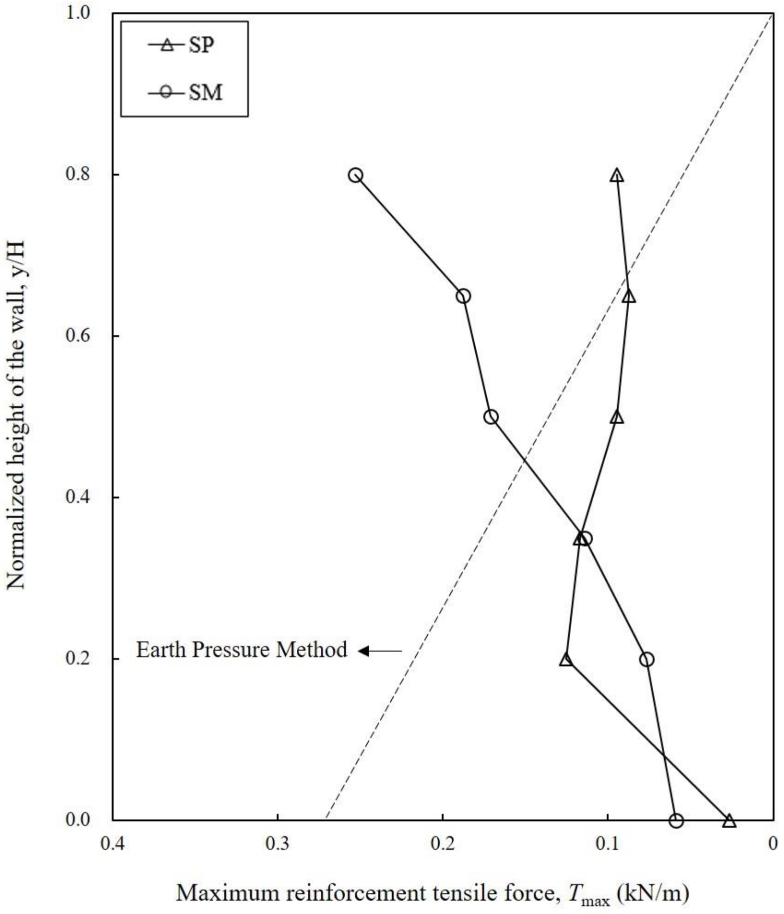

Figure 6.11 Maximum reinforcement tensile force profile

doi:10.6342/NTU201901530

The observed wall displacement was in great agreement with Figure 6.12, in which the strain contour from PIV analysis was illustrated. The maximum strain contour in SM-S_v9 occurred at the top layers where the maximum displacement commenced, and the strain dissipated with the decrease of the elevation. For SP-S_v9, however, the maximum strain contour propagated through all the layers, which coincided with visual observation.

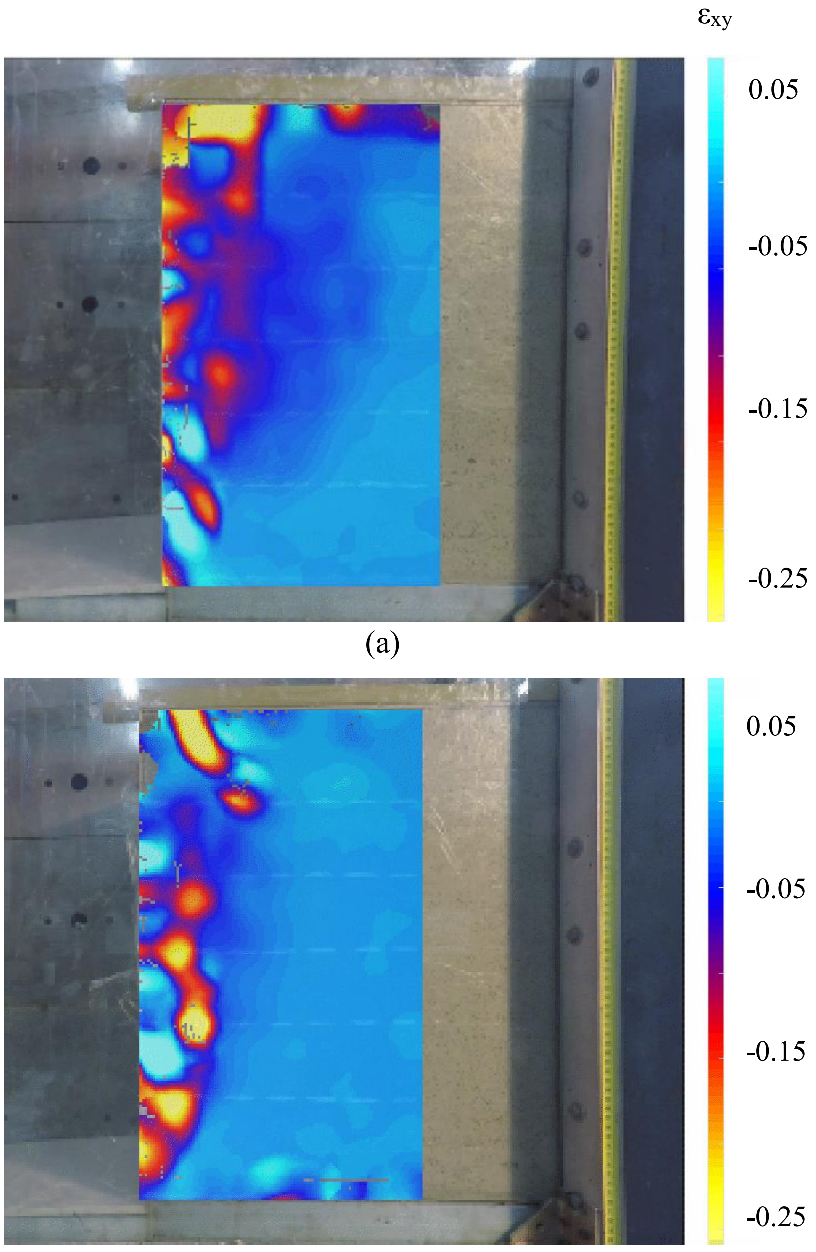

(a)

(b)

Figure 6.12 Strain contour from PIV analysis: (a) SM-S_v9; (b) SP-S_v9

In summary, the application of granular backfill can effectively enhance the soil-geogrid interface friction, which is critical to the performance of the reinforced wall under rainfall conditions. Table 6.2 summarized the performance of the tests SM-S_v9 and SP-S_v9. The failure modes in the tests SM-S_v9 and SM-S_v9 were different. In the test SP-S_v9, though the wall was fully wet, the saturated region was confined within the lowest layers on account of the high hydraulic conductivity of the backfill material. The appearances of the tension cracks and the potential failure surface was sudden occurrence and the intensive strain propagated through all layer. On the contrary, in the test SM-S_v9, the infiltrated water was accumulated on the top layer, causing loss of matric suction and further inducing tension cracks. The development of the wall displacement was progressive.

Table 6.2 Summary of test results

Test	SM-Sv9	SP-Sv9
FS_{breakage}	2.1	2.4
FS_{pullout} (dry)	3.6	6.5
FS_{pullout} (wet)	2.5	6.4
Maximum wall displacement, $\Delta_{\max}$ (cm)	8	3.5
Maximum reinforcement tensile strain, $\varepsilon_{\max}$ (%)	4	1.5
Tension cracks	Y	Y
Final stage	Excessive displacement	Minor deformation
Failure mode	Progressive	Sudden

6.2 Effects of Sand Cushions

6.2.1 Test SM-S$_v$9-C4 (Adoption of Sand Cushions)

Figure 6.13 presents the photos of the test results of the test SM-S$_v$9-C4. In this test, sand cushion thickness of 4 cm (replacing 36% of the marginal backfill with sand) for each reinforcement layer was applied. Tension cracks were found to start developing at 82 mins after the test started and eventually propagated to form the potential sliding surface. Afterward, no significant displacement occurred until a slight movement observed from *t* = 420 mins to *t* = 480 mins.

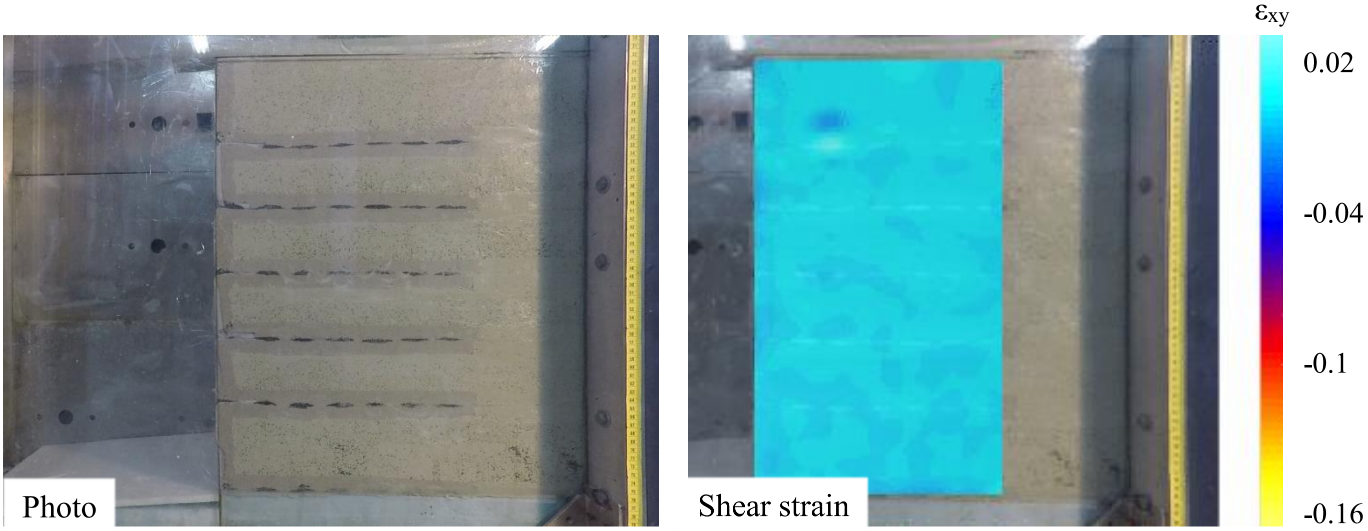

(a) ① Start of the test (*t* = 0 min)

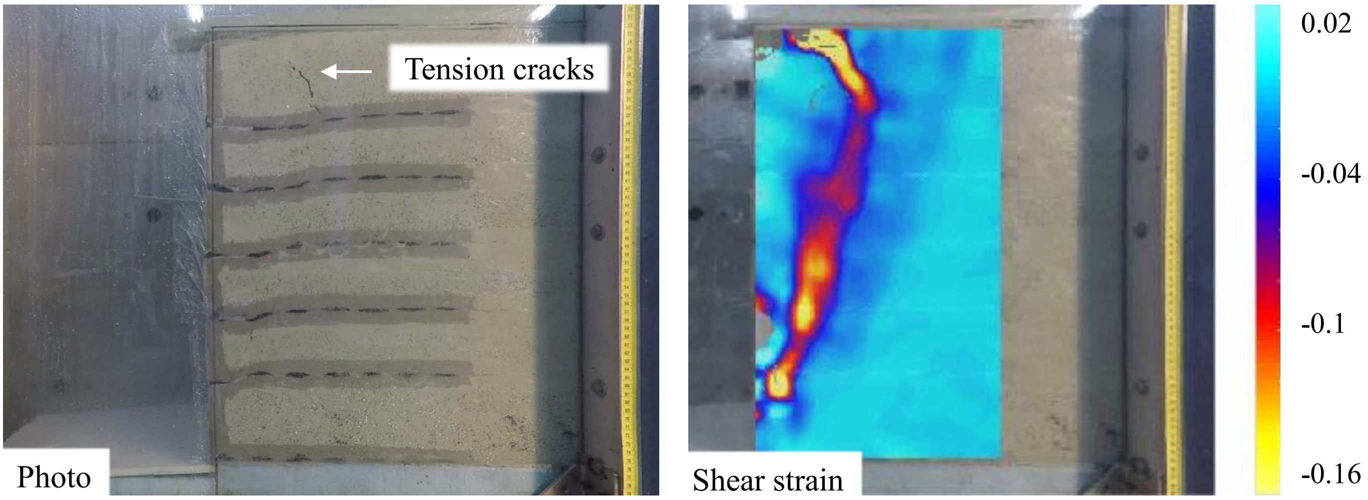

(b) ② Tension cracks and potential failure surface appeared (*t* = 82 mins)

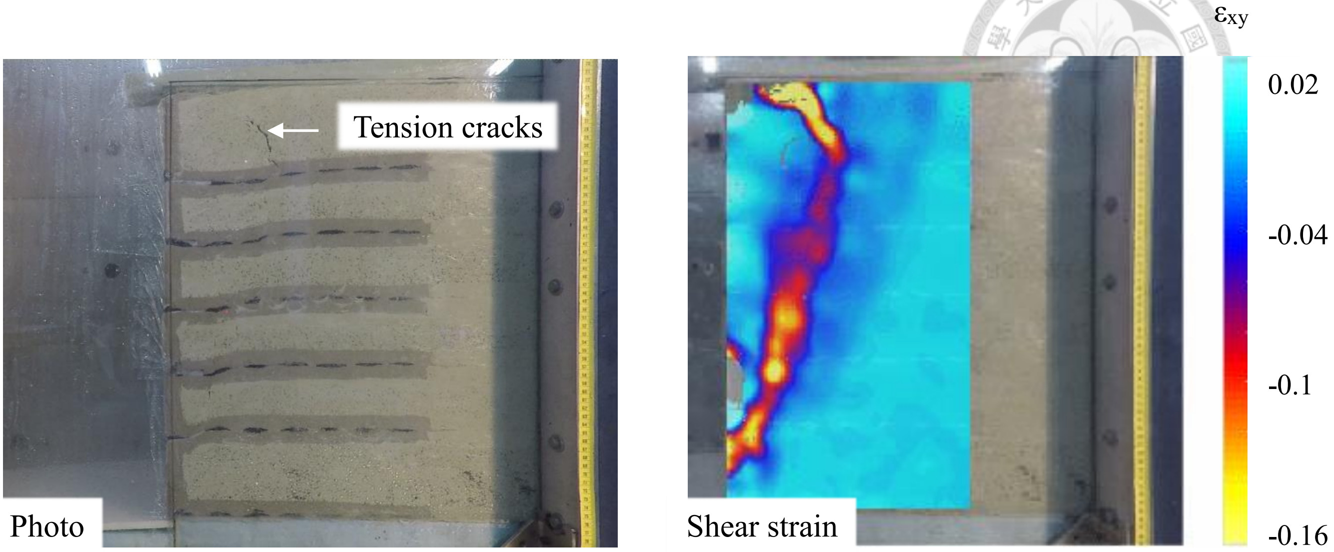

(c) ③ Water reached the bottom (*t* = 100 mins)

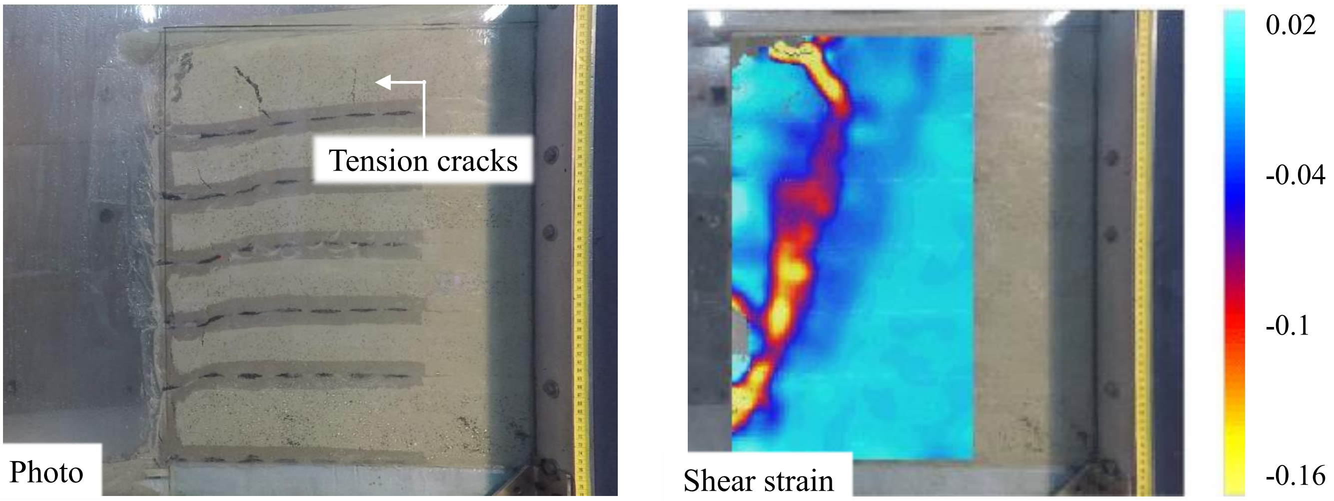

(d) ④ Displacement reached steady state (*t* = 660 mins)

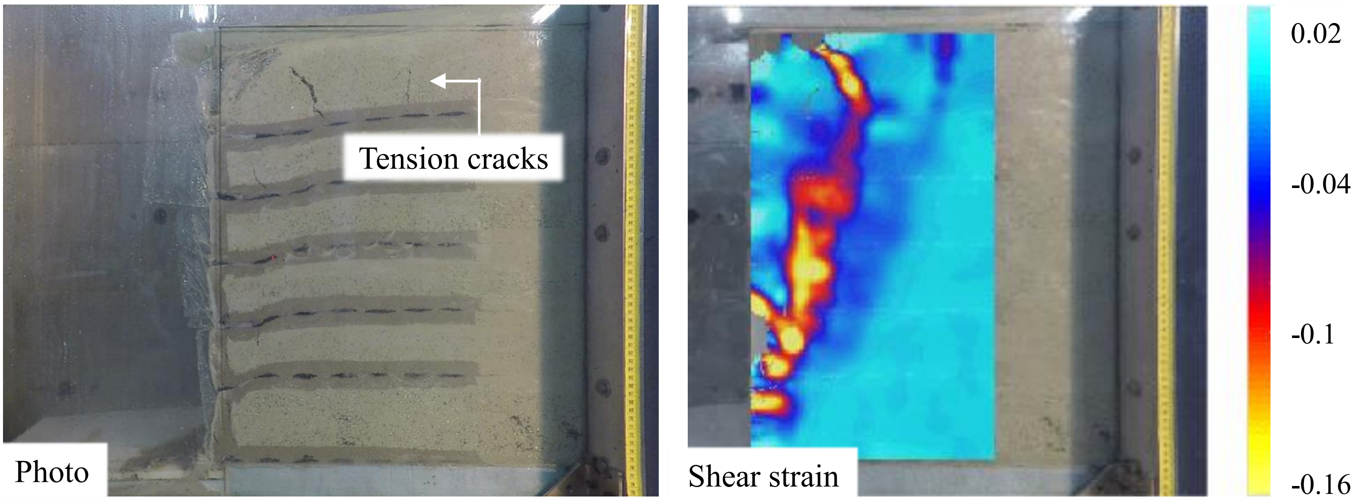

(e) ⑤ End of the test (*t* = 1080 mins)

Figure 6.13 Pictures of the model test SM-S_v9-C4

doi:10.6342/NTU201901530

Figure 6.14 presents the variation of the volumetric water content with time. VWC3, 2, and 1 showed an increase in succession as the water flowed from the top to the bottom. Notably, VWC1, locating at the bottom of the wall, registered the highest θ; this can be attributed to the high permeability of the sand cushions. The water flowed down from the filter layer and seeped into the reinforced wall through each sand cushion layer.

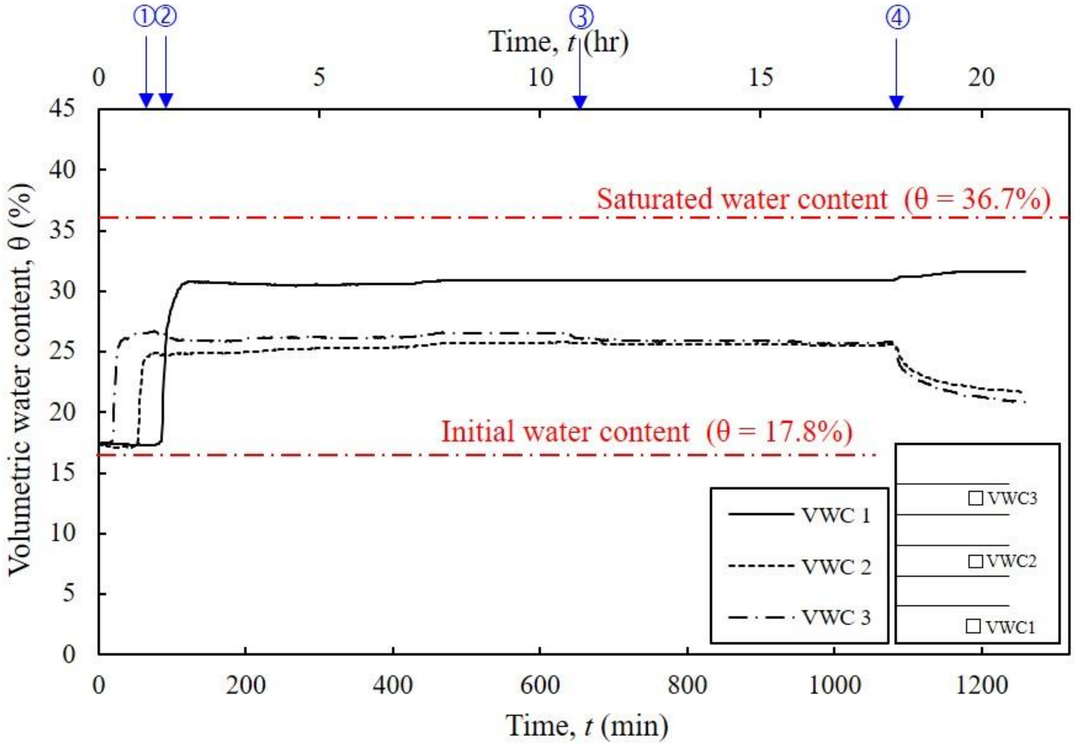

① Tension crack and potential failure surface appeared (t = 82 mins)
② Water reached the bottom (t = 100 mins)
③ Displacement reached steady state (t = 660 mins)
④ Rainfall stopped (t = 1080 mins)

Figure 6.14 VWC with time elapse

doi:10.6342/NTU201901530

Figure 6.15 shows the wall displacement profile. Before water reached the bottom of the wall (t = 100 mins), tension cracks and potential failure surface had appeared (t = 82 mins). The maximum wall displacement at the end of the test was 8% of the wall height and it occurred at the topmost layer, similar to the test SM-S_v9 (without sand cushions). Notably, the wall displacement had turned into a more uniform deformation along the wall face compared with the model test without adopting sand cushions. With the adoption of sand cushions, the difference between the wall displacement was 2%, whereas a difference of 8% was observed in such case without sand cushions.

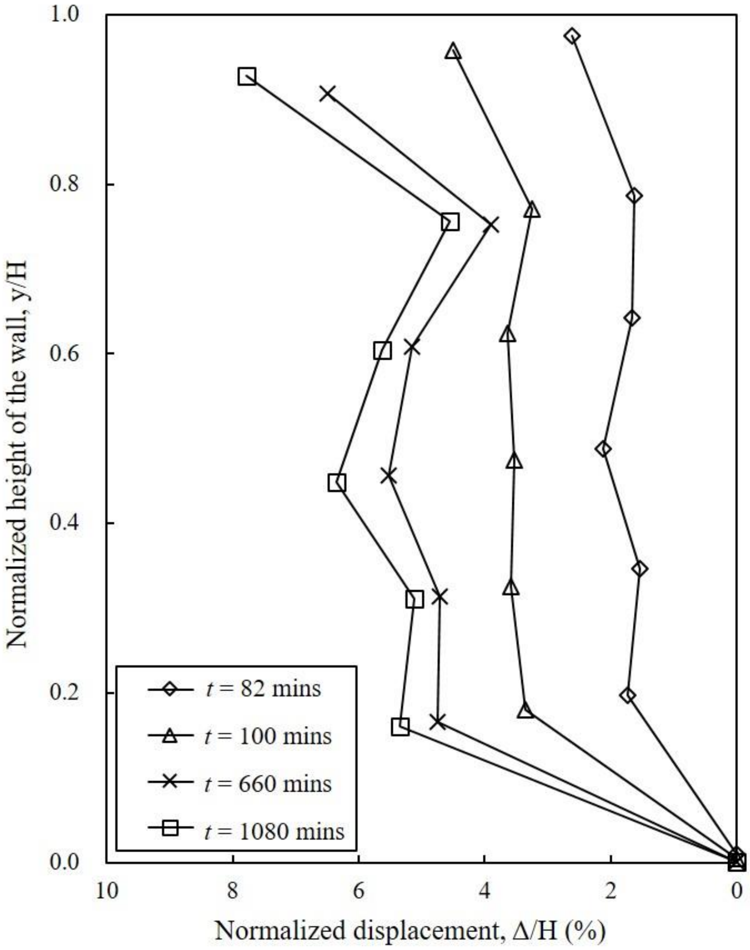

Figure 6.15 Wall displacement profile

doi:10.6342/NTU201901530

Figure 6.16 presents the maximum wall displacement and settlement versus time. The figure suggests that there were two major displacements, at *t* = 60~120 mins and at *t* = 540~600mins. The first corresponded to the development of the tension cracks, resulted from the loss of matric suction and soil shear strength due to rainfall infiltration. The second issued from the development of the soil shear strain. The soil eventually exceeded its failure strain; therefore, the second wall displacement commenced. Next, the wall displacement reached steady state at *t* = 660 mins.

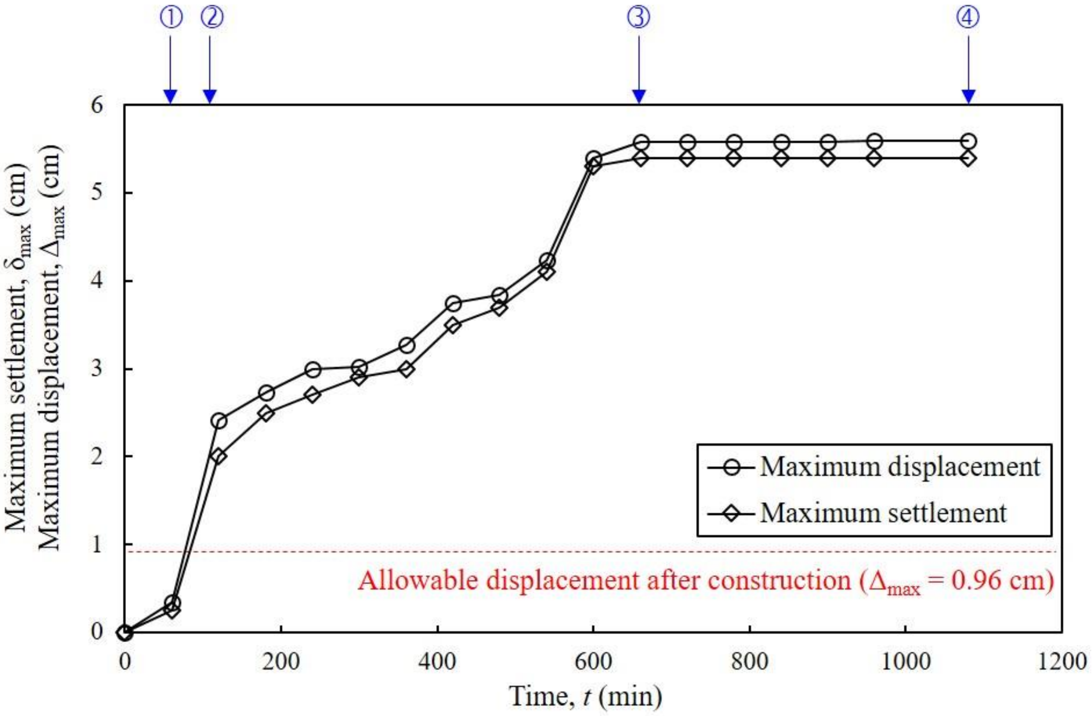

① Tension crack and potential failure surface appeared (*t* = 82 mins)
② Water reached the bottom (*t* = 100 mins)
③ Displacement reached steady state (*t* = 660 mins)
④ Rainfall stopped (*t* = 1080 mins)

Figure 6.16 Maximum wall displacement and settlement versus time

Figure 6.17 shows the mobilized reinforcement tensile strain. The maximum tensile strain was less than 3% and was located at the topmost layer. The displacement-induced maximum tensile strain in each layer decreased from the crest to the bottommost layer, which corresponded to the wall displacement from visual observation. Moreover, a potential sliding surface was shown as the red dashed line by connecting the locus of the maximum tensile strain in each layer. The failure surface by visual inspection and the maximum strain contour from the PIV results were also presented; the three were found to coincide. The maximum strain analyzed by the PIV analysis was around 26%, which was beyond the failure strain for the marginal backfill and meanwhile exceeded the peak strain of the sand.

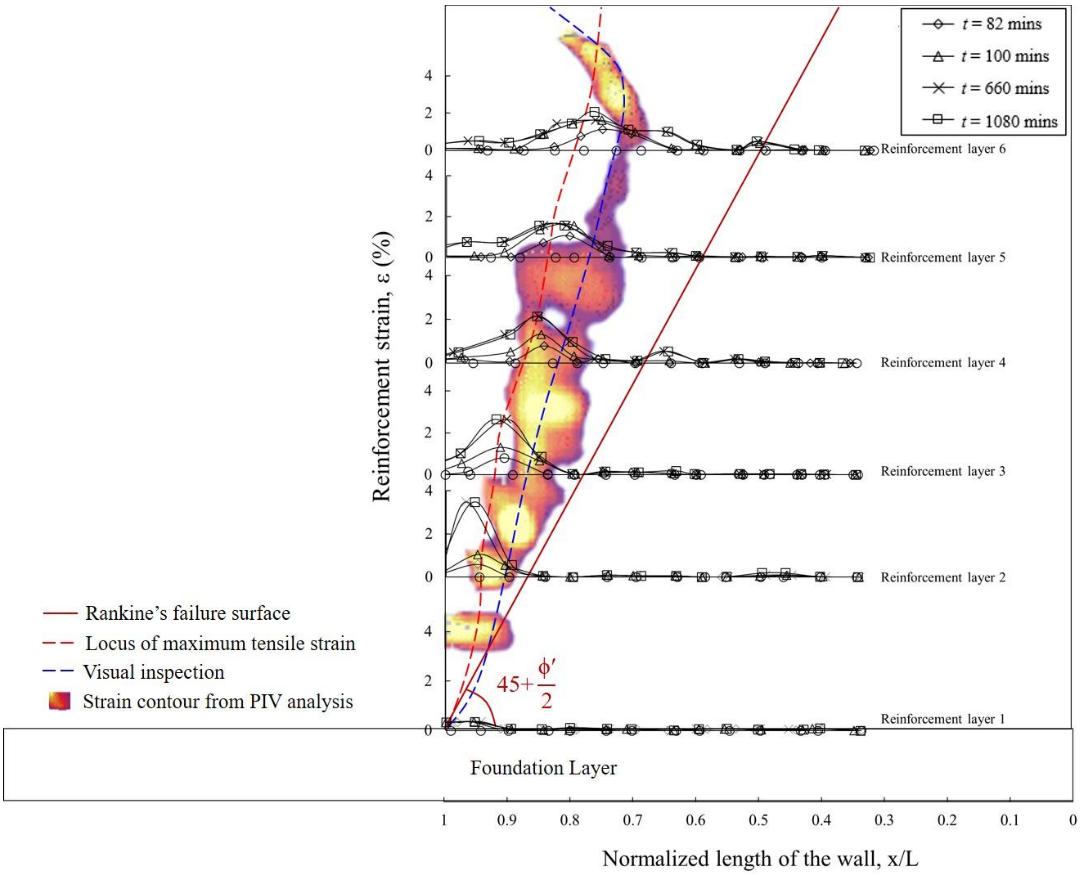

Figure 6.17 Reinforcement tensile strain and comparison of potential sliding surface

doi:10.6342/NTU201901530

Figure 6.18 displays the maximum reinforcement tensile force profile. At *t* = 1080 mins when the rainfall stopped, the mobilized reinforcement tensile strain in each layer was larger than the values suggested by the earth pressure method. Moreover, the pattern was changed from a cantilever type to a more uniform type.

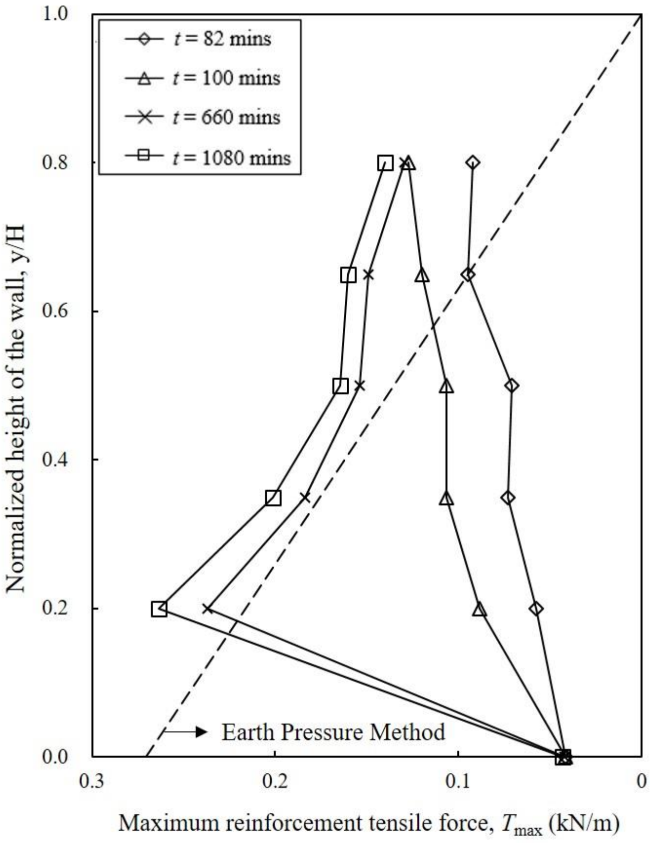

Figure 6.18 Maximum reinforcement tensile force profile

In summary, the soil-geogrid interface friction was enhanced in the test SM-S_v9-C4 because of the adoption of sand cushions. The high friction between the sand cushions and the geogrid reinforcement effectively restrained the excess deformation. The failure mode, however, developed into a compound of sudden tension cracks and progressive deformation. Not only was the wall displacement reduced, but the time the displacement reached the maximum was postponed. Tension cracks were found because of the high volumetric water content confined in the marginal backfill. Moreover, the developed soil shear strain in the test SP-S_v9 was significantly smaller than the test SM-S_v9.

6.2.2 Comparison

Table 6.3 summarizes the factor of safety against breakage and pullout for the tests SM-S_v9 and SM-S_v9-C4, and Figure 6.19 presents the pictures at the end of the two tests. The thickness of the sand cushions was 4 cm, accounting for 36% of the backfill. The factor of safety against pullout was significantly larger in the test SM-S_v9-C4 because of the high interface shearing characteristic between sand-geogrid interface. Visual observation indicates that larger deformation occurred in the test SM-S_v9 while only minor displacement was observed in the test SM-S_v9-C4.

Table 6.3 Factor of safety

Model test	FS_{breakage}	FS_{pullout} (dry)	FS_{pullout} (wet)
SM-S_v9	2.1	3.6	2.5
SM-S_v9-C4	2.1	4.4	4.3

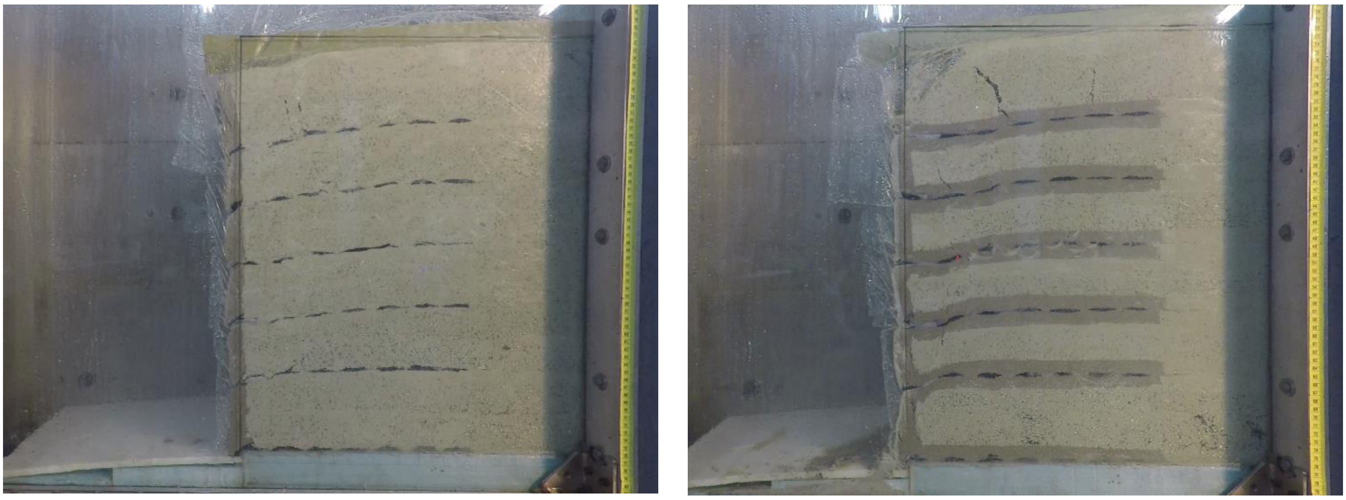
(a) (b)

Figure 6.19 Pictures of tests: (a) SM-S_v9; (b) SM-S_v9-C4

Figure 6.20 displays the wall displacement profile with and without the adoption of sand cushions. Visual inspection indicated that the wall displacement was smaller in the case with sand cushion applied. The maximum wall displacement in the test SM-S_v9 was observed at the topmost layer, with a value of 15% wall height. After the adoption of sand cushions, the maximum wall displacement was reduced to 8% wall height. For $S_v = 9$ cm, the wall displacement was reduced by 40% after adopting sand cushions.

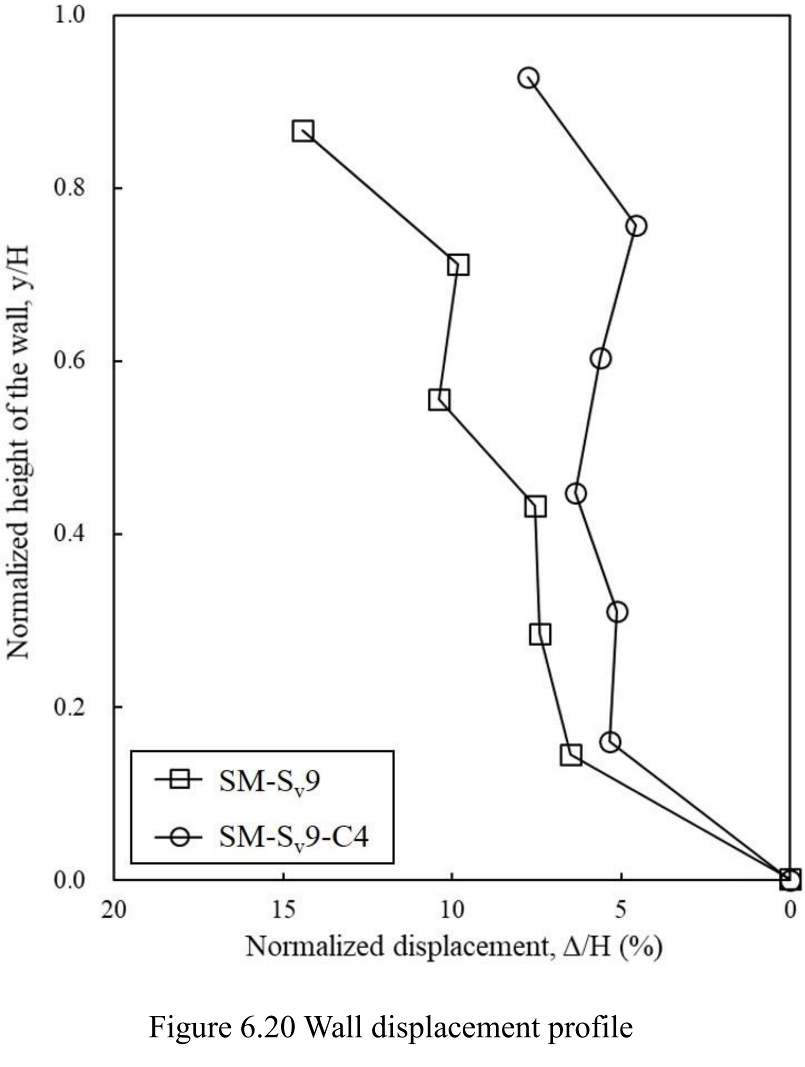

Figure 6.20 Wall displacement profile

doi:10.6342/NTU201901530

Figure 6.21 demonstrates the maximum displacement versus time. The maximum displacement was 8 cm in the test SM-S_v9; however, after the adoption of sand cushions, the maximum displacement was reduced to 5 cm in the test SM-S_v9-C4. Aside from the reduction in the maximum wall displacement, the progression of the displacement had become gentler. The curve for the test SM-S_v9 indicated that at t = 120 mins the major wall displacement had commenced and reached a value of 5 cm. Contrarily, the curve for the test SM-S_v9-C4 only had a displacement of 2.5 cm at t = 120 mins, and it reached the maximum value at t = 660 mins.

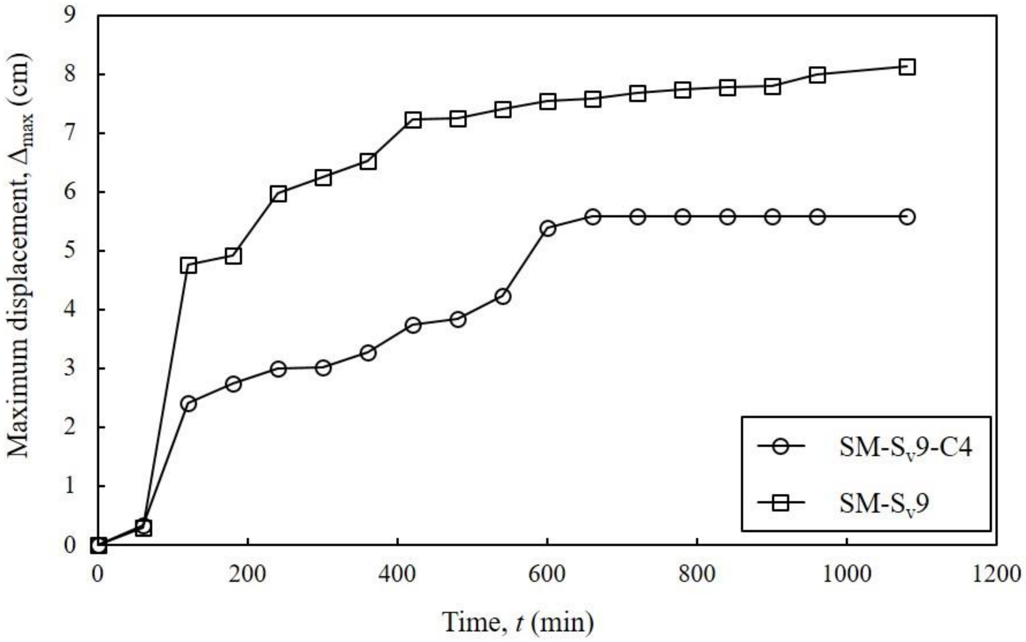

Figure 6.21 Maximum wall displacement versus time

doi:10.6342/NTU201901530

Figure 6.22 presents the mobilized reinforcement tensile strain in the tests SM-S$_v$9 and SM-S$_v$9-C4. The maximum tensile strain mobilized in the test without cushion was around 4%, while it was only 3% if sand cushions were adopted. The mobilized reinforcement tensile strain in the tests SM-S$_v$9 and SM-S$_v$9-C4 was significantly different at the topmost layer, as the displacement of the test SM-S$_v$9 was significantly larger than that of the test SM-S$_v$9-C4 in the topmost layer. Moreover, the major potential sliding surface is more shallow in the test SM-S$_v$9. Notably, a second potential sliding surface indicated by the locus of maximum tensile strain was observed in the test SM-S$_v$9.

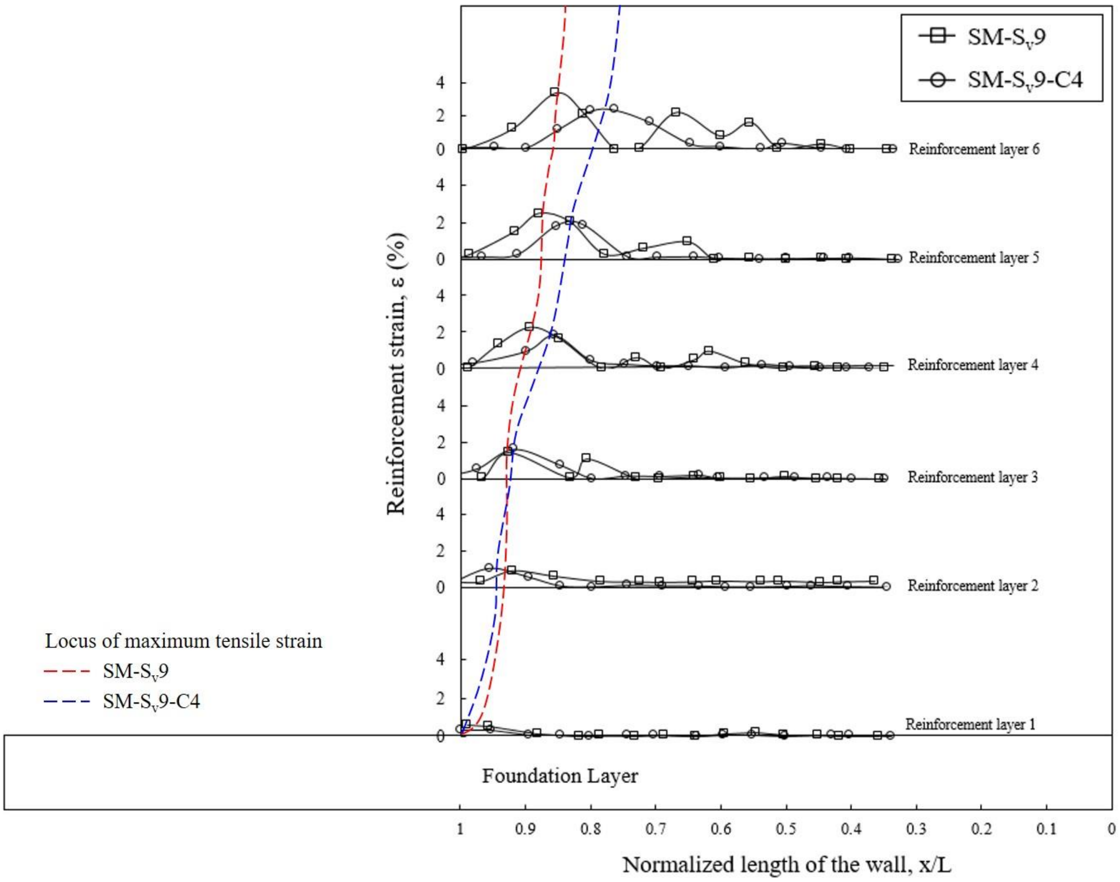

Figure 6.22 Reinforcement tensile strain

Figure 6.23 presents the maximum reinforcement tensile force profile. The mobilized reinforcement tensile strain displayed different patterns before and after the adoption of sand cushions. In the tests SM-S_v9 (before the application of sand cushions), the reinforcement tensile force at the top layers was much larger than the earth pressure method. After the adoption of sand cushions, the values in each layer became uniform; however, the values were all larger than that estimated from the earth pressure method.

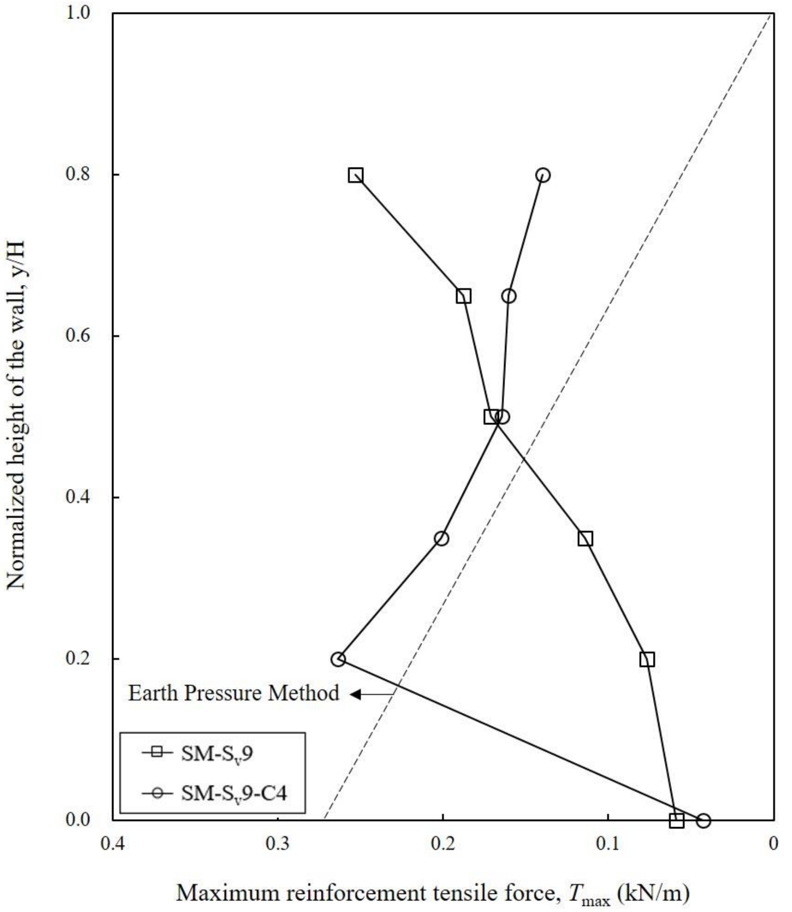

Figure 6.23 Maximum reinforcement tensile force profile

doi:10.6342/NTU201901530

Figure 6.24 demonstrates the strain contour estimated from the PIV analysis. For the model test without cushion, the maximum strain concentrated at the top layer owing to the large displacement induced by the accumulation of water infiltration at the top. With sand cushion applied, the maximum strain contour propagated through all the layers. This is similar to the strain propagation of the model test SP-S_v9, in which sandy soil was used as backfill. Furthermore, the adoption of sand cushions reduced the maximum strain by 30%, from a maximum of 36% to 26%.

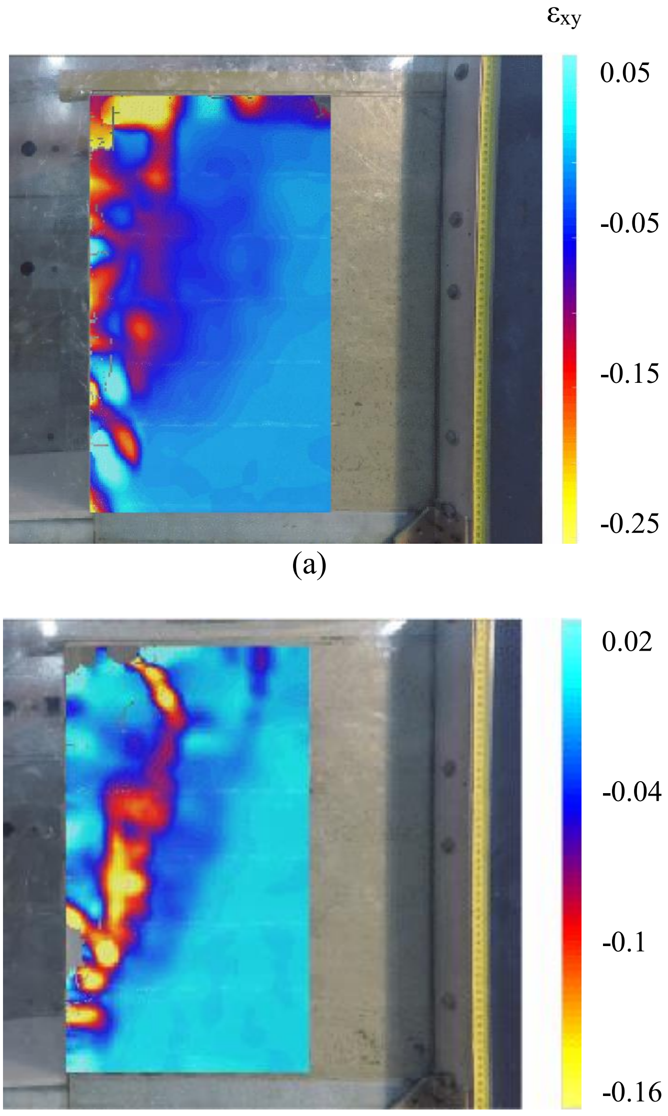

(a)

(b)

Figure 6.24 Strain contour from PIV analysis: (a) SM-S_v9; (b) SM-S_v9-C4

doi:10.6342/NTU201901530

In summary, the displacement of the wall can be significantly reduced with the application of sand cushion owing to the high interface friction between the soil-geogrid interface. Table 6.4 summarizes the performance of the test SM-S$_v$9 and SM-Sv9-C4. The failure modes in both tests were progressive. The main difference between the two tests is the development of the soil shear strain. For the test SM-S$_v$9, the rainfall infiltrated into the topmost layer, causing the loss of matric suction and soil shear strength. Moreover, the maximum displacement and the maximum soil shear strain developed at the top. Regarding the test SM-S$_v$9-C4, the application of sand cushions can provide drainage and prevent water accumulation on the topmost layer. In addition, the development of the soil shear strain resembled the pattern in the test SP-S$_v$9, in which the potential sliding surface propagated through all the layer.

Table 6.4 Summary of test results

Test	SM-Sv9	SM-Sv9-C4
FS_{breakage}	2.1	2.1
FS_{pullout} (dry)	3.6	4.4
FS_{pullout} (wet)	2.5	4.3
Maximum wall displacement, Δ_{max} (cm)	8	5.5
Maximum reinforcement tensile strain, ε_{max} (%)	4	3
Tension cracks	Y	Y
Final stage	Excessive displacement	Minor displacement
Failure mode	Progressive	Progressive

6.2.3 Test SM-S$_v$12-C4 (Adoption of Sand Cushions)

Figure 6.25 shows the pictures of the test SM-S$_v$12-C4. The wall did not move until the first tension crack developed at the topmost layer at 88 mins after the rainfall started. The crack quickly propagated downward to the lower layers and 20 minutes after, more tension cracks were found at the topmost layer. After six and a half hours, water started to fill into the tension cracks, causing further slight wall displacement.

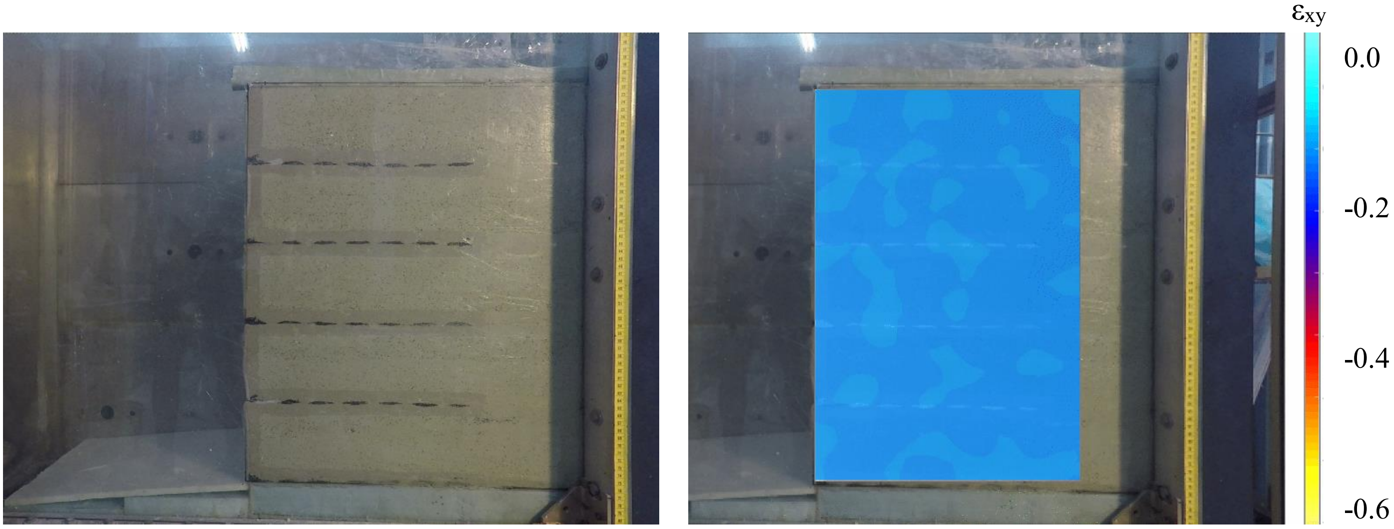

(a) ① Start of the test (t = 0 min)

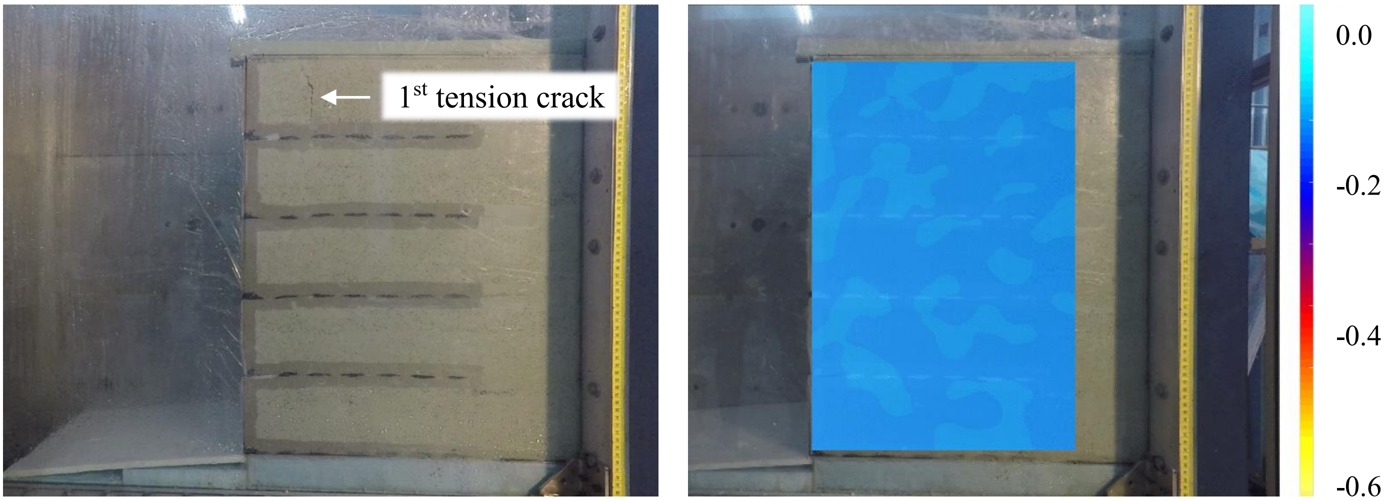

(b) ② Water reached the bottom and first tension crack developed (t = 88 mins)

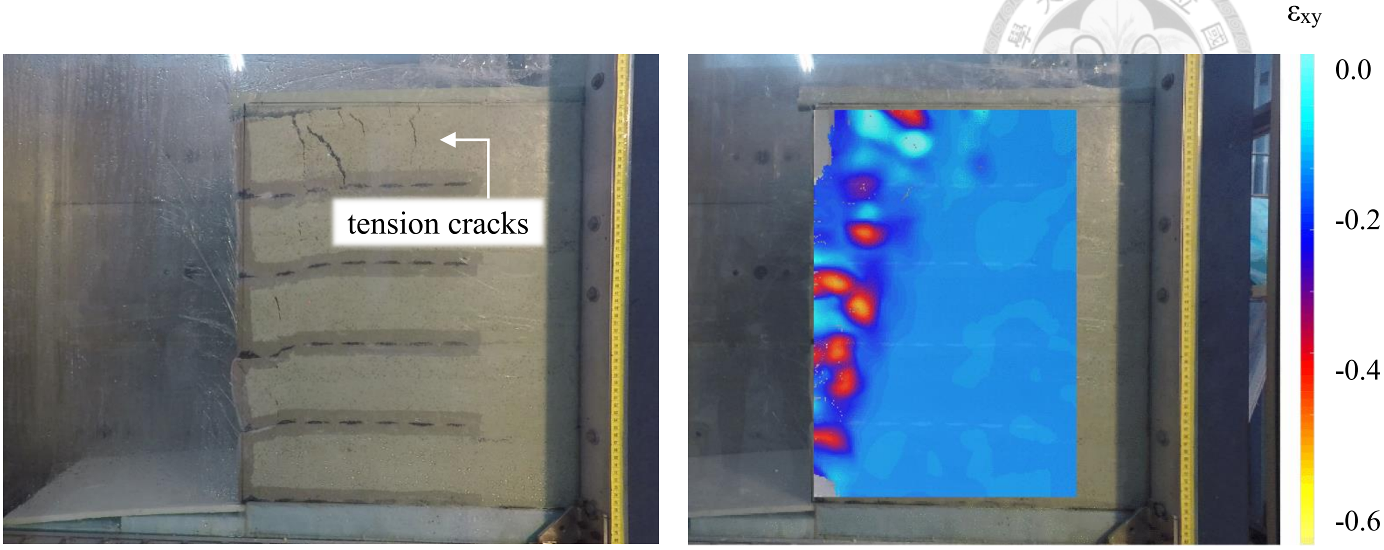

(c) ③ Second tension crack developed (t = 107 mins)

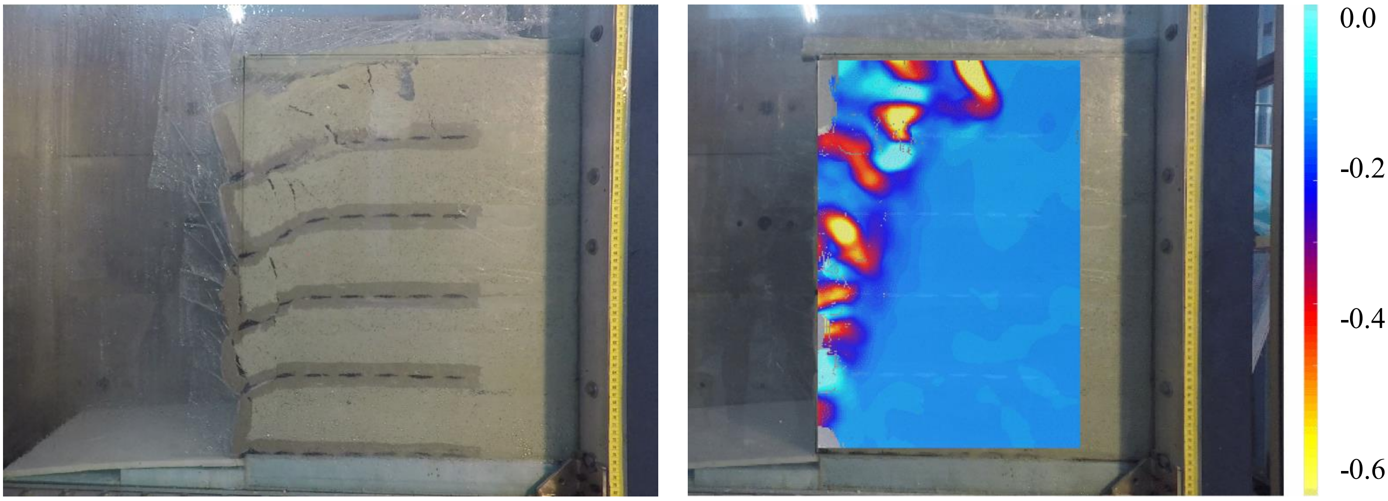

(d) ④ End of the test (t = 1080 mins)

Figure 6.25 Pictures of the model test SM-S_v12-C4

Figure 6.26 presents the change of the volumetric water content with time elapse. The first tension crack developed when the water reached the bottom of the wall. VWC3 was cut off because the development of the tension crack resulted in the exposure of the volumetric water content gauge, causing the measured value beyond saturation. VWC3, VWC2, and VWC1 sensed the water in succession as the infiltrated water flowed along the direction of the gravity. VWC2 and VWC1 eventually reached the same value because the permeability of the marginal backfill was relatively low; the water was indeed confined at the top layers as the water was ponded in the tension cracks as observed.

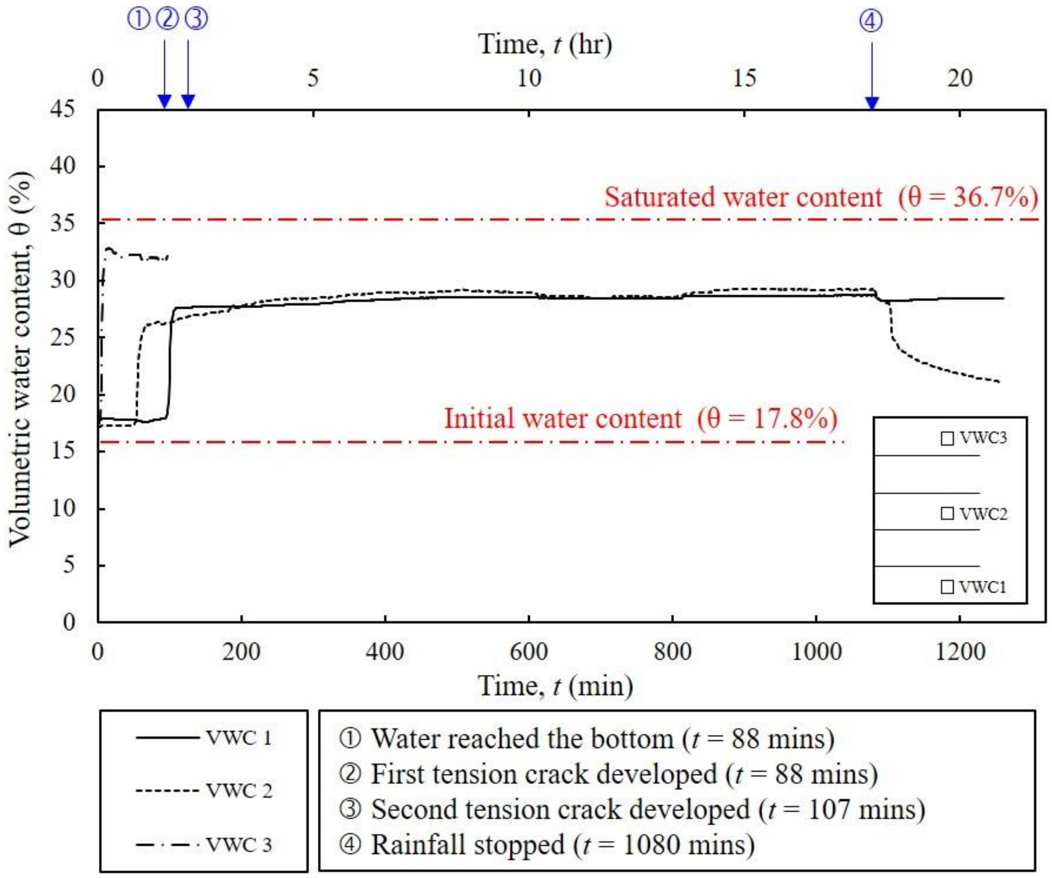

Figure 6.26 VWC with time elapse

Figure 6.27 displays the wall displacement profile. Several sudden displacements were observed within *t* = 90 ~ 600 mins. The maximum wall displacement at the end of the test was found in the topmost layer with a value of 15% wall height. The test without sand cushions (SM-S_v12) had a maximum wall displacement of 33% wall height at *t* = 127 minutes and the wall fully collapsed. In the test SM-S_v12-C4 however, even the reinforcement had large S_v, the wall did not collapse owing to the adoption of the sand cushions. The large interface friction between the sand cushions and the geogrid reinforcement constrained the excessive displacement.

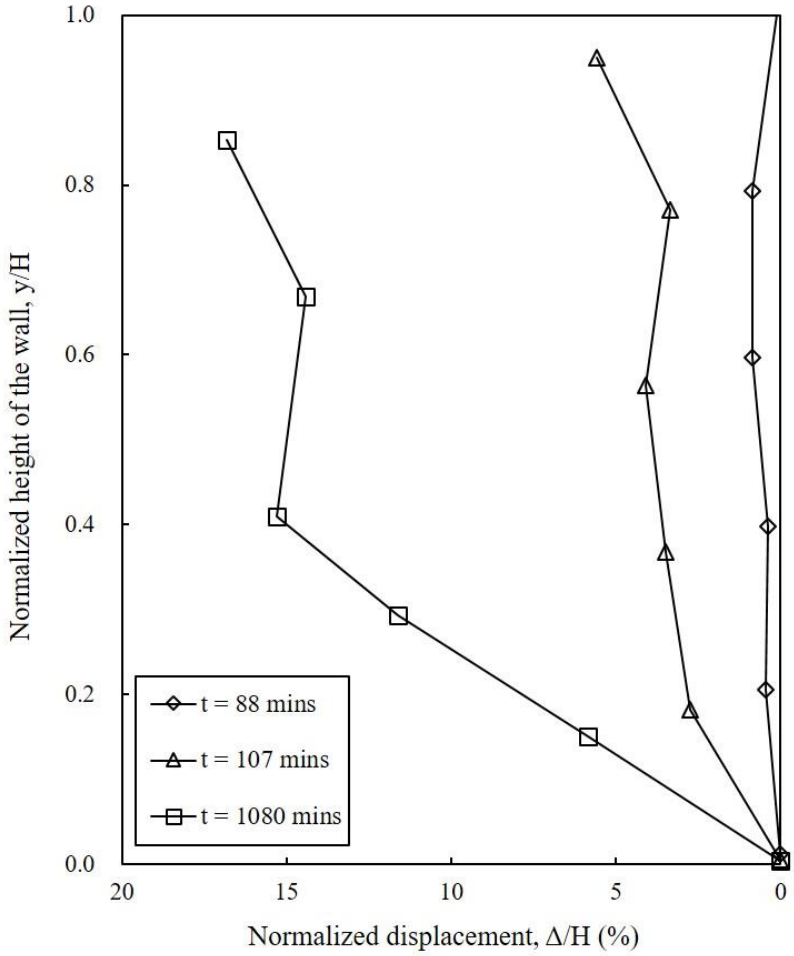

Figure 6.27 Wall displacement profile

doi:10.6342/NTU201901530

Figure 6.28 presents the maximum wall displacement and settlement versus time. The major wall displacement commenced at t = 60~120 mins after the rainfall started. The development of the major wall displacement in the first 2 hours resulted from the loss of matric suction and soil shear strength upon the infiltration of rainfall. The displacement became gradual afterward. Furthermore, the rainfall infiltration had led to the accumulation of water in the topmost layer, causing the saturated soil bulged out. However, the soil not collapse because of the resistance force from the geogrid reinforcement and the strong interface friction between the sand cushions and the geogrid reinforcement.

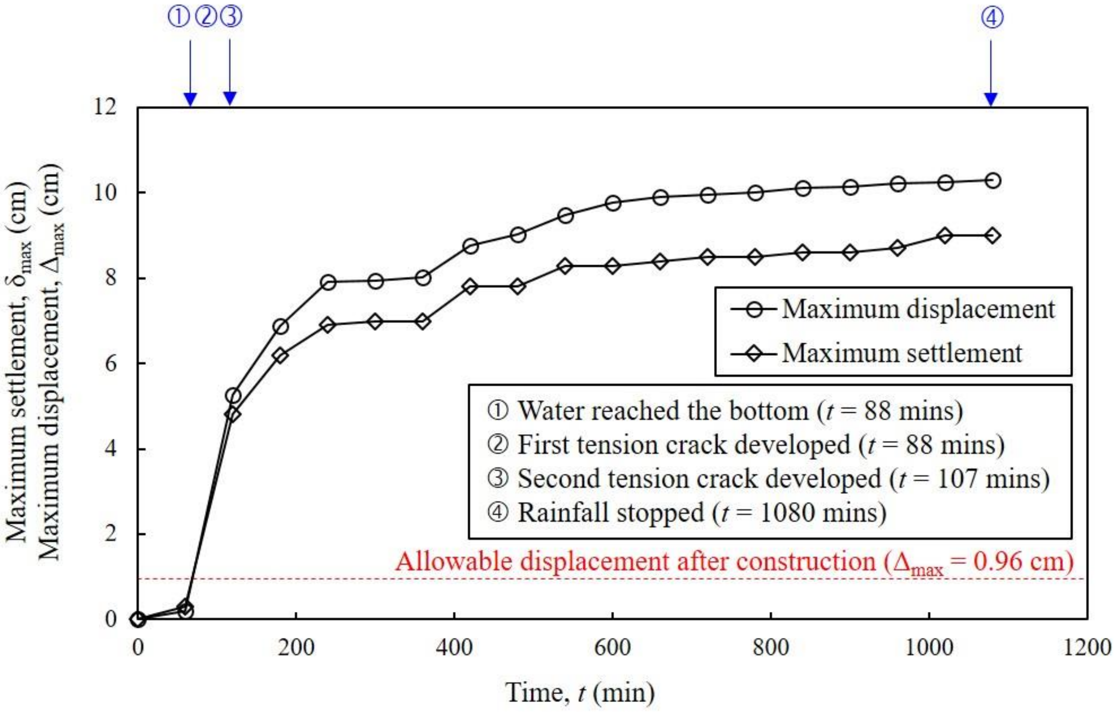

Figure 6.28 Maximum wall displacement and settlement versus time

Figure 6.29 presents the mobilized reinforcement tensile strain in each layer. The maximum strain was mobilized at the topmost layer where the largest wall displacement ensued. The maximum mobilized strain was 5%, which is very close to the ultimate tensile strain of the geogrid reinforcement (ε_u = 6.5%), and this can be correlated to the relatively small factor of safety for breakage (FS_{breakage} = 1.6). By connecting the locus of the maximum tensile strain, a critical failure surface can be plotted. Notably, there were two regions where larger tensile strains were mobilized in layers 3, 4, and 5. The regions coincided with the location of the tension cracks. Moreover, the strain contour from the PIV analysis indicated large strains at both the critical failure surface and the location of tension cracks. The maximum strain determined from the PIV analysis was 65%, which was much larger than the soil failure strain. Failure was indeed observed along the maximum strain contour.

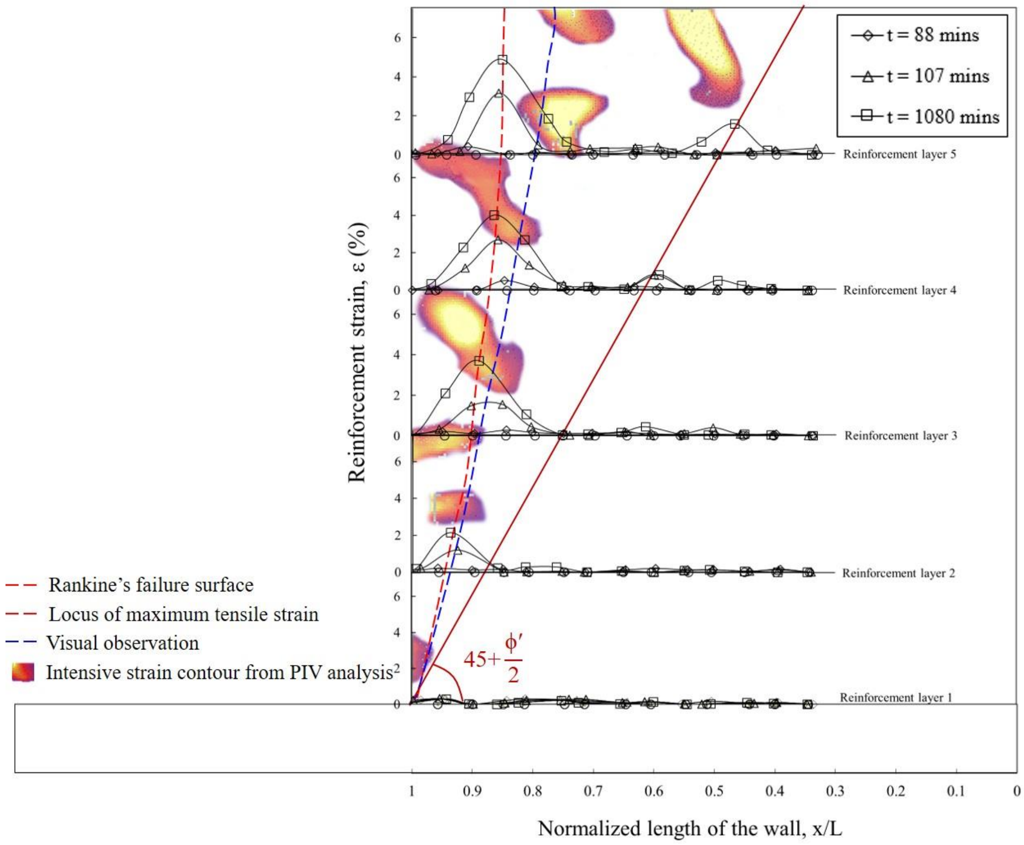

Figure 6.29 Reinforcement tensile strain

Figure 6.30 displays the maximum reinforcement tensile force profile. The maximum reinforcement tensile strain was a cantilever type, causing the strain at the top layers be underestimated while the strain at the lower layers was overestimated by the earth pressure method.

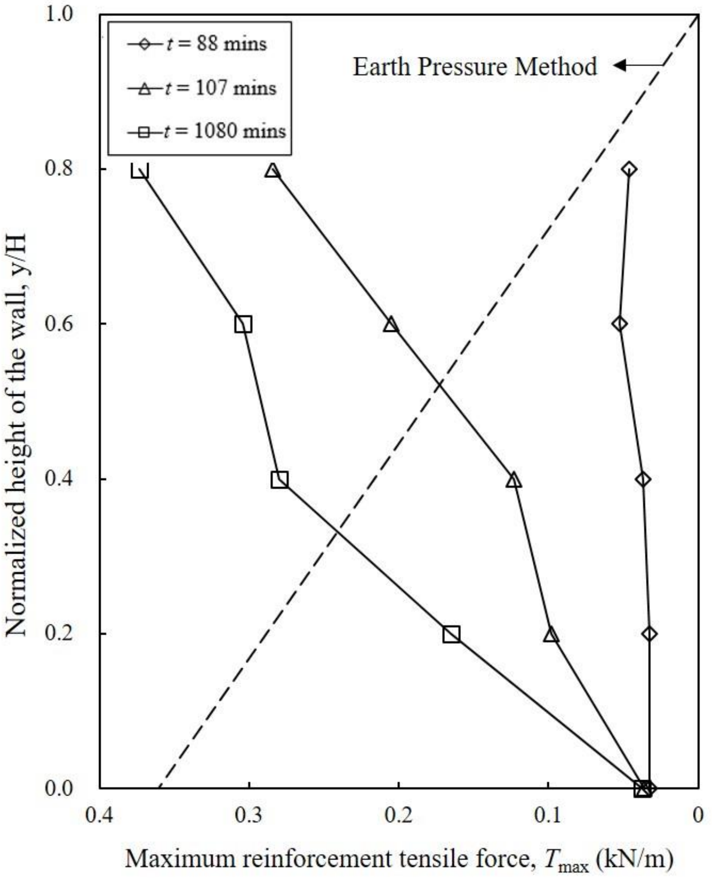

Figure 6.30 Maximum reinforcement tensile force profile

In summary, the test results from the test SM-S_v12-C4 demonstrates that the installation of sand cushions can effectively prevent the collapse of the wall, even though excessive deformation was observed at the end of the test. The low permeability of the backfill caused the accumulation of rainfall, further induced the loss of matric suction and soil shear strength. Tension cracks, large deformation, and the critical failure surface therefore developed. Nevertheless, the high interface friction between the soil and geogrid reinforcement successfully prevented the wall from collapse.

6.2.4 Comparison

Table 6.5 summarizes the factor of safety against breakage and pullout for the tests SM-S_v12 and SM-S_v12-C4, and Figure 6.31 presents the pictures of the two tests. Notably, Figure 6.31 (a) was taken at the moment before the wall fully collapsed (t = 127 mins). The thickness of the sand cushions was 4 cm, accounting for 26% of the backfill. The factor of safety against pullout was significantly larger in the test SM-S_v9-C12 owing to the high interface shearing characteristic between sand-geogrid interface. However, the factor of safety against breakage was relatively small.

Table 6.5 Factor of safety

Model test	FS_{breakage}	FS_{pullout} (dry)	FS_{pullout} (wet)
SM-S_v12	1.6	2.7	1.9
SM-S_v12-C4	1.6	3.3	3.2


(a) (b)

Figure 6.31 Pictures of tests: (a) SM-S_v12; (b) SM-S_v12-C4

doi:10.6342/NTU201901530

Figure 6.32 shows the wall displacement profile of the test SM-S$_v$12 and SM-S$_v$12-C4. The maximum wall displacement achieved a value of 33% wall height in the test SM-Sv12 before the reinforced wall totally collapsed. Regarding the test SM-S$_v$12-C4, though the wall displacement is quite large (18% wall height), the wall did not collapse. The interface interaction with the geogrid was enhanced and the sand cushions effectively improved the deformation characteristic. With sand cushions adopted, the wall displacement was reduced by 50% with only 26% sand replaced as sand cushions.

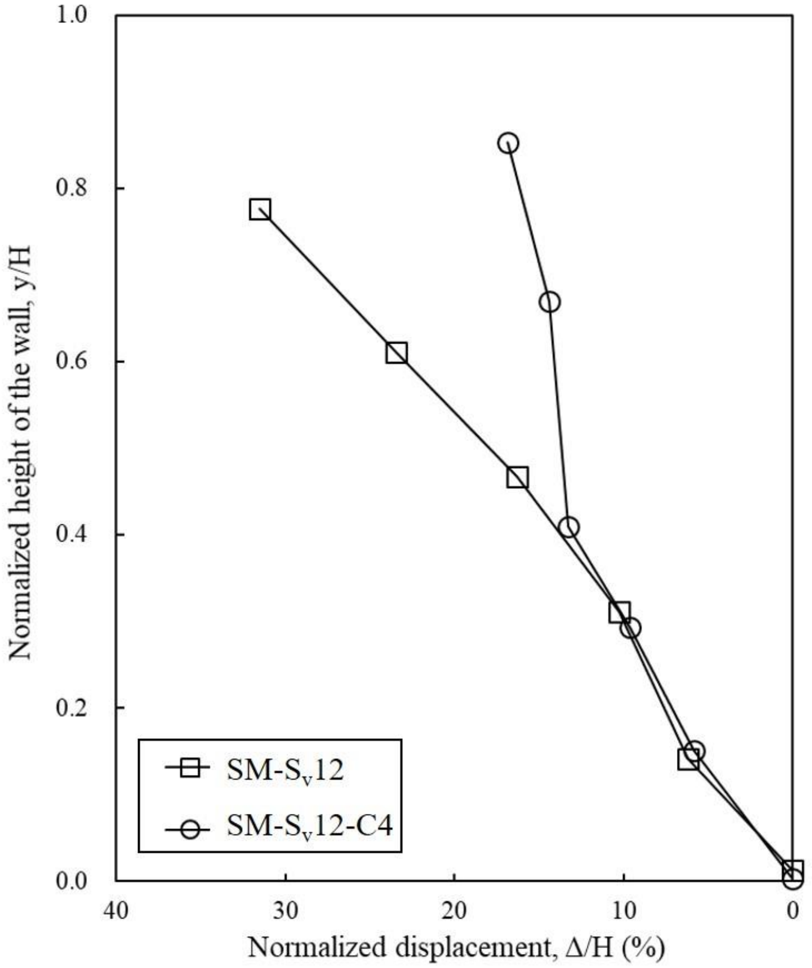

Figure 6.32 Wall displacement profile

Figure 6.33 shows the development of the maximum wall displacement in the test SM-S_v12 and SM-S_v12-C4. The figure indicated that for the test without sand cushions (SM-S_v12), the maximum wall displacement dramatically increased to 11 cm after the tension cracks developed (t = 94 mins). The wall eventually collapsed in an interlayer sliding mode. Contrarily, after the adoption of sand cushions (SM-S_v12-C4), the wall displacement had turned into a more progressive development. The major displacement induced by the loss of matric suction and soil shear strength was 8 cm, followed by a 3 cm successive displacement owing to the development of soil shear strain. The effect of sand cushions can be clearly verified. With such large S_v, the wall experienced large deformation but did not collapse.

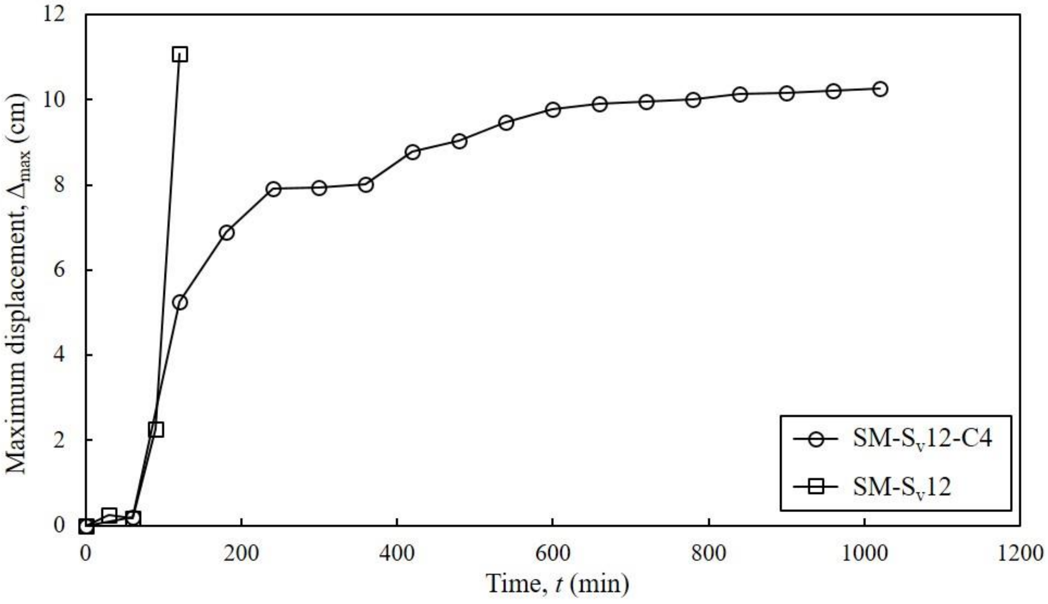

Figure 6.33 Maximum wall displacement versus time

Figure 6.34 presents the mobilized reinforcement tensile strain in the tests SM-S$_v$12 and SM-Sv12-C4. The maximum reinforcement tensile strain mobilized in the two tests were around 5% since the maximum wall displacement observed in the two tests were similar. Notably, the mobilized reinforcement strain in the test SM-S$_v$12 was calculated according to the wall displacement at the moment before the wall collapsed (t = 127 mins). The rather large reinforcement tensile strain mobilized can correspond to the relatively low factor of safety against breakage ($FS_{\text{breakage}} = 1.6$).

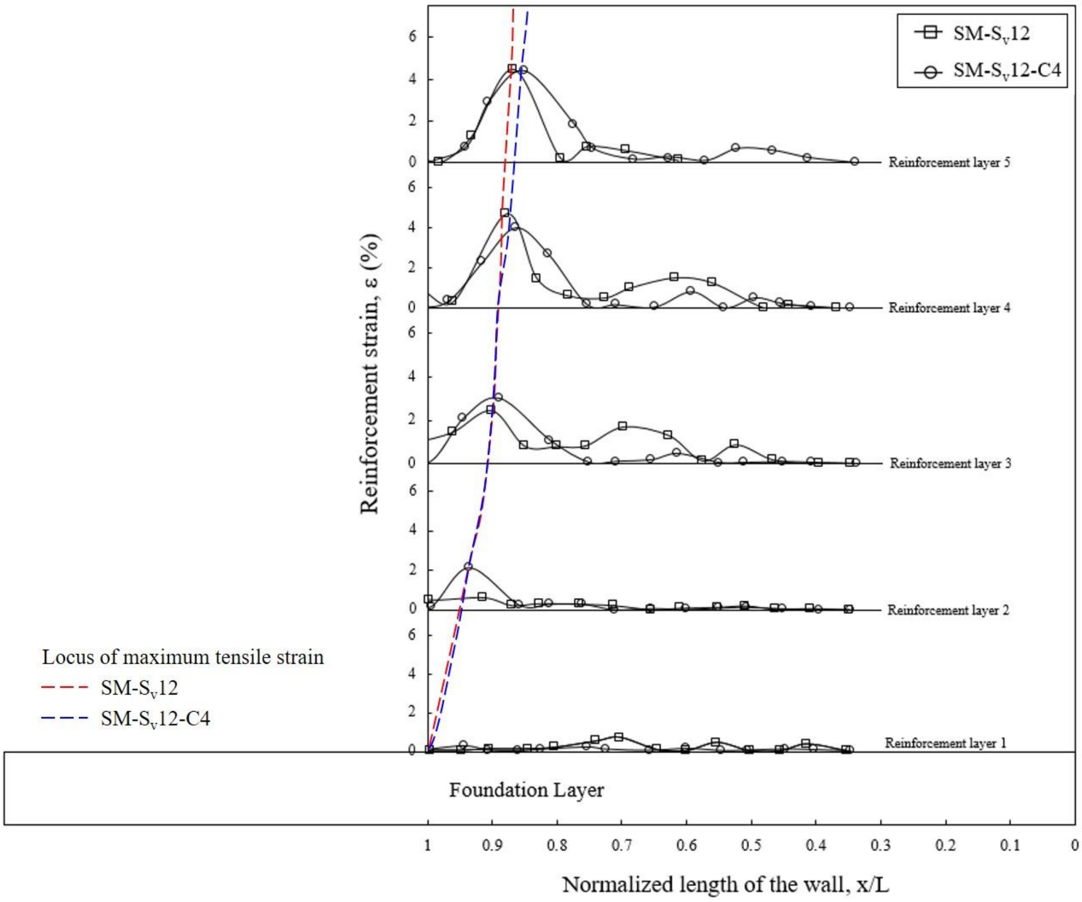

Figure 6.34 Reinforcement tensile strain

doi:10.6342/NTU201901530

Figure 6.35 displays the mobilized maximum reinforcement tensile force profile. The mobilized reinforcement tensile force was similar in both tests since the wall displacement in the both tests were similar. The maximum tensile force occurred at the topmost layer, resembling the cantilever pattern as the wall displacement. The earth pressure method significantly underestimated the tensile force at the top layers and overestimated that at the bottom layers for reinforced walls with marginal backfill.

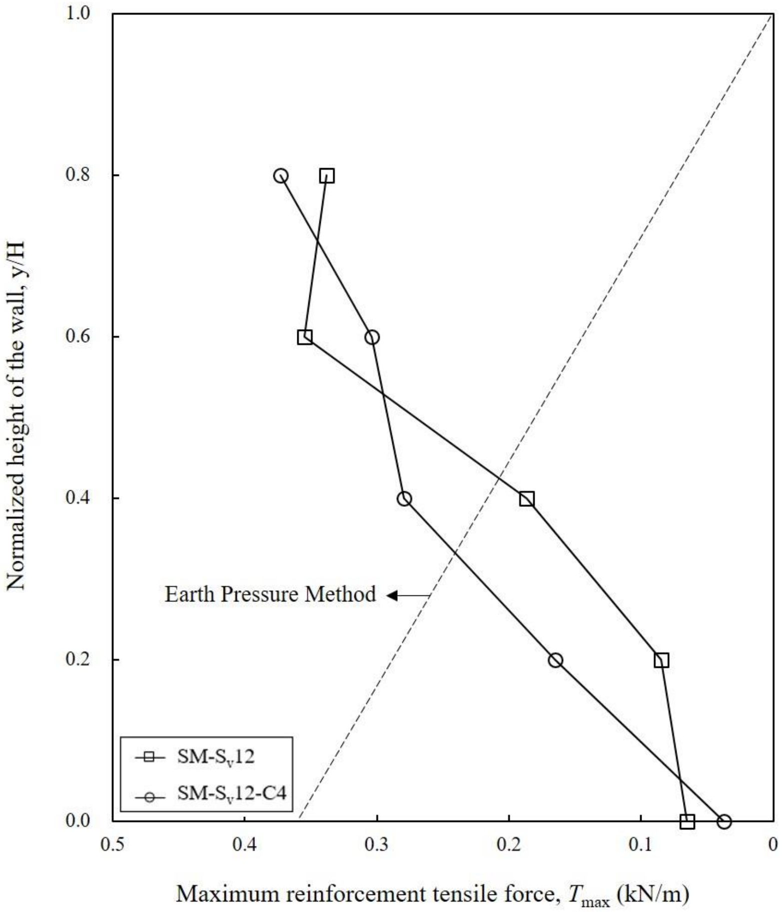

Figure 6.35 Maximum reinforcement tensile force profile

In summary, the adoption of sand cushions can effectively prevent the reinforced wall with large spacing from failure by improving the soil-geogrid interface friction and enhancing the deformation characteristics. Table 6.6 summarizes the performance of the tests SM-S_v12 and SM-Sv12-C4. The stability of the wall was dramatically improved by only replacing 26% of the backfill as sand cushions. Sand cushions can provide drainage and prevent the accumulation of water; the displacement induced by water was therefore restrained. In addition, the deformation characteristic of sand cushions was much better than that of marginal backfills. Specifically, sand cushions can withstand the large overburden pressure and contribute to the wall stability. With that, the test SM-Sv12-C4 did not collapse even with such large S_v.

Table 6.6 Summary of test results

Test	SM-Sv12	SM-Sv12-C4
FS_{breakage}	1.6	1.6
FS_{pullout} (dry)	2.7	3.3
FS_{pullout} (wet)	1.9	3.2
Maximum wall displacement, $\Delta_{\max}$ (cm)	11	10
Maximum reinforcement tensile strain, $\varepsilon_{\max}$ (%)	5	5
Tension cracks	Y	Y
Final stage	Fully collapsed	Excessive deformation
Failure mode	Sudden	Progressive

Chapter 7 Conclusions and Recommendations

7.1 Conclusions

This study investigates the performance of GRS walls with marginal backfills under rainfall conditions. In addition, improved methods for the design of GRS walls with marginal backfill subjected to rainfall were also proposed by investigating the results from a series of model tests. The following conclusions can be drawn from the findings of this study:

1. The wall stability can be enhanced and the wall displacement can be effectively restrained by reducing the reinforcement spacing, applying backfill with better quality, or adopting sand cushions at the reinforcement.
2. GRS walls with marginal backfill experienced interlayer sliding failure mode under large reinforcement spacing (S_v = 12 cm). Excessive deformation happened if the reinforcement spacing was reduced to 9 cm. When the reinforcement spacing was reduced to 6 cm, the wall remained stable and wall displacement was hardly observed.
3. Wall deformation is simply assumed to be within allowable limits, provided that the design meets the required *FS*s for GRS walls. However, the assumption was limited for GRS walls under normal conditions. Excessive wall displacement and tension cracks induced by such are essential factors aside from *FS*, especially under rainfall conditions because tension cracks accelerate the accumulation of water, resulting in the loss of matric suction and soil shear strength. Therefore, *FS*s for GRS walls against rainfall should be set higher ($FS_{\text{rainfall}} = 1.8\ FS_{\text{dry}}$) that the deformation becomes minor.

4. A much more stable GRS wall can indeed be attained by applying a backfill with better quality. However, GRS walls with sandy backfill experience surficial shallow failure. Compared to the GRS walls with marginal backfill, the tension cracks and failure surface occurred suddenly.
5. The adoption of the sand cushions by replacing only 36% of the backfill is complementary beneficial to the performance of GRS walls with marginal backfill under rainfall conditions. While GRS walls with marginal backfill present a progressive failure due to the loss of matric suction and the lack of interface friction between the soil and the geogrid, and GRS walls with granular backfill display sudden cracks, sand cushions can effectively enhance the interface friction between the soil-geogrid interface and improve the deformation characteristics.

7.2 Recommendations for Future Study

1. Smaller reinforcement spacing should be design for the top layers for GRS walls with marginal backfill under rainfall condition since the maximum displacement and soil shear strain developed at the top.
2. The performance of GRS walls with different thickness of sand cushions can be evaluated to determine the most efficient design.
3. Numerical analysis can be carried out to investigate the performance of the improved design methods.

doi:10.6342/NTU201901530

References

ASTM D421. (2007). Standard practice for dry preparation of soil samples for particle-size analysis and determination of soil constants: ASTM International, West Conshohocken, PA, USA.

ASTM D4253. (2002). Standard test methods for maximum index density and unit weight of soils using a vibratory table: ASTM International, West Conshohocken, PA, USA.

ASTM D4254. (2000). Standard test methods for minimum index density and unit weight of soils and calculation of relative density: ASTM International, West Conshohocken, PA, USA.

ASTM D6836. (2008) Standard test methods for determination of the soil water characteristic curve for desorption using a hanging column, pressure extractor, chilled mirror hygrometer, and/or centrifuge: ASTM International, West Conshohocken, PA, USA.

ASTM D792. (2013). Standard test methods for density and specific gravity (relative density) of plastics by displacement: ASTM International, West Conshohocken, PA, USA.

Balakrishnan, S., and Viswanadham, B. V. S. (2016). Performance evaluation of geogrid reinforced soil walls with marginal backfills through centrifuge model tests. *Geotextiles and Geomembranes*, 44(1), 95-108.

Bhattacherjee, D., and Viswanadham, B. V. S. (2015). Numerical studies on the performance of hybrid-geosynthetic-reinforced soil slopes subjected to rainfall. *Geosynthetics International*, 22(6), 1-17.

Buckingham, E. (1914). On physically similar systems; illustrations of the use of dimensional equations. *Physical review*, 4(4), 345.

Chen, H. T., Hung, W. Y., Chang, C. C., Chen, Y. J., and Lee, C. J. (2007). Centrifuge modeling test of a geotextile-reinforced wall with a very wet clayey backfill. *Geotextiles and Geomembranes*, 25(6), 346-359.

FHWA. (2009). Design and construction of mechanically stabilized earth walls and reinforced soil slopes-Volume I. *U. S. Department of Transportation Federal Highway Administration,* NHI-10-024.

FHWA. (2009). Design and construction of mechanically stabilized earth walls and reinforced soil slopes-Volume II. *U. S. Department of Transportation Federal Highway Administration,* NHI-10-024.

Gallage, C., Jayakody, S., and Uckimura, T. (2012). Effects of slope inclination on the rain-induced instability of embankment slopes. *Proceedings of the Second International Conference on Geotechnique, Construction Materials and Environment,* 196-201.

Koerner, R. M., and Koerner, G. R. (2013). A data base, statistics and recommendations regarding 171 failed geosynthetic reinforced mechanically stabilized earth (MSE) walls. *Geotextiles and Geomembranes*, 40, 20-27.

Langharr, H. L. (1951). *Dimensional analysis and theory of models*. Krieger.

doi:10.6342/NTU201901530

Liu, C. N., Yang, K. H., Ho, Y. H., and Chang, C. M. (2012). Lessons learned from three failures on a high steep geogrid-reinforced slope. *Geotextiles and Geomembranes*, 34, 131-143.

Liu, C. N., Yang, K. H., and Nguyen, M. D. (2014). Behavior of geogrid–reinforced sand and effect of reinforcement anchorage in large-scale plane strain compression. *Geotextiles and Geomembranes*, 42(5), 479-493.

Mamaghanian, J., Razeghi, H. R., Viswanadham, B. V. S., and Manikumar, C. H. S. G. (2018). Behaviour of geogrid reinforced soil walls with marginal backfills with and without chimney drain in a geotechnical centrifuge. *Physical Modelling in Geotechnics*, 2, 1211-1216.

Portelinha, F. H. M., Bueno, B. S., and Zornberg, J. G. (2013). Performance of nonwoven geotextile-reinforced walls under wetting conditions: Laboratory and field investigations. *Geosynthetics International,* 20(2), 90-104.

Portelinha, F. H. M., and Zornberg, J. G. (2017). Effect of infiltration on the performance of an unsaturated geotextile-reinforced soil wall. *Geotextiles and Geomembranes,* 45(3), 211-226.

Shibuya, S., Kawaguchi, T., and Chae, J. (2007). Failure of reinforced earth as attacked by Typhoon No.23 In 2004. *Soils and Foundations,* 47(1), 153-160.

Thuo, J. N., Yang, K. H., and Huang, C. C. (2015). Infiltration into unsaturated reinforced slopes with nonwoven geotextile drains sandwiched in sand layers. *Geosynthetics International,* 22(6), 1-18.

Tognon, A. R., Rowe, R. K., and Brachman, R. W. (1999). Evaluation of side wall friction for a buried pipe testing facility. *Geotextiles and Geomembranes,* 17(4), 193-212.

Viswanadham, B. V. S., and König, D. (2004). Studies on scaling and instrumentation of a geogrid. *Geotextiles and Geomembranes,* 22(5), 307-328.

Wu, J. Y., and Chou, N. N. (2013). Forensic studies of geosynthetic reinforced structure failures. *Journal of Performance of Constructed Facilities,* 27(5), 604-613.

Yang, K. H., Thuo, J. N., Chen, J. W., and Liu, C. N. (2019). Failure investigation of a geosynthetic-reinforced soil slope subjected to rainfall. *Geosynthetics International,* 26(1), 42-65.

Yang, K. H., Thuo, J. N., Huynh, V. D. A., Nguyen, T. S., and Portelinha, F. H. M. (2018). Numerical evaluation of reinforced slopes with various backfill-reinforcement-drainage systems subject to rainfall infiltration. *Computers and Geotechnics*, 96, 25-39.

Yoo, C., and Jang D.W., (2013). Geosynthetic reinforced soil wall performance under heavy rainfall. *Proceedings of the 18th International Conference on Soil Mechanics and Geotechnical Engineering*, 2131-2134.

Yoo, C., and Shin, S. M. (2016). Performance of geosynthetic reinforced wall during rainfall. *Japanese Geotechnical Society Special Publication,* 2(64), 2180-2185.

Yoo, C., and Jung, H. Y. (2006). Case history of geosynthetic reinforced segmental retaining wall failure. *Journal of Geotechnical and Geoenvironmental Engineering,* 132(12), 1538-1548.

doi:10.6342/NTU201901530

鄭恆志，(2004)，“加勁格網之介紹與應用”，盟鑫工業股份有限公司

馮高原，(2010)，“錨定纖網系統邊坡加勁模型試驗”，國立臺灣大學碩士論文，台北

陳榮河、紀柏全，(2010)，“模型邊坡試驗之因次分析”，地工技術，125，pp. 7-14

蔡明宏，(2011)，“三軸壓縮試驗下加勁土壤力學行為與加勁材應變發展之研究”，國立臺灣科技大學碩士論文，台北

黃渝紋，(2012)，“三軸壓縮試驗探討蜂巢格網的圍束效應”，國立臺灣大學碩士論文，台北

童自裕，(2013)，“降雨引致異質性邊坡破壞之模型試驗”，國立臺灣大學碩士論文，台北

周南山，(2016)，“地工合成材料在永續工程之應用”，環境工程會刊

白名琁，(2018)，“纖維加勁砂土土堤受滲流作用之模型試驗”，國立臺灣科技大學碩士論文，台北

賴兆偉，(2018)，“加勁基礎受正斷層作用之物理模型試驗研究”，國立臺灣科技大學碩士論文，台北

Questions and Suggestions from the Panels

A. Professor Ching-Chuan Huang

1. It seems like you don’t have quantitative conclusions regarding the *FS*. For instance, *FS* is required to be at least 1.5 under normal, dry conditions. How much do you recommend the FS to be increased for GRS walls under rainfall conditions?

   Reply: Thank you for the suggestion. The quantitative conclusions regarding *FS* has been added in Figure 5.25 and the conclusions. The *FS* against pullout should be increase by 1.8 times under rainfall conditions according to the allowable maximum wall displacement.

2. For the test SM-S_v12, do you consider that pullout failure had occurred?

   Reply: According to the observation, the geogrid reinforcement were indeed displaced during the test; however, the reinforcements were not fully pulled out. I would not consider pullout failure occurred in this test. The actual failure mode is the interlayer sliding failure, in which the secondary reinforcement flipped out.

3. In page 48, the stiffness of the geogrid reinforcement at 2% and 5% strain should be reported since they are important values in practical engineering.

   Reply: Thank you for the suggestion. The stiffness of the reinforcement at 2% and 5% strain has been reported.

4. In every test, did you find the wetting front propagation consistent?

   Reply: Yes, the wetting front propagation was consistent. In every test, the water infiltrated from the top to the bottom, causing VWC3, 2, and 1 sensed water in succession. Notably, only the ultimate value of the VWC was different owing to the different backfills and configurations in each test.

doi:10.6342/NTU201901530

5. For S_v = 9 cm, which one do you think is a better backfill? Sand or Silty sand?

   Reply: I think the failure mode was different. For the wall with marginal backfill, the wall experienced severe cantilever wall displacement. For the wall with granular backfill, though the wall displacement was small, the failure occurred rather sudden. These two results emphasize the advantage of one of the improved methods (sand cushions). The application of sand cushions can combine the advantages of marginal backfill and granular backfill.

B. Professor Yong-Shan Hung

1. The void ratio at the target relative density on page .38 should be 0.77 instead of 0.73, you need to check the value.

   Reply: Thank you for the suggestion. The void ration at the target relative density has been corrected to 0.77.

2. Could you tell me why you choose the vertical pressures of 50, 100, and 150 kPa to evaluate the behavior if interface between the soil and the reinforcement? Do you think those pressures are suitable for the reduce scale model wall tests?

   Reply: Although the vertical pressures chosen may seem too high to represent the overburden pressure of the reduce scale model tests, the chosen vertical pressure was considered appropriate regarding the results from the traditional direct shear tests. The traditional direct shear box has a small diameter of 5 cm. The boundary friction will significantly influence the test results. Therefore, larger vertical pressures like 52, 100, and 150 kPa should be adopted to reduce the boundary effect of the direct shear tests.

3. Equation 4.5 on page 60 doesn't seem right.

   Reply: Thank you for the suggestion. The equation has been corrected.

4. Can you explain why the FS against pullout for SM-Sv9 and SM-Sv6 are the same? Shouldn’t the FS against pullout becomes larger when the reinforcement spacing was reduced?

   Reply: If the reinforcement spacing was reduced from 9 cm to 6 cm, the driving force in each layer of reinforcement would be smaller. In addition, the overburden pressure of the topmost layer was reduced, resulting in the reduction of the resisting force. The factor of safety is calculated as the resisting force over the driving force. Therefore, the FS against pullout was the same since the reduction of the resisting force diminished the reduction of the driving force.

5. Can you enunciate more about the construction of the wall including the wrap-around facing, filter layer, and the crest of the wall?

   Reply: The length of the reinforcement was 35 cm, and the backfill soil was compacted on the geogrid reinforcement. Next, the filter layer was filled in and compacted. Afterward, the geogird reinforcement and the facing were wrapped-around, and the wrap-around length is 15 cm. Notably the wrap-around length in the topmost layer was lengthened to 30 cm. Finally, colored tape was applied at the crest of the wall, at which the model wall contact with the sandbox. The colored tape was used to prevent water leaking into the model wall from the interface between the model wall and the sandbox.

6. How do you get the shear strain contour from the PIV analysis?

   Reply: The PIV analysis was done via a free MATLAB program called Ncorr. The key factor to the analysis was the seed. The seed was given manually in the reference picture. The software will trace the seed in the remaining pictures. During this process, it is essential to check the location of the seed to ensure the correct seed location.

After generating the seed in every picture, we were able to format displacement and calculate the strains.

7. In the figures regarding the variation of the VWC, how do you get the saturated water content θ?

   Reply: The saturated volumetric water content was calculated from the saturated gravimetric water content.

8. In your model tests, you mentioned that you installed pore water pressure transducers. Do you observe any relation or behavior through these transducers during rainfall?

   Reply: Yes. We did install pore water transducers in all the tests. However, we were not able to measure any meaningful values. The values became negative as the tests went on. This might because the transducers were mounted at the margin of the wall. And the rainfall was too slight for the transducer to measure. We might need other type of transducers to measure the correct pore water pressure in the future.

C. Professor Yong-Show Fang

1. The references you cite should be consistent.

   Reply: Thank you for the suggestion. The references have been corrected.

2. In Section 3.2.1, the pycnometer test should be called specific gravity test

   Reply: Thank you for the suggestion. The Section 3.2.1 has been corrected.

3. Why do you use Kaolinite?

   Reply: It is easier to obtain Kaolinite with standard quality.

4. What is the process of classifying the silty sand? Why it is not classified as clay?

   Reply: The silty sand was classified by the Unified Soil Classification System. First, it was in the category of coarse-grained soils because more than 50% retained on No. 200 sieve. Next, it was classified as sand instead of gravel because more than 50% of

doi:10.6342/NTU201901530

coarse fraction passed through No. 4 sieve. And finally, the test soil contained more than 12% fines and we were not able to get the plastic limit from the Atterberg tests. Thus, it is classified as silty sand (SM) instead of clayey sand (SM).

5. Can you explain what is plain strain condition? Did you consider the boundary condition of you sandbox? The sand box is only 30 cm wide. The boundary effect may have a significant influence to your results.

   Reply: If assumed zero strain in the Z direction, then the axial stress along the Z direction is non-zero. The axial strain along Z direction, the shear stresses and strains on XZ and XY planes are zero. We did consider the boundary effect of the sandbox. We applied water-base lubricant sandwiched between two PE sheets to reduce the boundary friction.